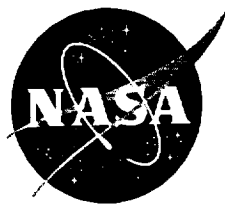


NASA/TM-2002-211392



## **Rotor/Wing Interactions in Hover**

*Larry A. Young and Michael R. Derby*

**April 2002**

## The NASA STI Program Office . . . in Profile

Since its founding, NASA has been dedicated to the advancement of aeronautics and space science. The NASA Scientific and Technical Information (STI) Program Office plays a key part in helping NASA maintain this important role.

The NASA STI Program Office is operated by Langley Research Center, the Lead Center for NASA's scientific and technical information. The NASA STI Program Office provides access to the NASA STI Database, the largest collection of aeronautical and space science STI in the world. The Program Office is also NASA's institutional mechanism for disseminating the results of its research and development activities. These results are published by NASA in the NASA STI Report Series, which includes the following report types:

- **TECHNICAL PUBLICATION.** Reports of completed research or a major significant phase of research that present the results of NASA programs and include extensive data or theoretical analysis. Includes compilations of significant scientific and technical data and information deemed to be of continuing reference value. NASA's counterpart of peer-reviewed formal professional papers but has less stringent limitations on manuscript length and extent of graphic presentations.
- **TECHNICAL MEMORANDUM.** Scientific and technical findings that are preliminary or of specialized interest, e.g., quick release reports, working papers, and bibliographies that contain minimal annotation. Does not contain extensive analysis.
- **CONTRACTOR REPORT.** Scientific and technical findings by NASA-sponsored contractors and grantees.

- **CONFERENCE PUBLICATION.** Collected papers from scientific and technical conferences, symposia, seminars, or other meetings sponsored or cosponsored by NASA.
- **SPECIAL PUBLICATION.** Scientific, technical, or historical information from NASA programs, projects, and missions, often concerned with subjects having substantial public interest.
- **TECHNICAL TRANSLATION.** English-language translations of foreign scientific and technical material pertinent to NASA's mission.

Specialized services that complement the STI Program Office's diverse offerings include creating custom thesauri, building customized databases, organizing and publishing research results . . . even providing videos.

For more information about the NASA STI Program Office, see the following:

- Access the NASA STI Program Home Page at <http://www.sti.nasa.gov>
- E-mail your question via the Internet to [help@sti.nasa.gov](mailto:help@sti.nasa.gov)
- Fax your question to the NASA Access Help Desk at (301) 621-0134
- Telephone the NASA Access Help Desk at (301) 621-0390
- Write to:  
NASA Access Help Desk  
NASA Center for Aerospace Information  
7121 Standard Drive  
Hanover, MD 21076-1320

NASA/TM-2002-211392



## **Rotor/Wing Interactions in Hover**

*Larry A. Young  
NASA Ames Research Center  
Moffett Field, California 94035*

*Michael R. Derby  
Aerospace Computing, Inc.  
Mountain View, California 94035*

National Aeronautics and  
Space Administration

Ames Research Center  
Moffett Field, California 94035-1000

---

**April 2002**

Available from:

NASA Center for AeroSpace Information  
7121 Standard Drive  
Hanover, MD 21076-1320  
(301) 621-0390

National Technical Information Service  
5285 Port Royal Road  
Springfield, VA 22161  
(703) 487-4650

## Table of Contents

Nomenclature .....	iv
Abstract.....	1
Introduction.....	1
Approach in Modeling Wing- and Rotor-on-Rotor Interactions .....	4
Wing-On-Rotor Influences.....	7
Rotor-on-Rotor Influences.....	10
Parametric Investigation of Rotor/Wing Interactions.....	12
Conclusions.....	14
References .....	15
Appendix A - Derivation of Rotor/Wing Interaction Model .....	17
Nomenclature -- Appendices .....	17
Description of Flowfield Modeling.....	21
Governing Equations.....	25
Solution for Rotor Induced Velocity Terms.....	31
First (Left-Hand-Side) Rotor .....	31
Second (Right-Hand-Side) Rotor.....	35
Rotor Swirl Velocity Terms.....	36
Solution for Wing Interaction Induced Velocity Terms .....	37
Convex Image Vortex Surfaces .....	39
Rectangular Image Vortex Sheets.....	44
Effect of Interactions on Rotor Thrust/Inflow.....	50
Rotor-on-Rotor Interaction.....	53
Wing-on-Rotor Interactions .....	57
Appendix B - Strength of Wing Image Vortex Sheets .....	63
A Heuristic Argument.....	63
A Numerical Assessment.....	65
An Approximate Analytic Treatment.....	70

## Nomenclature

$b$	Wing span; distance from rotor centerline to centerline (m)
$c$	Wing effective chord length with deflected flaperon (m)
$c_0$	Wing chord length; flaperon not deflected, (m)
$h$	Rotor-to-wing offset distance (m)
$r$	Rotor radial coordinate, origin located at port rotor disk center
$R$	Rotor radius (m)
$x_{\text{flap}}$	Flaperon length (m)
$z$	Vertical coordinate, origin located at port rotor disk center, positive up
$\bar{\lambda}$	Mean inflow constant through rotor disk, including rotor/wing interactional aerodynamics (nondim.)
$\lambda(r, \psi)$	Rotor inflow constant distribution as function of radial station and azimuth angle (nondim.)
$\bar{v}$ ,	Total rotor/wing induced velocities (m/sec)
$\bar{v}_R$	Isolated rotor induced velocities (m/sec)
$\Delta \bar{v}$	Net rotor/wing interference velocities (m/sec)
$\delta_{\text{flap}}$	Flaperon incidence angle (radians)
$\gamma$	Rotor wake vortex cylinder strength ( $\text{m}^2/\text{sec}$ )
$\gamma_{\text{Sheet}}$	Vortex sheath strength ( $\text{m}^2/\text{sec}$ )
$\Gamma$	Rotor wake bound vorticity strength ( $\text{m}^2/\text{sec}$ )
$\Lambda$	Wing sweep (radians)
$\psi$	Rotor angular coordinate (azimuth angle), Ref. line at rotor center, parallel to aircraft longitudinal axis, pointing aft (radians)

# **Rotor/Wing Interactions in Hover**

Larry A. Young  
NASA Ames Research Center, Moffett Field, CA

Michael R. Derby  
Aerospace Computing, Inc., Mountain View, CA

## **Abstract**

Hover predictions of tiltrotor aircraft are hampered by the lack of accurate and computationally efficient models for rotor/wing interactional aerodynamics. This paper summarizes the development of an approximate, potential flow solution for the rotor-on-rotor and wing-on-rotor interactions. This analysis is based on actuator disk and vortex theory and the method of images. The analysis is applicable for out-of-ground-effect predictions. The analysis is particularly suited for aircraft preliminary design studies. Flow field predictions from this simple analytical model are validated against experimental data from previous studies. The paper concludes with an analytical assessment of the influence of rotor-on-rotor and wing-on-rotor interactions. This assessment examines the effect of rotor-to-wing offset distance, wing sweep, wing span, and flaperon incidence angle on tiltrotor inflow and performance.

## **Introduction**

Maximizing hover performance is important to the success of tiltrotor aircraft (Fig. 1). Key to this problem is reducing wing/airframe download and improving rotor performance, while taking into account rotor-on-rotor and wing-on-rotor interactional aerodynamic influences. Though considerable progress has been made over the last several years with respect to understanding these rotor/wing interactions for tiltrotor aircraft, there remains significant opportunities for improved experimental and analytical treatment of the phenomena. It is particularly crucial to gain and apply this improved understanding at the earliest stages of the aircraft design process.

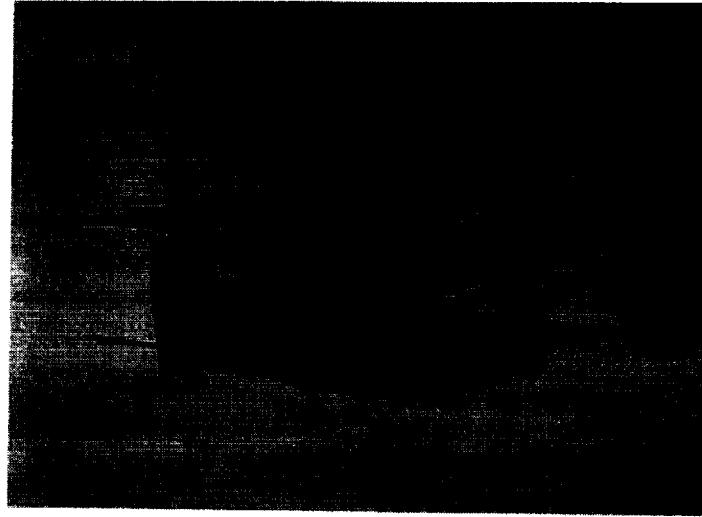


Fig. 1 – Tiltrotor Aircraft in Hover

Numerous experimental and analytical investigations on rotor/wing aerodynamic interactions in hover have been conducted (for example, Refs. 1-5). The focus of the majority of the work in the literature has been to examine tiltrotor download, and the evaluation of possible download reduction devices or techniques. Most of the work has been experimental in nature -- though several analytical/CFD studies have also been performed -- and have employed for the most part semi-span test models (Fig.2). The study of the aerodynamic influence of wing-on-rotor and rotor-on-rotor effects on rotor performance has received only limited treatment to date.

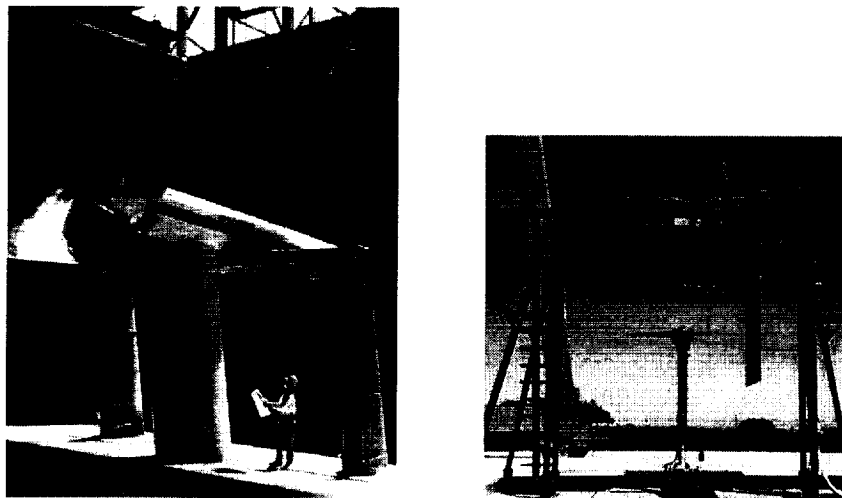


Fig. 2 – Examples of Past Experimental Work

NASA-sponsored civil tiltrotor studies have also recently underscored the importance of proprotor aeroacoustics for civil tiltrotor passenger and community acceptance. Noise



reduction now appears likely to be a major technology driver for future tiltrotor aircraft design. Recent work (Ref. 6) has examined the impact of rotor/wing hover interactions on tiltrotor aeroacoustics. It is clear from this work, and other investigations, that an improved understanding of tiltrotor aerodynamics is necessary to improve hover aeroacoustics predictions. It is important that a simple analysis approach be developed to model the rotor/wing flow field to perform accurate and computationally efficient performance and tiltrotor aircraft hover aeroacoustic predictions -- particularly at the earliest stages of aircraft preliminary design. The Biot-Savart/potential-flow analysis of rotor/wing interactions outlined in this paper is intended, in part, to meet this need.

Figure 3 is a representative flowfield calculation from the tiltrotor rotor/wing interaction analysis developed in this paper. Figure 3 is a contour plot of the calculated vertical induced velocities in a lateral plane passing through both rotor axis centerlines (a line art sketch of a tiltrotor aircraft is overlaid on the contour plot to aid in interpreting the flowfield results). The influence of the aircraft wing is clearly seen in Fig. 3. The rotor wake velocities directly above the wing significantly decrease as the wing surface is approached. Beneath the wing a region of recirculating flow with a small amount of mean upwash is predicted. Rotor wake velocities outboard of the wing tips increase to maintain overall momentum in the wake. Between the two rotors and above the wing are another two regions of recirculating flow (as evidenced in Fig. 3 by localized areas of upwash and downwash). This is the well-known fountain flow region(s) for tiltrotor aircraft. This phenomena, and the implications of the derived rotor/wing interaction analysis regarding it, will be discussed in further detail later in the paper. Because of use of actuator disk modeling for the rotors, the rotor wake contraction downstream of the rotor plane -- and expansion upstream of the rotor disk -- is not captured in Fig. 3. This is not a significant compromise to the intended utility of the analysis as will be discussed.

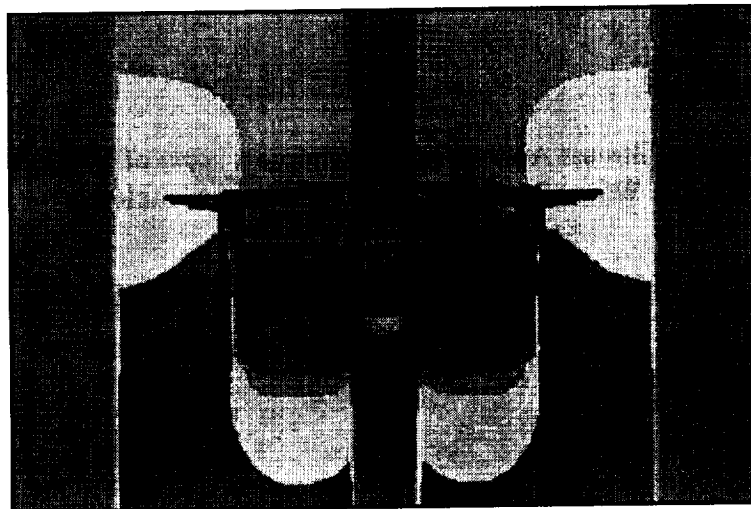


Fig. 3 -- Typical Flowfield (Vertical Velocity) Prediction of Rotor/Wing Interaction  
(velocities shown for a lateral plane through the rotor axes)

## Approach in Modeling Wing- and Rotor-on-Rotor Interactions

Only the rotors and wing of a tiltrotor aircraft are modeled in the analysis developed in this paper (Fig. 4). The tiltrotor fuselage and the nacelles are not modeled. As the primary focus of discussion in this paper will be on the effect of wing-on-rotor and rotor-on-rotor interactions on rotor performance, this is an acceptable modeling approach. Going one step further, tiltrotor aircraft are modeled in this analysis by a system of vortex cylinders and vortex sheets/surfaces that represent the wing and rotors. This simplified modeling approach for tiltrotor aircraft will be shown to yield acceptable results for rotor/wing interactions and their influence on rotor performance and mean inflow.

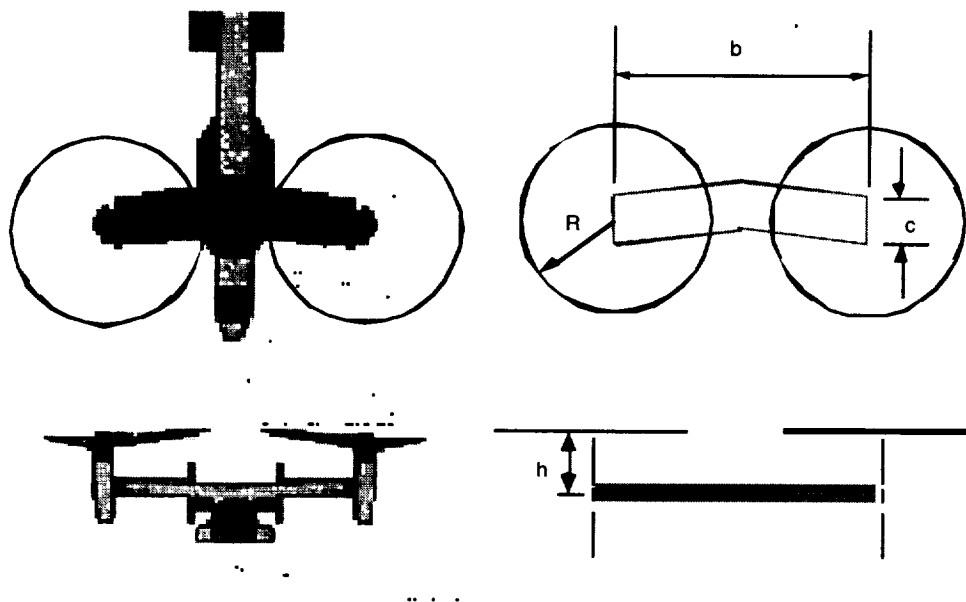


Fig. 4 -- Reduction of a Tiltrotor Aircraft into its Simplest Form of Modeling: Two Rotors and a Wing (Fuselage and Nacelles Not Modeled)

The rotor wake flowfield, as represented by the velocity vector  $\bar{v}$ , can be separated into two components:  $\bar{v}_R$ , the isolated rotor velocities, and,  $\Delta\bar{v}$ , the net rotor/wing interference velocities.

$$\bar{v} = \bar{v}_R + \Delta\bar{v} \quad (1)$$

The isolated rotor velocities,  $\bar{v}_R$ , are calculated by expressions derived later in this paper from actuator disk vortex theory. More sophisticated wake models are readily available,

but for the purposes of this paper, the simplicity of the actuator disk representation will suffice.

The modeling of the rotor/wing interference velocities,  $\Delta\bar{v}$ , is the key challenge underlying the analysis in this paper. This requires a novel approach in modeling the interactional influence of the wing in the rotor wake via 'vortex sheaths' -- a set of 'image' vortex surfaces that, in combination, satisfy the no-flow boundary condition at the wing surface (Fig. 5). There is one vortex sheath in each rotor wake. There are four vortex surfaces per 'sheath.' These vortex surfaces, in combination comprising the vortex sheaths, are referred to as 'image' vortex surfaces in deference to their analogous function as image vortices used in the classic method of images (such as used for wind tunnel wall corrections and rotor ground-effect interactions). The vortex sheath surface elements are comprised of convex and rectangular vortex sheets with circulation strength of nominally  $\gamma_{\text{sheet}}/\gamma \approx -2$ . ( $\gamma_{\text{sheet}}$  is the vortex sheet strength.  $\gamma$  is the rotor wake 'vortex cylinder' strength, or  $\gamma = \sqrt{C_T}/F\Omega R$ , where  $F=1/2$  for classic actuator disk vortex theory, but some value less than that when accounting for rotor/wing interactions). Semi-infinite line vortices are used to model the inboard blade-root trailed vortices and the resulting rotor wake swirl velocities. Employing this vortex sheath, image vortex system modeling, the Biot-Savart Law was used to analytically derive the induced velocity contribution of the rotor/wing interactions,  $\Delta\bar{v}$ , in the tiltrotor flowfield.

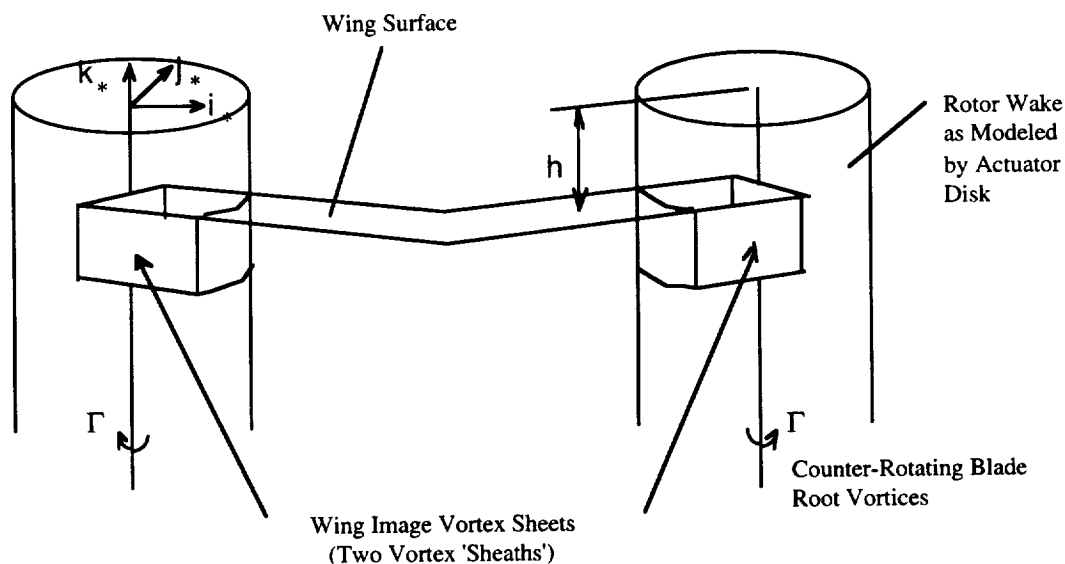


Fig. 5 -- Representing Rotors and Wing with a System of Vortex Elements

The main body of the paper will primarily discuss the computational results of the rotor/wing interaction modeling. The detailed derivation of analytical expressions for the rotor/wing interactions is presented in Appendix A. The general functional form of the analytical expressions for the induced velocities is given in Eq. 2a-b. Expressions for the

twenty-six terms in Eq. 2a-b ( $I_{R1}$ ,  $I_{R2}$ , etc.) are also derived and noted in Appendix A. These expressions will be comprised of both algebraic and elliptical integral functions. A key assertion regarding the rotor/wing interaction modeling derived in this paper -- that the required circulation strength of the vortex sheath is given by  $\gamma_{\text{sheet}}/\gamma \approx -2$ , so as to satisfy the no-flow boundary constraint at the wing surface -- is substantiated in Appendix B. This assertion (i.e.  $\gamma_{\text{sheet}}/\gamma \approx -2$ ) is validated by three different methods in Appendix B: a heuristic argument, a numerical treatment, and an approximate but analytical assessment. (In the latter case, a slightly more accurate analytical expression for  $\gamma_{\text{sheet}}$  is derived after much laborious algebraic effort.)

$$\begin{aligned} \bar{v}_R = & \left\{ \frac{\Gamma}{4\pi} I_{RR} - \frac{\gamma}{4\pi} (I_{R1} + I_{R2}) \right\} \bar{i}_* \\ & + \left\{ \frac{\Gamma}{4\pi} J_{RR} - \frac{\gamma}{4\pi} (J_{R1} + J_{R2}) \right\} \bar{j}_* \\ & - \frac{\gamma}{4\pi} (K_{R1} + K_{R2}) \bar{k}_* \end{aligned} \quad (2a)$$

$$\begin{aligned} \Delta \bar{v} = & \frac{-\gamma_{\text{Sheet}}}{4\pi} (I_{W11} + I_{W12} + I_{W13} + I_{W21} + I_{W22} + I_{W23}) \bar{i}_* \\ & - \frac{\gamma_{\text{Sheet}}}{4\pi} (J_{W11} + J_{W12} + J_{W13} + J_{W21} + J_{W22} + J_{W23}) \bar{j}_* \\ & - \frac{\gamma_{\text{Sheet}}}{4\pi} (K_{W11} + K_{W12} + K_{W13} + K_{W21} + K_{W22} + K_{W23}) \bar{k}_* \end{aligned} \quad (2b)$$

Using the analysis methodology as detailed in appendices A and B, an analytical assessment will now be made of the influence of various tiltrotor aircraft configuration parameters on rotor/wing interactions. In particular, the effect of rotor/wing offset distance, wing span and sweep, and flaperon incidence angles on rotor thrust will be examined. This assessment will also focus on the relative influences of wing-on-rotor versus rotor-on-rotor interactions. Wing-on-rotor interactions will be shown to primarily affect the distribution of rotor inflow in the rotor wake, but have a relatively small influence on mean inflow and rotor performance. Rotor-on-rotor interactions, on the other hand, primarily effect the mean inflow and overall rotor performance. The predictions from the derived analysis also reveal three-dimensional flow field features that have to date only been qualitatively measured for complete (full span, dual rotor) tiltrotor aircraft configurations.

The analytical work performed in this paper, along with the parametric investigations conducted with that analysis, yields a simple but powerful set of tools for tiltrotor aircraft preliminary design.

### Wing-On-Rotor Influences

Figure 6 presents a typical flow field prediction from the analytical work derived in this paper (see Appendix A). Figure 6 is contour plot of normalized rotor inflow (i.e.  $\lambda(r,\psi)/\bar{\lambda}$ ) at the rotor disk plane ( $z/R = 0$ ) for a typical tiltrotor aircraft configuration. The inflow distribution is normalized by the ideal, mean, isolated rotor inflow,  $\bar{\lambda}$ .

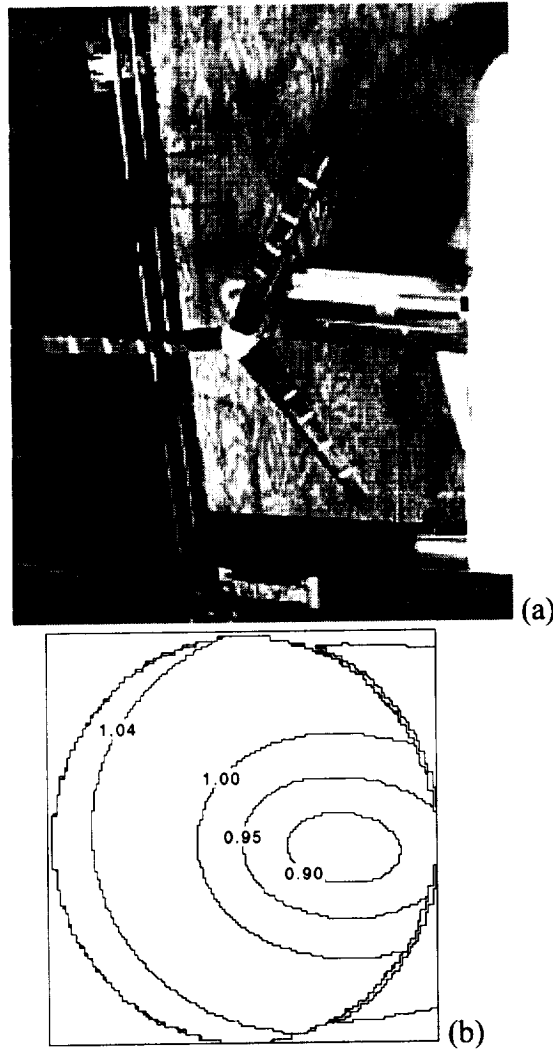


Fig. 6a-b - Left-Hand-Side Rotor: (a) Photograph of a Tiltrotor Model (Ref. 20) and (b) Predicted Normalized Rotor/Wing Inflow Distribution for that Rotor

The presence of the wing has a substantial impact on the rotor inflow distribution in Fig. 6. Over the wing, an inflow momentum deficit of approximately 10-15% is predicted.

The overall nature of the nonuniform inflow distribution is in relatively good agreement with the experimental hot-wire anemometry measurements of Ref. 6 and 11.

The predictions are consistent with the expected behavior of a tiltrotor aircraft hover flow field. Chief among the flow field features captured by this analysis are the ground and fountain effects previously noted in the literature (Refs. 3, 8, 11, and 12). The biggest source of discrepancy in the inflow correlation (in the rotor disk plane) is due to the use of the actuator disk modeling for  $\bar{v}_R$ , instead of more accurate rotor wake models. The results for  $\Delta\bar{v}$  appear to be qualitatively satisfactory as compared to empirical observations made in the literature. The vortex sheath, or wing image vortex, modeling of  $\Delta\bar{v}$  could be used in conjunction with more accurate isolated rotor wake models available in the literature to yield improved flow field results.

Perhaps the best known flow field characteristic for tiltrotor aircraft are the fountains (region of large flow recirculation) that form over the wing between the two rotors. It is essential for any analytical model to accurately predict this region of flow recirculation. Figure 7 is a streakline plot generated by the analytical model derived in this paper. The results are quite encouraging as the tiltrotor fountains are captured by the prediction.

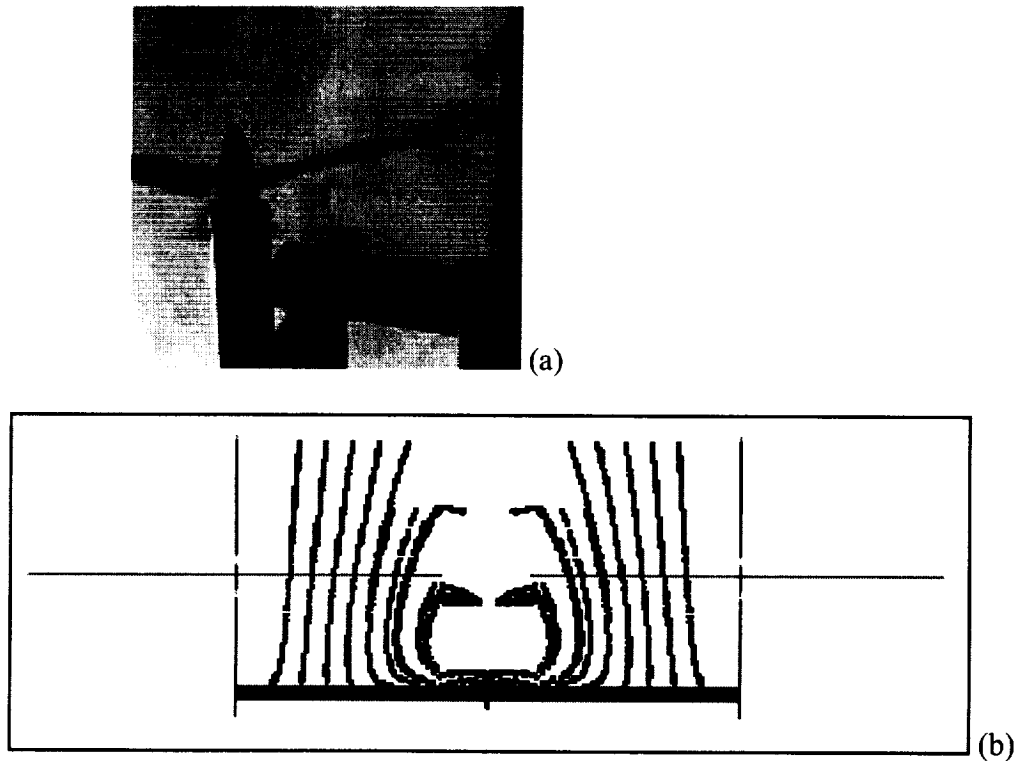


Fig. 7a-b - Tiltrotor Rotor/Wing Fountain Effect (for Left-Hand Rotor on the Retreating Side): (a) Experimental (Ref. 12) and (b) Predicted

Though a considerable body of qualitative observations exists, there is limited data in the literature suitable for quantitative correlation of analysis with experiment for the tiltrotor fountain effect. One of the best examples in the literature for observations of the fountain effect flow field is the shadowgraph work of Ref. 8. Analytical results clearly show that 'fountain flow' is essentially two flow mechanisms working in conjunction to affect the tiltrotor flowfield. The primary rotor/wing interaction has a distinct flow characteristic different from the secondary rotor/wing interaction. 'Fountain flow' is the sum total of the two distinct interactions.

Rotor inflow measurements close to the rotor disk were made using hot-wire anemometry for a small-scale, full-span dual-rotor tiltrotor model in hover in Ref. 6. Figures 8a-b compares predicted rotor inflow contour plots with the experimental hot-wire anemometry results from Ref. 6. The hot-wire measurements were made slightly upstream (above) the rotor disk, at  $z/R = 0.08$ . The analysis captures the general character of the rotor inflow distribution of the rotor/wing interaction. Discrepancies between the experimental data and the predictions are chiefly due to the analysis not modeling the impact on the inflow of tip losses, blade root cutout, and momentum deficit due to swirl near the rotor axis. This explains the major flow field differences along the rotor axis and the disk edge. More accurate isolated rotor hover wake models, for  $\bar{v}_R$ , could easily be used with the analytical expressions for  $\Delta\bar{v}$  to improve the overall correlation.

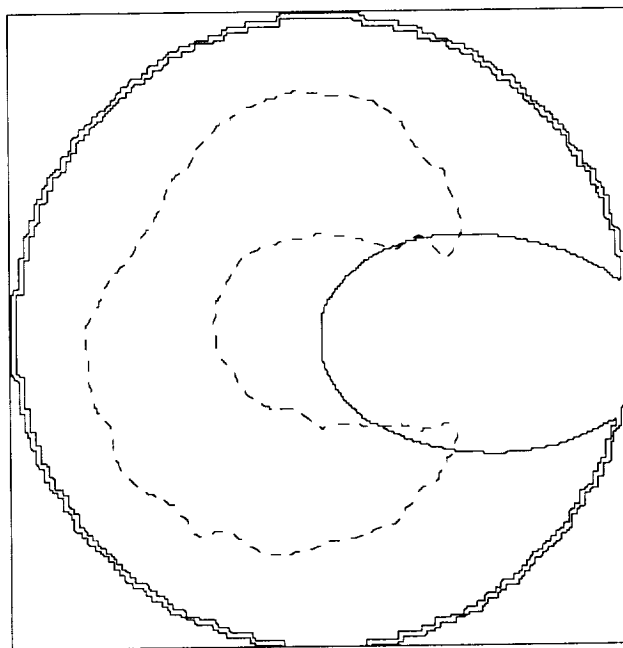


Fig. 8a - Nondimensional Rotor/Wing Interaction Velocities ( $z/R=0.08$ ,  $\lambda(r, \psi)/\bar{\lambda}=0.9$ ; left-hand-side rotor). Dashed line is experimental data (Ref. 6); solid line is predicted.

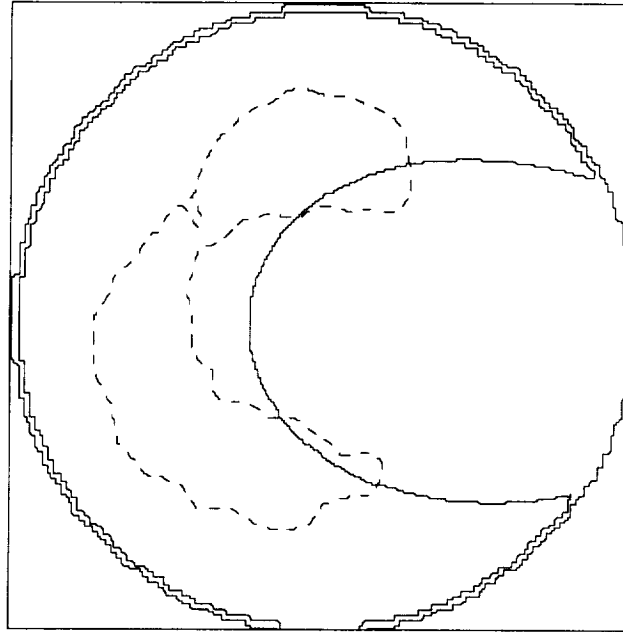


Fig. 8b - Nondimensional Rotor/Wing Interaction Velocities ( $z/R=0.08$ ,  $\lambda(r,\psi)/\bar{\lambda}=1.0$ )

Unfortunately, the velocity measurements could not be nondimensionalized with respect to the ideal hover inflow because rotor thrust was not measured for the Ref. 6 data. The experimental velocities as presented in Fig. 8a-b have been instead nondimensionalized by a reference velocity of 7 m/sec, which corresponds to an estimate of the nominal peak inflow value for the nonuniform distribution.

### **Rotor-on-Rotor Influences**

There is very little data in the literature regarding rotor-on-rotor interactions for side-by-side rotors where the influence of rotor proximity has been investigated. Figure 9 compares predictions of rotor thrust loss (due to rotor-on-rotor interactions) to experimental data from Ref. 3, for rotor and image-plane interactions. Figure 9 shows the resultant rotor thrust loss as the lateral distance between the rotor and image plane is varied. It is assumed in this discussion that a sufficiently large image plane, such as employed in Ref. 3, will simulate the gross effects of tiltrotor rotor-on-rotor interactions. This is a common assumption in tiltrotor hover performance experimental investigations. This assumption if correct allows that reasonable results can be derived from semispan rotor/wing testing, if an adequately large image plane is used, rather than requiring use of a full-span, dual-rotor test model. It would appear that predicted trend is in general agreement with the experimental data. Nonetheless, it is clear from Fig. 9 that the rotor thrust loss due to rotor-on-rotor (or rather rotor/image-plane) interactions is over-



predicted with respect to the Ref. 3 data as  $b/2R$  approaches unity (i.e. the rotor disks begin to overlap).

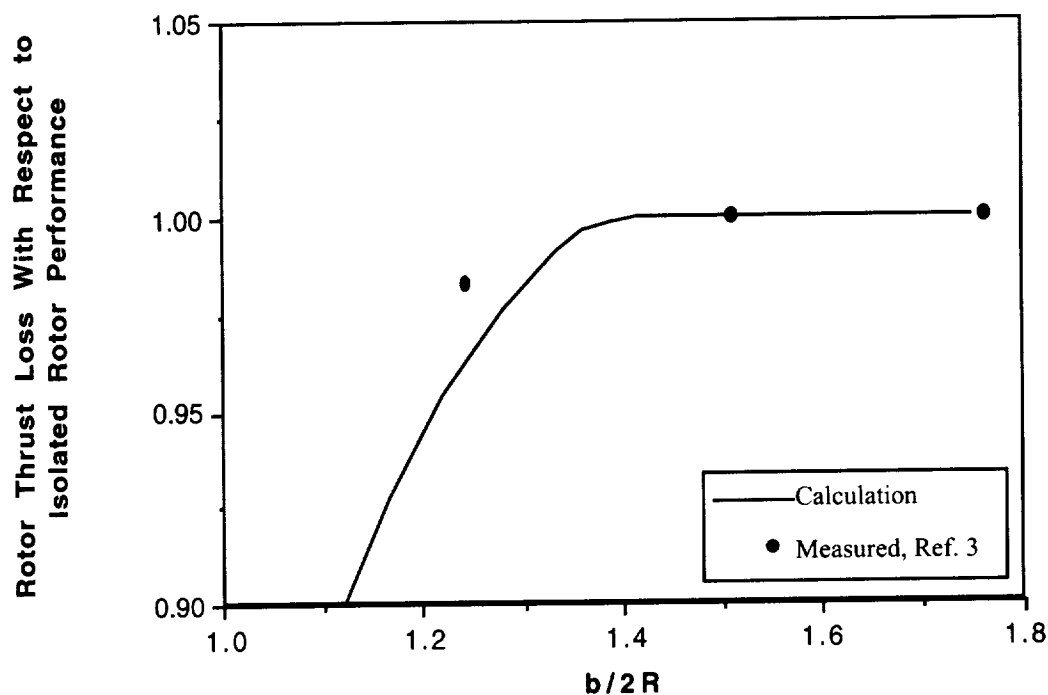


Fig. 9 - Influence of Rotor-on-Rotor (or, rather, Image-Plane-on-Rotor) Interaction on Rotor Performance

The key characteristic underlying the predicted rotor-on-rotor interaction is a re-assessment of rotor momentum theory as applied to tiltrotors (and side-by-side rotors in general) in hover. Reconsideration of the momentum theory problem for side-by-side rotors in close proximity would suggest (and has been accounted for in the analysis derived in Appendix A) that a wake skew angle in the upstream boundary condition needs to be included in the rotor hover momentum theory solution. Incorporation of such a wake skew angle results in a prediction of significant rotor thrust losses as side-by-rotors come into very close (but within the range of existent aircraft designs) proximity. Typical rotor-to-rotor lateral spacing for tiltrotor aircraft ranges from  $b/2R = 1.2868$  for the XV-15 tiltrotor research aircraft to  $b/2R = 1.2255$  for the V-22 Osprey. As suggested by Fig. 9, there can be a profound effect on installed (full vehicle) rotor performance -- as compared to an isolated rotor -- due to very close lateral spacing between two side-by-side rotors. Given the limited experimental data in the literature, a systematic experimental investigation to validate the influence of side-by-side rotor lateral spacing on tiltrotor hover performance is merited (particularly in the range  $1 \leq b/2R \leq 1.4$ ). Further, a new generation of isolated rotor and full-span tiltrotor wind tunnel models will hopefully enable precise quantitative measurements of tiltrotor interactional aerodynamics.

### Parametric Investigation of Rotor/Wing Interactions

Rotor thrust ratio trends are shown in Figs. 10-12 for rotor-to-wing offset distance, wing span, and wing flap incidence angle. Wing span (Fig. 10) has the greatest effect on rotor thrust. Rotor-to-wing offset distance (Fig. 11) and wing flap incidence angle (Fig. 12) have significantly less effect on rotor thrust. (The impact of wing flap incidence angles is assessed by defining an effective wing chord length that accounts for the flap deflection.) Similarly, very little effect of wing sweep on rotor thrust was seen, and so these results are not presented. The baseline parameters used in the Fig. 10-12 predictions are based on the nominal values for the V-22 aircraft: i.e.,  $b/2R = 1.2255$ ,  $R/h = 2.22$ ,  $c_o/R = 0.44$ ,  $\Lambda = 6$  degrees forward sweep, and  $\delta_{\text{flap}} = 70$  degrees trailing edge down. Figures 10-12 reflect parametric changes with respect to these baseline values.

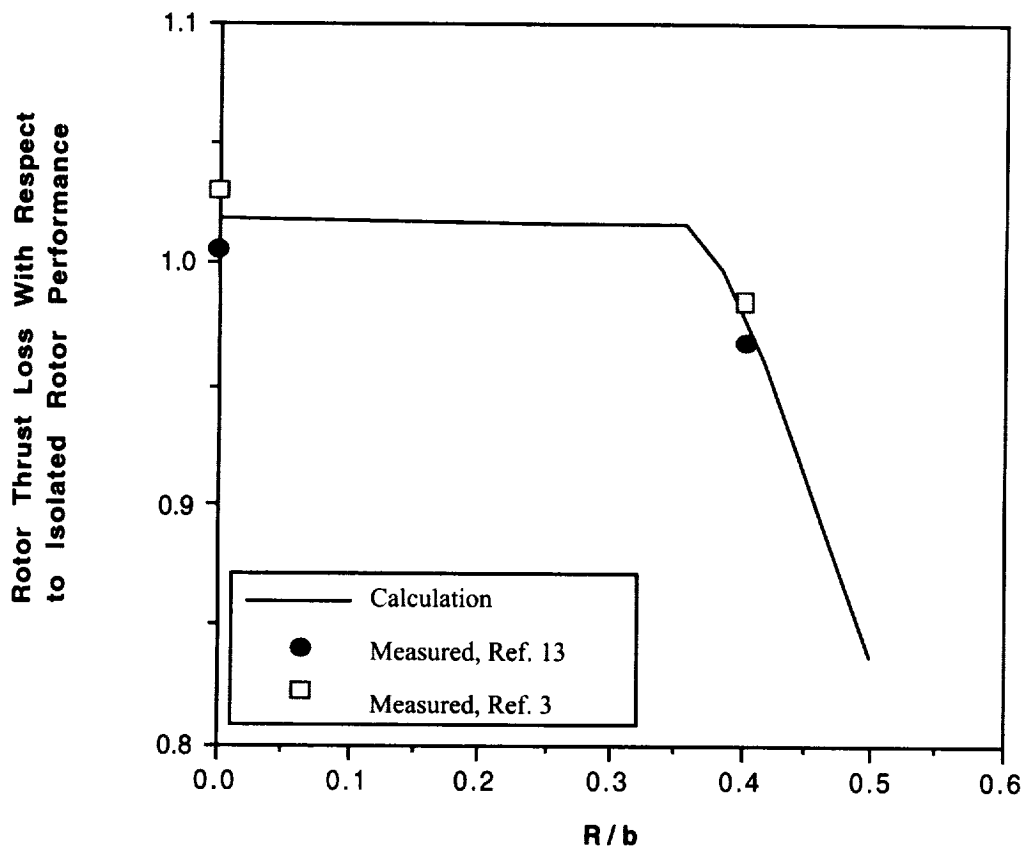


Fig. 10 - Influence of Wing Span on Rotor Performance. (Includes influence of both Wing- and Rotor-on-Rotor Interactions.)

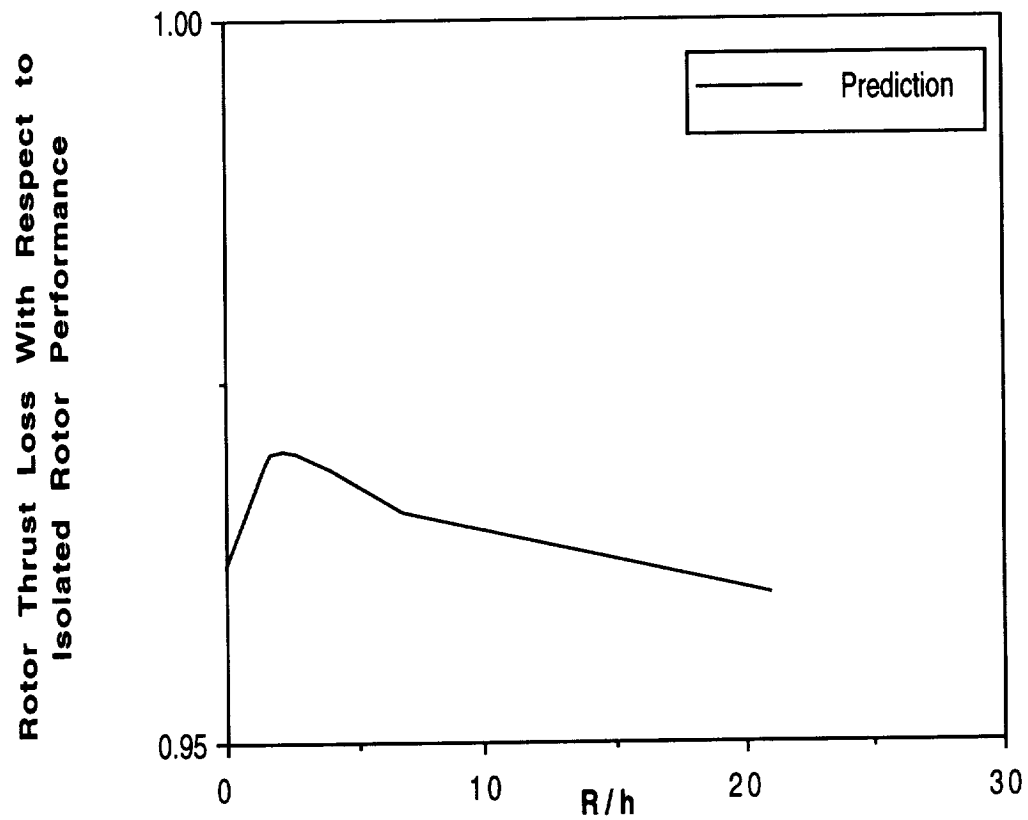


Fig. 11 - Influence of Rotor/Wing Offset Distance on Rotor Performance

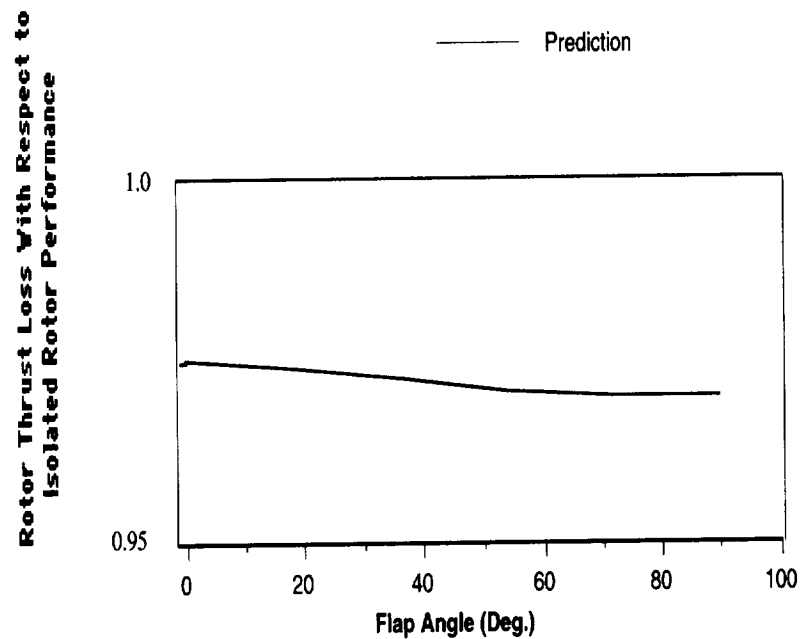


Fig. 12 - Influence of Wing Flaperon Incidence Angle on Rotor Performance

The biggest contribution to the wing span versus rotor thrust trend (Fig. 10) is due to the rotor-on-rotor interaction. The wing-on-rotor interaction contribution is of only secondary importance to the rotor thrust trend. This is because the induced axial velocity contribution from all the image vortex surface elements tends to negate each other's influence on the rotor disk mean inflow. The aircraft design implication of this rotor thrust loss trend is that there may be an incentive to go to higher aspect-ratio/wing-span wings for future tiltrotor aircraft.

Somewhat surprisingly, the offset distance between the rotor and wing has only a minor influence on rotor performance (Fig. 11). In contrast, the rotor/wing offset distance has a considerable effect on wing download (Ref. 2). The minimum thrust loss is predicted around  $R/h = 2.5$ , roughly the same rotor/wing offset as that on the V-22 aircraft. The thrust ratio for  $R/h \approx 2.5$  approaches the thrust loss level due solely to the rotor-on-rotor interaction.

An 'effective' wing chord length is used to account for the influence of wing flap incidence angles on rotor performance (Fig. 12). This definition of an effective wing chord length accounts for only planform area variations and does not take into account the vertical displacement of the image vortices with respect to the rotor disk due to flaperon deflection. The effective chord length, as used in this paper, is given by  $c = c_0(1 - x_{\text{flap}} \sin \delta_{\text{flap}})$ .

## Conclusions

An approximate, Biot-Savart law solution of the rotor/wing hover flow field has been derived. The effect of several important tiltrotor aircraft design parameters has been included in the rotor flow field predictions. The resulting analysis is computationally very efficient and accurate as to predicting rotor-on-rotor and wing-on-rotor interactions. Rotor/wing interactions have a substantial impact on the nonuniformity of the radial and azimuthal inflow distributions across the rotor disk. A new insight into the flow mechanisms underlying tiltrotor fountain flow has been gained. Analytical expressions have been derived for the influence of rotor/wing interactions on rotor thrust and mean inflow. This analysis includes the effect of a far-wake inflow skew angle from rotor-on-rotor interactions on rotor thrust.

A limited, but generally successful, correlation of analysis predictions with experimental data from the literature was performed. Improvements can be readily achieved by using more sophisticated rotor wake models in conjunction with the rotor/wing interaction

analysis developed in this paper. A study of the effect of various tiltrotor aircraft configuration parameters on rotor thrust in hover was performed. Wing-span (or rotor side-by-side lateral spacing) is extremely important as to its influence on the rotor-on-rotor interaction and, therefore, the rotor performance. All other parameters (rotor-to-wing offset distance, wing sweep, and flaperon incidence angle) have significantly less influence on rotor performance.

Results from this work will, hopefully, lead to the development of more sophisticated analytical treatments of the rotor/wing interaction problem, provide guidance for experimental investigations, and influence tiltrotor aircraft design.

### References

1. Taylor, M., "A Balsa-Dust Technique for Air-Flow Visualization and Its Application to Flow Through Model Helicopter Rotors in Static Thrust," NACA TN 2220.
2. McKee, J. and Naeseth, R., "Experimental Investigation of the Drag of Flat Plates and Cylinders in the Slipstream of a Hovering Rotor," NACA TN 4239.
3. Felker, F. and Light, J., "Rotor/Wing Aerodynamic Interactions in Hover," 42'nd Annual Forum of the American Helicopter Society, Washington, D.C., June 1986.
4. Clark, D., "Analysis of the Wing/Rotor and Rotor/Rotor Interactions Present in Tilt-Rotor Aircraft," U.S. Army Sponsored International Conference on Rotorcraft Basic Research, Durham, N.C. February 1985.
5. Fejtek, I., "Navier-Stokes Flowfield Computation of Wing/Rotor Interaction for a Tiltrotor Aircraft in Hover," NASA CR 4532, July 1993.
6. Coffen, C., "Tilt Rotor Hover Aeroacoustics," NASA CR 177598, June 1992.
7. Johnson, W., *Helicopter Theory*, Princeton University Press, 1980.
8. Swanson, A. and Light, J., "Shadowgraph Flow Visualization of Isolated Tiltrotor and Rotor/Wing Wakes," 48'th Annual Forum of the American Helicopter Society, Washington D.C., June 1992.
9. Gradshteyn, I. and Ryzhik, I., *Table of Integrals, Series, and Products, Fourth Edition*, Academic Press, New York & London, 1965.
10. Press, W.H., et. al., *Numerical Recipes: The Art of Scientific Computing*, Cambridge University Press, 1988.
11. Coffen, C. and George, A., "Analysis and Prediction of Tilt Rotor Hover Noise," 46'th Annual Forum of the American Helicopter Society, Washington, D.C., May 21-23, 1990.
12. Felker, F.F., Signor, D.B., Young, L.A., and Betzina, M.D., "Performance and Loads Data From a Hover Test of a 0.658-Scale V-22 Rotor and Wing," NASA TM 89419, April 1987.

13. Wood, T.L. and Peryea M.A., "Reduction of Tiltrotor Download," 49'th Annual Forum of the American Helicopter Society, St. Louis, Mo., May 19-21 1993.
14. Avallone, E.A. and Baumeister III, T., Editors., *Mark's Standard Handbook for Mechanical Engineers, Ninth Ed.*, McGraw-Hill, New York.
15. Beer, F.P. and Johnston, Jr., E.R., *Vector Mechanics for Engineers - Statics and Dynamics, Third Edition*, McGraw-Hill, New York, 1977.
16. Heyson, H., "An Evaluation of Linearized Vortex Theory as Applied to Single and Multiple Rotors Hovering In and Out of Ground Effect," NASA TN D-43, September 1959.
17. Roberson, J.A. and Crowe, C.T., *Engineering Fluid Mechanics*, Houghton Mifflin, Boston, 1975.
18. White, F.M., *Viscous Fluid Flow*, McGraw-Hill, 1974.
19. Rivlin, T.J., *An Introduction to the Approximation of Functions*, Dover Publications, Inc., New York, 1981.
20. Johnson, J.L. and Young, L.A., "Tilt Rotor Aeroacoustic Model Project," Confederation of European Aerospace Societies (CEAS) Forum on Aeroacoustics of Rotors and Propellers, Rome, Italy, June 9-11, 1999.

## Appendix A - Derivation of Rotor/Wing Interaction Model

### Nomenclature -- Appendices

b	Wing span; distance from rotor centerline to centerline (m)
c	Wing effective chord length with deflected flaperon, $c = c_0(1 - x_{\text{flap}} \sin \delta_{\text{flap}})$ , (m)
$c_0$	Wing chord length; flaperon not deflected, (m)
$C_T$	Rotor thrust coefficient, includes influence of rotor/wing interactional aerodynamics, $C_T = T/\pi\rho\Omega^2R^4$
$C_{T_I}$	Isolated rotor thrust coefficient, $C_{T_I} = T_I/\pi\rho\Omega^2R^4$
$C_{T_{RR}}$	Rotor thrust coefficient as influenced by rotor-on-rotor (or image-plane-on-rotor) interactions, $C_{T_{RR}} = T_{RR}/\pi\rho\Omega^2R^4$
$d\bar{s}_1, d\bar{s}_2,$ $d\bar{s}_3, d\bar{s}_4,$ $d\bar{s}_{n+4}$	Elemental surfaces used in Biot-Savart integration
F	Mean inflow interaction parameter ( $F=1/2$ for isolated rotor) that accounts for rotor-on-rotor and wing-on-rotor interactions on rotor thrust and mean inflow, $F = \frac{1}{2} + F_{RR} + F_{RW}$
$F_{RR}$	Parameter reflecting the net effect on mean rotor inflow of the rotor-on-rotor interaction
$F_{RW}$	Parameter reflecting the net effect on mean rotor inflow of the wing-on-rotor interactions
$F_{\text{Sheet}}$	Parameter reflecting the net effect of each image vortex sheet (of a total of eight rectangular sheets) representing the wing-on-rotor interaction contribution to the rotor mean inflow constant

$h$	Rotor-to-wing offset distance (m)
$\bar{i}, \bar{j}, \bar{k}$	Local Cartesian coordinates for Biot-Savart integration of rotor wake
$\bar{i}_*, \bar{j}_*, \bar{k}_*$	Global, fixed-frame, Cartesian coordinates; positive right, positive forward, and positive up, respectively
$I_{R1}, I_{R2}$	Actuator disk lateral velocity component contribution (global coordinates, $\bar{i}_*$ unit vector), from the left- and right-hand-side rotors (planform view) respectively, based on actuator disk theory
$J_{R1}, J_{R2}$	Actuator disk longitudinal velocity component contribution (global coordinates, $\bar{j}_*$ unit vector), from the left- and right-hand-side rotors respectively, based on actuator disk theory
$K_{R1}, K_{R2}$	Actuator disk vertical velocity component contribution (global coordinates, $\bar{k}_*$ unit vector), from the left- and right-hand-side rotors respectively, based on actuator disk theory
$I_{RR}$	Lateral velocity component contribution ( $\bar{i}_*$ unit vector) from the rotor blade root vortex and resulting swirl
$J_{RR}$	Longitudinal velocity component contribution ( $\bar{j}_*$ unit vector) from the rotor blade root vortex and resulting swirl
$I_{W11}, I_{W12}$ $I_{W13}, I_{W21}$ $I_{W22}, I_{W23}$	Lateral velocity component contributions from the left- and right-hand-side wing-on-rotor interactions (left and right side indicated by the first index; correspondingly, each left- and right-hand-side interaction has three contributing terms, as indicated by the second index)
$J_{W11}, J_{W12}$ $J_{W13}, J_{W21}$ $J_{W22}, J_{W23}$	Longitudinal velocity component contributions from the left- and right-hand-side wing-on-rotor interactions
$K_{W11}, K_{W12}$ $K_{W13}, K_{W21}$ $K_{W22}, K_{W23}$	Vertical velocity component contributions from the left- and right-hand-side wing-on-rotor interactions
$r$	Rotor radial coordinate, origin located at port rotor disk center
$R$	Rotor radius (m)
$R(z)$	Radial location of rotor wake slipstream boundary, where $R(0)=R$ (m)



$\bar{r}_1, \bar{r}_2,$ $\bar{r}_3, \bar{r}_4,$ $\bar{r}_{n+4}$	Position vectors used to define the relative location of an arbitrary reference point, P, with respect to the set of vortex surface elements used to define the rotor/wing interaction flow model
s	Portion of wing embedded in the rotor wake, $s = \sqrt{R^2 - \frac{c^2}{4} \cos^2 \Lambda}$
$t_n$	Integration limit for the n'th rectangular vortex sheet representing the wing interactions, (m)
$T_n$	Location of the n'th vortex sheet origin with respect to the local tangential coordinate, (m)
$T_I$	Isolated rotor thrust (N)
$T_{RR}$	Rotor thrust as influenced by rotor-on-rotor interactions (N)
T	Rotor thrust including wing-on-rotor & rotor-on-rotor interactions (N)
$T_*$	Independent variable to define, by integration, the mean inflow parameter, $F_{RW}$
$w(z)$	Vertical velocity component ( $\bar{k}_*$ unit vector) as a function of vertical axis coordinate, z (m/s)
$x_{flap}$	Flaperon length (m)
$x_n$	One of two translations required to transform coordinates of a reference point, P, from global to local coordinates of the n'th vortex sheet, (m)
$x_{wake}$	Upstream, far-wake, rotor slipstream centroid lateral offset distance from the rotor axis (m)
$y_n$	Second translation required (see $x_n$ ) to transform coordinates of a reference point, P, from global to local coordinates of the n'th vortex sheet, (m)
z	Vertical coordinate, origin located at port rotor disk center, positive up
Z	Vertical location of the rectangular image vortex sheet's origin with respect to the local tangential coordinate, (m)

$z_l$	Independent variable for integration of the Biot-Savart expression for actuator disk inflow
$\theta_n$	Rotation required to transform coordinates (see $x_n$ and $y_n$ ) of a reference point, P, from global to local coordinates of the n'th vortex sheet, (radians)
$\bar{\lambda}$	Mean inflow constant through rotor disk, including rotor/wing interactional aerodynamics (nondim.)
$\bar{\lambda}_{\text{wing surface}}$	Mean inflow constant at the wing surface, which has to be zero (no-flow boundary constraint)
$\lambda(r,\psi)$	Rotor inflow constant distribution as function of radial station and azimuth angle (nondim.)
$\bar{v}$ ,	Total rotor/wing induced velocities (m/sec)
$\bar{v}_R$	Isolated rotor induced velocities (m/sec)
$\Delta\bar{v}$	Net rotor/wing interference velocities (m/sec)
$\chi$	Wake skew angle (radians)
$\delta_{\text{flap}}$	Flaperon incidence angle (radians)
$\gamma$	Rotor wake vortex cylinder strength, $\gamma = \sqrt{C_T/F}\Omega R$ , ( $\text{m}^2/\text{sec}$ )
$\gamma_{\text{Shect}}$	Vortex sheath strength ( $\text{m}^2/\text{sec}$ )
$\Gamma$	Rotor wake bound vorticity strength, $\Gamma = 2\pi C_T \Omega R^2$ , ( $\text{m}^2/\text{sec}$ )
$\Lambda$	Wing sweep (radians)
$\eta_n$	Normal local coordinate (see $\tau$ and $\zeta$ ) of a reference point, P, with respect to n'th image vortex sheet representing the wing interaction, (m)
$\rho$	Atmospheric density ( $\text{kg}/\text{m}^3$ )
$\eta$ .	Independent variable for integration to define mean inflow parameter, $F_{RW}$

$\Omega$	Rotor rotational speed (radians/sec)
$\psi$	Rotor angular coordinate (azimuth angle), measured from line at rotor center, parallel to aircraft longitudinal axis, pointing aft (radians)
$\psi_L, \psi_T$	Angular coordinate location for the port wing leading- and trailing-edges, respectively (radians)
$\psi_1^*, \psi_2^*$	Independent variables for Biot-Savart law integration to define actuator disk induced velocities
$\tau$	For a vortex sheet (used to model the image vortices that represent the wing surface), one of two local, tangential coordinates (see $\zeta$ and $\eta_n$ ) used for Biot-Savart integration for the sheet induced velocity
$\tau_{n,k}$	Matrix containing elements that are integration limits that correspond to the vortex sheet Biot-Savart integration with respect to the independent variable, $\tau$
$\zeta$	For a vortex sheet (used to model the image vortices that represent the wing surface), the second local, tangential coordinate used for Biot-Savart integration for the sheet induced velocity
$\zeta_j$	Vector containing elements that are integration limits that correspond to the vortex sheet Biot-Savart integration with respect to the independent variable, $z$

## Description of Flowfield Modeling

The development of an analytical model for tiltrotor rotor/wing interactions in hover is foremost dependent upon the definition of a system of vortex surface elements that can accurately model the flow field. This modeling includes actuator disk vortex cylinder representations for the rotors, and rectangular sheets and convex surfaces for wing image vortex sheets that model the wing surface no-flow boundary condition. The analysis detailed in this paper relies heavily on an analogy with the Method of Images. The Method of Images has been used in the literature to model hovering rotors in ground effect (Fig. A1a) and can be used to model the influence of partial ground planes superimposed in rotor wakes (Fig. A1b). It will be shown (Fig. A1c) that vortex sheet modeling employing the Method of Images can be conceptually extended to the problem of rotor/wing interactions for tiltrotor aircraft in hover.

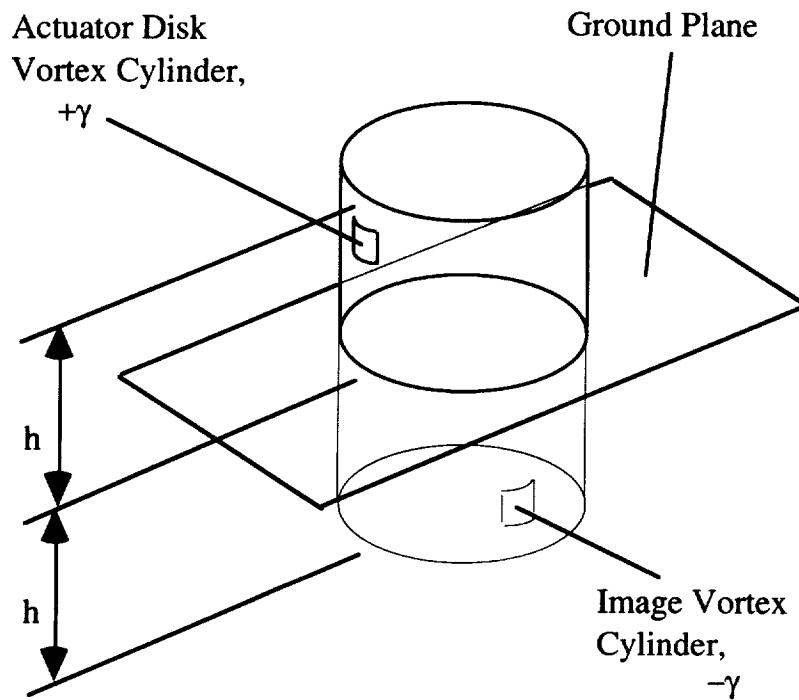


Fig. A1a - Conventional 'Method of Images' as Applied to Rotor Hover In Ground Effect

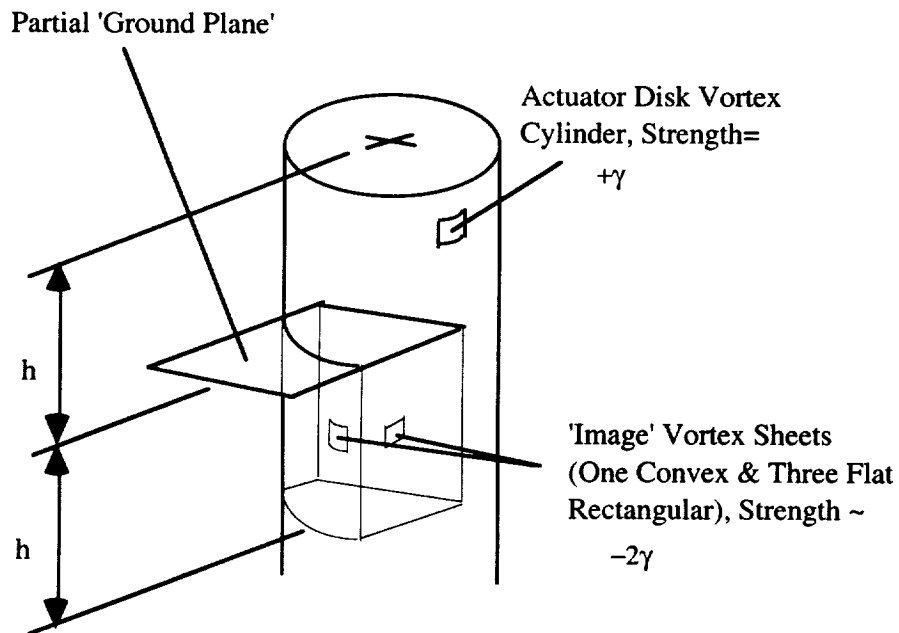


Fig. A1b - 'Method of Images' as Applied to a Partial 'Ground Plane'

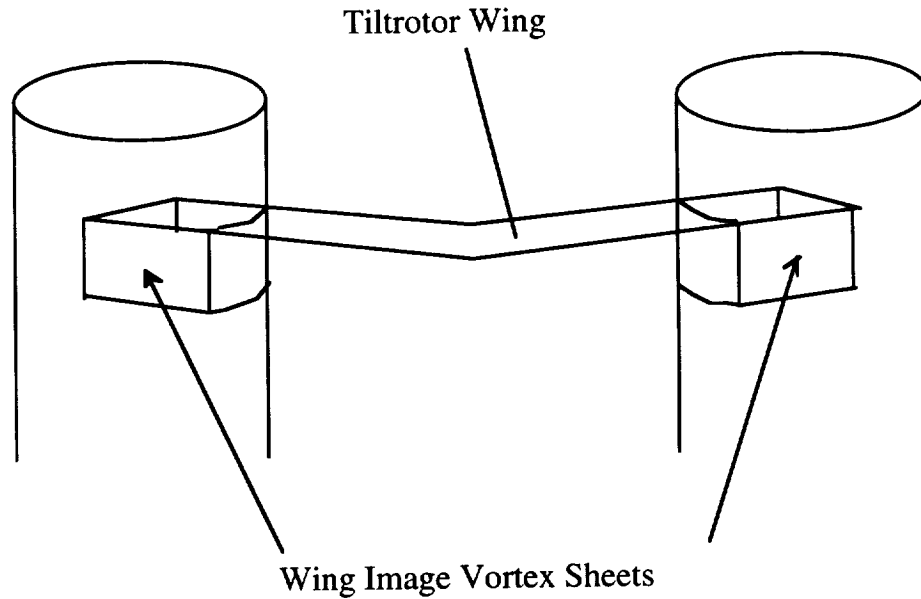


Fig. A1c - 'Method of Images' as Applied to a Tiltrotor Wing (Modeled as a Set of Two Partial 'Ground Planes')

Actuator disk modeling of the rotor wakes is employed in this paper for its analytical simplicity. The actuator disk distributed circulation strength is given by the well-known expression:  $\gamma = \sqrt{2C_T}\Omega R$  (see Ref. 7). In general, it should be noted for the rotor/wing interaction problem that  $C_T \neq C_{T_i}$ . This observation will be further discussed later in the paper when analytical expressions for the interactional aerodynamic influence of rotor-on-rotor and wing-on-rotor effects on rotor thrust and mean inflow are derived. The net effect of the rotor/wing interactions on rotor thrust and mean inflow is to require that  $\gamma = \sqrt{C_T/F}\Omega R$ , where the parameter  $F$  accounts for the rotor/wing interactional influence.  $F=1/2$  when the rotor/wing interaction is negligible.

As noted earlier a method of images analogy is employed in this paper to model the wing interactions with the rotor wake. This dictates that a 'vortex sheath' (a set of image vortex sheet/surfaces) is superimposed in the rotor wake to model the wing interaction, and that the vortex sheath has the circulation strength as defined by Eq. B28 (Appendix B) or  $\gamma_{\text{sheet}} \approx -2\gamma$ . For further discussion underlying the derivation of the vortex sheath circulation strength, refer to Appendix B.

Figure A2 depicts the vortex theory model used in this paper for rotor/wing interactions. This model simulates the flow field of a full-span, dual-rotor, tiltrotor aircraft configuration. Twelve vortex elements are used to model the tiltrotor aircraft hover rotor/wing interaction problem: two semi-infinite vortex cylinders; two semi-infinite,

counter-rotating, vortex lines; two convex (circular arc) image vortex surfaces; six flat, rectangular image vortex sheets. The convex surface and the flat rectangular vortex sheets as a whole constitute two vortex sheaths (Ref. 4). The global, fixed-frame, coordinates (units vectors of which are  $\bar{i}_*$ ,  $\bar{j}_*$ , and  $\bar{k}_*$ ) are shown as well as local coordinates (unit vectors are  $\bar{i}$ ,  $\bar{j}$ , and  $\bar{k}$ ) for the actuator disk (and the two convex image vortex surfaces) Biot-Savart integration. The global, fixed-frame, Cartesian coordinate system origin is co-located at the left-hand-side rotor's centerline at the disk plane. The lateral unit velocity vector is  $\bar{i}_*$ ; the longitudinal unit velocity vector is  $\bar{j}_*$ ; and the vertical unit velocity vector is  $\bar{k}_*$ . Also shown in Fig. A2 is the rotor blade root vortices; these manifest themselves as two semi-infinite counter-rotating vortex lines, with circulation  $\Gamma$ , aligned along the rotor/actuator disk axis. The semi-infinite rotor blade-root vortex circulation strength is given by the well-known expression:  $\Gamma = 2\pi C_T \Omega R^2$  (Ref. 7).

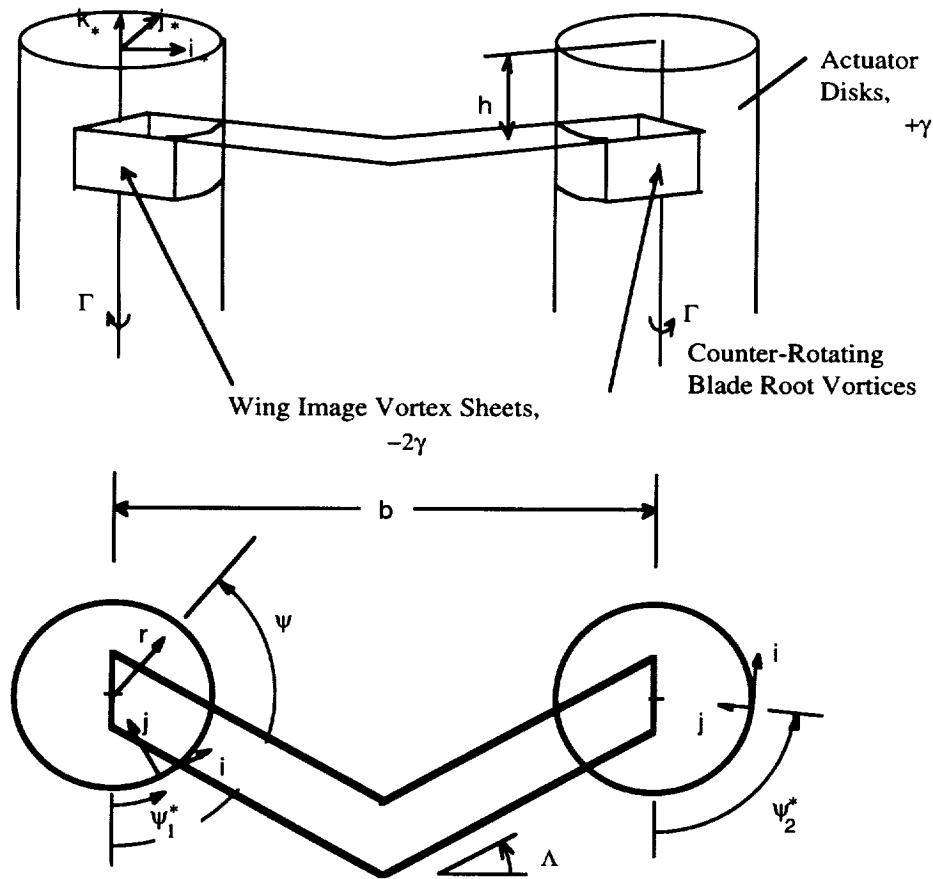


Fig. A2 - Vortex Theory Model

Clearly, a number of approximations have been made in the model shown in the Fig. A2. First, is the modeling of the wing interactions through use of uniform, distributed vorticity image vortex surfaces/sheets. Nothing *a priori* requires the assumption of uniformity of vortex sheet circulation strength. A second approximation is the actuator-disk representation of the rotor wake, and assuming that wake contraction is negligible. This 'no wake contraction' approximation may not be simplistic as first impression would suggest. Ref. 8 flow visualization results show the initial rotor wake contraction to be counterbalanced by a subsequent wake expansion as the rotor downwash impinges upon the wing. The tiltrotor wing is assumed to have a constant chord, uniformly swept wing; the wing tips are further assumed to extend to the rotor centerlines. The vortex model assumes a conventional tiltrotor aircraft configuration, so no blade overlap is allowed between the two rotors. Finally, the aircraft airframe is not modeled in the analysis. The fuselage interactional aerodynamic influence in hover is assumed of secondary importance compared to the rotor/wing interactions.

Analytical expressions are derived from the Biot-Savart law as applied to the twelve vortex elements used to model the tiltrotor aircraft rotor/wing interaction problem. Superposition of the induced velocities of the individual vortex elements gives the complete flow field solution. Ultimately, an expression is also derived for the mean influence of the rotor/wing interactions on rotor inflow and performance. This includes predictions of rotor-on-rotor and wing-on-rotor interactions -- including what has been referred to in the literature as the wing 'ground' and 'fountain' effects.

## Governing Equations

The rotor/wing induced velocities can be expressed in the form

$$\bar{v} = \bar{v}_R + \Delta\bar{v} \quad (A1)$$

The net induced velocity for the a tiltrotor aircraft in out-of-ground-effect hover is comprised of two components: the induced velocity from the rotors,  $\bar{v}_R$ , and the induced velocity components from the rotor/wing interaction,  $\Delta\bar{v}$ . The isolated rotor wake velocity and the rotor/wing interference velocity terms are respectively

$$\begin{aligned}\bar{v}_R = & -\frac{\gamma}{4\pi} \left[ \int_{-\infty}^0 \int_0^{2\pi} \frac{\bar{\mathbf{r}}_1 \times d\bar{\mathbf{s}}_1}{|\bar{\mathbf{r}}_1|^3} + \int_{-\infty}^0 \int_0^{2\pi} \frac{\bar{\mathbf{r}}_2 \times d\bar{\mathbf{s}}_2}{|\bar{\mathbf{r}}_2|^3} \right] \\ & + \frac{\Gamma}{4\pi} \left[ \int_{-\infty}^0 \frac{\bar{\mathbf{r}}_3 \times d\bar{\mathbf{s}}_3}{|\bar{\mathbf{r}}_3|^3} - \int_{-\infty}^0 \frac{\bar{\mathbf{r}}_4 \times d\bar{\mathbf{s}}_4}{|\bar{\mathbf{r}}_4|^3} \right]\end{aligned}\quad (\text{A2a})$$

$$\begin{aligned}\Delta\bar{v} = & \frac{-\gamma_{\text{Sheet}}}{4\pi} \left[ \int_{-h/2}^{h/2} \int_{\psi_T}^{\psi_L} \frac{\bar{\mathbf{r}}_1 \times d\bar{\mathbf{s}}_1}{|\bar{\mathbf{r}}_1|^3} + \int_{-h/2}^{h/2} \int_{2\pi-\psi_L}^{2\pi-\psi_T} \frac{\bar{\mathbf{r}}_2 \times d\bar{\mathbf{s}}_2}{|\bar{\mathbf{r}}_2|^3} \right] \\ & - \frac{\gamma_{\text{Sheet}}}{4\pi} \sum_{n=1}^6 \left[ \int_{-h/2}^{h/2} \int_{-t_n}^{+t_n} \frac{\bar{\mathbf{r}}_{n+4} \times d\bar{\mathbf{s}}_{n+4}}{|\bar{\mathbf{r}}_{n+4}|^3} \right]\end{aligned}\quad (\text{A2b})$$

where

$$\bar{\mathbf{r}}_1 = r \sin(\psi - \psi_1^*) \bar{\mathbf{i}} + (R - r \cos(\psi - \psi_1^*)) \bar{\mathbf{j}} + (z - z_1) \bar{\mathbf{k}} \quad (\text{A2c})$$

$$d\bar{\mathbf{s}}_1 = R d\psi_1^* dz_1 \bar{\mathbf{i}} \quad (\text{A2d})$$

$$\begin{aligned}\bar{\mathbf{r}}_2 = & \left[ (R \cos \psi_2^* - r \cos \psi) \sin \psi_2^* + (r \sin \psi - b - R \sin \psi_2^*) \cos \psi_2^* \right] \bar{\mathbf{i}} \\ & + \left[ (R \cos \psi_2^* - r \cos \psi) \cos \psi_2^* - (r \sin \psi - b - R \sin \psi_2^*) \sin \psi_2^* \right] \bar{\mathbf{j}} + (z - z_1) \bar{\mathbf{k}}\end{aligned}\quad (\text{A2e})$$

$$d\bar{\mathbf{s}}_2 = R d\psi_2^* dz_1 \bar{\mathbf{i}} \quad (\text{A2f})$$

$$\bar{\mathbf{r}}_3 = r \sin \psi \bar{\mathbf{i}} - r \cos \psi \bar{\mathbf{j}} + (z_1 - z) \bar{\mathbf{k}} \quad (\text{A2g})$$



$$d\bar{s}_3 = dz_1 \bar{k} \quad (A2h)$$

$$\bar{r}_4 = (r \sin \psi - b) \bar{i} - r \cos \psi \bar{j} + (z_1 - z) \bar{k} \quad (A2i)$$

$$d\bar{s}_4 = dz_1 \bar{k} \quad (A2j)$$

It should be noted that for  $\bar{r}_3$  and  $\bar{r}_4$  the relationship between the local and global coordinates is one to one; i.e.  $1\bar{i} = 1\bar{i}_*$ ,  $1\bar{j} = 1\bar{j}_*$ , and  $1\bar{k} = 1\bar{k}_*$ .

$$\bar{r}_{n+4} = (\tau - T_n) \bar{i} + \eta_n \bar{j} + (\zeta - Z) \bar{k} \quad (A2k)$$

$$d\bar{s}_{n+4} = d\tau d\zeta \bar{i} \quad (A2l)$$

The relationship between the local and global, fixed-frame coordinate systems will be discussed in detail later in the paper. The parameters  $T_n$  and  $Z$  define the local coordinate system origin of the  $n$ 'th vortex sheet (the origin is located in the center of the sheet). Expressions for  $T_n$  and  $Z$  will also be derived and discussed later in the paper. The vortex sheet dimension in the  $\bar{k}$  direction is a constant,  $h$ . The convex vortex surface integration limits  $\psi_L$  and  $\psi_T$  are given by (expressions derived from basic geometry and trigonometry considerations; see Fig. A3)

$$\psi_L = \frac{\pi}{2} - \Lambda + \sin^{-1} \left( \frac{c}{2R} \cos \Lambda \right) \quad (A2m)$$

$$\psi_T = \frac{\pi}{2} - \Lambda - \sin^{-1} \left( \frac{c}{2R} \cos \Lambda \right) \quad (A2n)$$

And, finally, as can be seen from work in Appendix B (Eq. B28), the image vortex sheets/surfaces that are used to model the wing surface no-flow boundary condition have a circulation strength given by Eq. A2o.

$$\frac{\gamma_{\text{sheet}}}{\gamma} = \frac{2\pi c s}{c_1} \left[ \sqrt{\frac{c_2^2 + x^2}{1 + x^2}} + \sqrt{1 + \left( \frac{c_2}{x} \right)^2} \right] \quad (A2o)$$

where

$$x \equiv h/R$$

$$c_1 = -4 \left( 1 + \frac{2}{\pi} \right) (cs + c_3 c^2)$$

$$c_2 = \left( \frac{c}{R} \right) \sqrt{\frac{4}{9} \left( 1 + \frac{2}{\pi} \right)^2 \left( 1 + c_3 \frac{c}{s} \right)^2 - 1}$$

$$c_3 \equiv \frac{1}{2} \left[ \frac{|b - 2s|}{\sqrt{(b - 2s)^2 + c^2}} - 1 \right]$$

$$s = \sqrt{R^2 - \frac{c^2}{4} \cos^2 \Lambda}$$

or

$$\gamma_{\text{sheet}} \approx -2\gamma$$

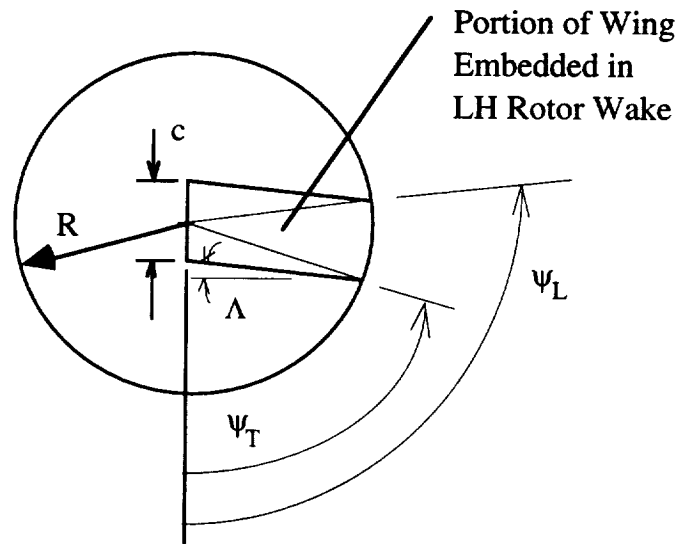


Fig. A3 - Definition of Wing Leading- and Trailing-Edge Integration Limits ( $\psi_L$  &  $\psi_T$ )

Equations A2a-o are based on Biot-Savart integrals for two semi-infinite vortex cylinders with positive circulation ( $+\gamma$ ), two convex (circular arc) vortex surfaces with negative

circulation (Eq. A2o or  $\gamma_{\text{Sheet}} \approx -2\gamma$ ), and two sets of three flat rectangular vortex sheets also with negative circulation (Eq. A2o or  $\gamma_{\text{Sheet}} \approx -2\gamma$ ). The Biot-Savart integrals for these respective vortex elements are well known in the literature. Each vortex element (cylinder, semi-infinite line, convex surface, or flat rectangular sheet) contributes to the induced velocity at a given point, P. The relative spatial orientation of point P to each vortex element is defined through use of position vectors:  $\vec{r}_1$ ,  $\vec{r}_2$ ,  $\vec{r}_3$ ,  $\vec{r}_4$ , and  $\vec{r}_{n+4}$ . (Note  $1 \leq n \leq 6$ ; this gives ten position vectors for twelve vortex elements; the convex vortex surfaces have the same position vectors as the vortex cylinders.) Refer to Fig. A4.

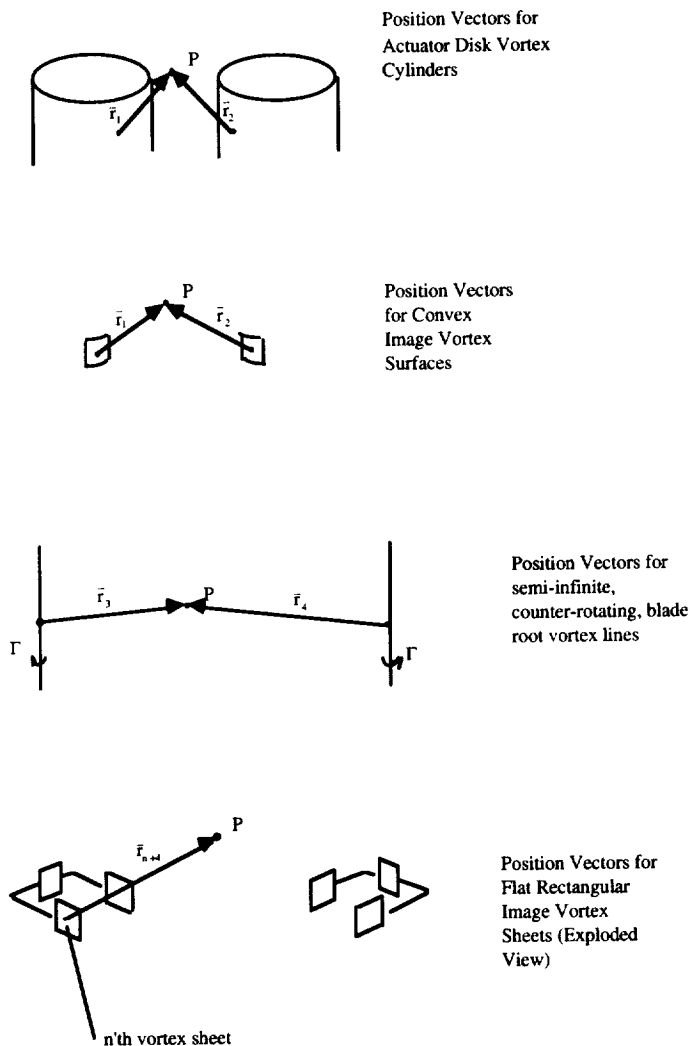


Fig. A4 - Biot-Savart Position Vectors

The solution of the above Biot-Savart equations (Eqs. A2a-b) will be shown to have the form

$$\begin{aligned}\bar{v}_R = & \left\{ \frac{\Gamma}{4\pi} I_{RR} - \frac{\gamma}{4\pi} (I_{R1} + I_{R2}) \right\} \bar{i}_* \\ & + \left\{ \frac{\Gamma}{4\pi} J_{RR} - \frac{\gamma}{4\pi} (J_{R1} + J_{R2}) \right\} \bar{j}_* \\ & - \frac{\gamma}{4\pi} (K_{R1} + K_{R2}) \bar{k}_*\end{aligned}\quad (A3a)$$

$$\begin{aligned}\Delta \bar{v} = & \frac{-\gamma_{Sheet}}{4\pi} (I_{W11} + I_{W12} + I_{W13} + I_{W21} + I_{W22} + I_{W23}) \bar{i}_* \\ & - \frac{\gamma_{Sheet}}{4\pi} (J_{W11} + J_{W12} + J_{W13} + J_{W21} + J_{W22} + J_{W23}) \bar{j}_* \\ & - \frac{\gamma_{Sheet}}{4\pi} (K_{W11} + K_{W12} + K_{W13} + K_{W21} + K_{W22} + K_{W23}) \bar{k}_*\end{aligned}\quad (A3b)$$

Or

$$\begin{aligned}\bar{v} = & \left\{ \frac{\Gamma}{4\pi} I_{RR} - \frac{\gamma}{4\pi} \left[ I_{R1} + I_{R2} + \left( \frac{\gamma_{Sheet}}{\gamma} \right) (I_{W11} + I_{W12} + I_{W13} + I_{W21} + I_{W22} + I_{W23}) \right] \right\} \bar{i}_* \\ & + \left\{ \frac{\Gamma}{4\pi} J_{RR} - \frac{\gamma}{4\pi} \left[ J_{R1} + J_{R2} + \left( \frac{\gamma_{Sheet}}{\gamma} \right) (J_{W11} + J_{W12} + J_{W13} + J_{W21} + J_{W22} + J_{W23}) \right] \right\} \bar{j}_* \\ & - \frac{\gamma}{4\pi} \left[ K_{R1} + K_{R2} + \left( \frac{\gamma_{Sheet}}{\gamma} \right) (K_{W11} + K_{W12} + K_{W13} + K_{W21} + K_{W22} + K_{W23}) \right] \bar{k}_*\end{aligned}\quad (A3c)$$

The induced velocity terms in Eqs. A3a-c ( $I_{R1}$ ,  $I_{R2}$ , etc.) are derived from integrating Eqs. A2a-b, given Eqs. A2c-o. This integration will be performed in subsequent sections of this paper.

## Solution for Rotor Induced Velocity Terms

### First (Left-Hand-Side) Rotor

This section will outline the derivation of Biot-Savart solutions for the induced velocity terms, as noted in Eq. A3a, for the actuator disk representation of the first (LHS) rotor.

$$\mathbf{I}_{R1} \bar{\mathbf{i}}_* + \mathbf{J}_{R1} \bar{\mathbf{j}}_* + \mathbf{K}_{R1} \bar{\mathbf{k}}_* \equiv \int_{-\infty}^0 \int_0^{2\pi} \frac{\bar{\mathbf{r}}_1 \times d\bar{\mathbf{s}}_1}{|\bar{\mathbf{r}}_1|^3} \quad (\text{A4})$$

Standard integral tables (Ref. 9) yields Eq. A5a-c for the integration of Eq. A4 (given Eq. A2a) with respect to  $z_1$ .

$$\int_L^U \int_{\phi_L}^{\phi_U} \frac{\bar{\mathbf{r}}_1 \times d\bar{\mathbf{s}}_1}{|\bar{\mathbf{r}}_1|^3} = \int_{\phi_L}^{\phi_U} \frac{4R(z_1 - z) [r \cos(\psi - \psi_1^*) - R] d\psi_1^*}{q \sqrt{r^2 + R^2 + (z_1 - z)^2 - 2rR \cos(\psi - \psi_1^*)}} \bar{\mathbf{k}} \bigg|_L^U - \int_{\phi_L}^{\phi_U} \frac{4R(a - 2z_1 z + z^2) d\psi_1^*}{q \sqrt{r^2 + R^2 + (z_1 - z)^2 - 2rR \cos(\psi - \psi_1^*)}} \bar{\mathbf{j}} \bigg|_L^U \quad (\text{A5a})$$

where  $\bar{\mathbf{r}}_1$  and  $d\bar{\mathbf{s}}_1$  have been defined by Eqs. A2c-d and while letting

$$\begin{aligned} a &= r^2 + R^2 + z^2 - 2rR \cos(\psi - \psi_1^*) \\ q &= 4[r^2 + R^2 - 2rR \cos(\psi - \psi_1^*)] \end{aligned} \quad (\text{A5b-c})$$

$U$  and  $L$  are arbitrary upper and lower integration limits (with respect to  $z_1$ ), and  $\phi_U$  and  $\phi_L$  are arbitrary limits with respect to integration for  $\psi_1^*$ . This approach to formulating the integral terms will be useful in defining not only the actuator disk vortex cylinder Biot-Savart solutions, but the convex image vortex surfaces used to partially model the

wing. Application of the integration limits for the actuator disk's semi-infinite vortex cylinder (i.e. letting  $U = 0$  and  $L = -\infty$  and  $\phi_U = 2\pi$  and  $\phi_L = 0$ ) yields the following

$$\begin{aligned}
\int_{-\infty}^0 \int_0^{2\pi} \frac{\bar{\mathbf{r}}_1 \times d\bar{\mathbf{s}}_1}{|\bar{\mathbf{r}}_1|^3} = & - \int_0^{2\pi} \frac{z[r \cos(\psi - \psi_1^*) - R]R d\psi_1^*}{[r^2 + R^2 - 2rR \cos(\psi - \psi_1^*)]\sqrt{r^2 + R^2 + z^2 - 2rR \cos(\psi - \psi_1^*)}} \bar{\mathbf{k}} \\
& + \int_0^{2\pi} \frac{[r \cos(\psi - \psi_1^*) - R]R d\psi_1^*}{[r^2 + R^2 - 2rR \cos(\psi - \psi_1^*)]} \bar{\mathbf{k}} \\
& - \int_0^{2\pi} \frac{\sqrt{r^2 + R^2 + z^2 - 2rR \cos(\psi - \psi_1^*)}R d\psi_1^*}{[r^2 + R^2 - 2rR \cos(\psi - \psi_1^*)]} \bar{\mathbf{j}} \\
& - \int_0^{2\pi} \frac{z^2 R d\psi_1^*}{[r^2 + R^2 - 2rR \cos(\psi - \psi_1^*)]\sqrt{r^2 + R^2 + z^2 - 2rR \cos(\psi - \psi_1^*)}} \bar{\mathbf{j}} \\
& + \int_0^{2\pi} \frac{2zR d\psi_1^*}{[r^2 + R^2 - 2rR \cos(\psi - \psi_1^*)]} \bar{\mathbf{j}}
\end{aligned}
\tag{A6}$$

Equation A6 is in terms of local coordinates (the unit vectors of which are  $\bar{\mathbf{i}}$ ,  $\bar{\mathbf{j}}$ , and  $\bar{\mathbf{k}}$ ) as defined in Fig. A2. A coordinate transformation to global coordinates ( $\bar{\mathbf{i}}_*$ ,  $\bar{\mathbf{j}}_*$ , and  $\bar{\mathbf{k}}_*$ ) is made to the above integral terms. The coordinate transformation required is:  $\bar{\mathbf{i}} = \cos \psi_1^* \bar{\mathbf{i}}_* + \sin \psi_1^* \bar{\mathbf{j}}_*$ ;  $\bar{\mathbf{j}} = -\sin \psi_1^* \bar{\mathbf{i}}_* + \cos \psi_1^* \bar{\mathbf{j}}_*$ ;  $\bar{\mathbf{k}} = \bar{\mathbf{k}}_*$ .

$$\begin{aligned}
\int_{-\infty}^0 \int_0^{2\pi} \frac{\bar{\mathbf{r}}_1 \times d\bar{\mathbf{s}}_1}{|\bar{\mathbf{r}}_1|^3} = & - \int_0^{2\pi} \frac{z[r \cos(\psi - \psi_1^*) - R]R d\psi_1^*}{[r^2 + R^2 - 2rR \cos(\psi - \psi_1^*)]\sqrt{r^2 + R^2 + z^2 - 2rR \cos(\psi - \psi_1^*)}} \bar{\mathbf{k}}_* \\
& + \int_0^{2\pi} \frac{[r \cos(\psi - \psi_1^*) - R]R d\psi_1^*}{[r^2 + R^2 - 2rR \cos(\psi - \psi_1^*)]} \bar{\mathbf{k}}_* \\
& - \int_0^{2\pi} \frac{\sqrt{r^2 + R^2 + z^2 - 2rR \cos(\psi - \psi_1^*)} R \cos \psi_1^* d\psi_1^*}{[r^2 + R^2 - 2rR \cos(\psi - \psi_1^*)]} \bar{\mathbf{j}}_* \\
& - \int_0^{2\pi} \frac{z^2 R \cos \psi_1^* d\psi_1^*}{[r^2 + R^2 - 2rR \cos(\psi - \psi_1^*)]\sqrt{r^2 + R^2 + z^2 - 2rR \cos(\psi - \psi_1^*)}} \bar{\mathbf{j}}_* \\
& + \int_0^{2\pi} \frac{2zR \cos \psi_1^* d\psi_1^*}{[r^2 + R^2 - 2rR \cos(\psi - \psi_1^*)]} \bar{\mathbf{j}}_* \\
& + \int_0^{2\pi} \frac{\sqrt{r^2 + R^2 + z^2 - 2rR \cos(\psi - \psi_1^*)} R \sin \psi_1^* d\psi_1^*}{[r^2 + R^2 - 2rR \cos(\psi - \psi_1^*)]} \bar{\mathbf{i}}_* \\
& + \int_0^{2\pi} \frac{z^2 R \sin \psi_1^* d\psi_1^*}{[r^2 + R^2 - 2rR \cos(\psi - \psi_1^*)]\sqrt{r^2 + R^2 + z^2 - 2rR \cos(\psi - \psi_1^*)}} \bar{\mathbf{i}}_* \\
& - \int_0^{2\pi} \frac{2zR \sin \psi_1^* d\psi_1^*}{[r^2 + R^2 - 2rR \cos(\psi - \psi_1^*)]} \bar{\mathbf{i}}_*
\end{aligned}
\tag{A7}$$

The integration, with respect to  $\psi_1^*$ , for the axial induced velocities is straightforward and takes advantage of the fact that the flow field is axisymmetric and uniform for an actuator disk. Therefore, the axial velocity integral terms can be evaluated at arbitrary radial and azimuthal locations -- in this case, for simplicity,  $r$  and  $\psi$  are set to zero. This approach yields the classic actuator disk axial velocity solution -- which, in the nomenclature of this paper, is denoted by the term  $K_{R1}$ .

$$K_{R1} = \pi \left\{ \frac{z}{\sqrt{R^2 + z^2}} - 1 \right\} \left[ 1 + \frac{R-r}{|R-r|} \right]
\tag{A8}$$

To complete the integral solution for the actuator disk for the radial and tangential velocities, in Eq. A7, it is necessary to impose two approximations. These

approximations consist of separating integrals into a combination of near- and far-field expressions that are then analytically tractable.

$$\int \frac{\sqrt{z^2 + g(\psi_1^*)} d\psi_1^*}{g(\psi_1^*)} \approx \int \frac{d\psi_1^*}{(1+|z|)\sqrt{g(\psi_1^*)}} + \int \frac{z d\psi_1^*}{g(\psi_1^*)} \quad (\text{A9a})$$

and

$$\int \frac{z^2 d\psi_1^*}{g(\psi_1^*)\sqrt{z^2 + g(\psi_1^*)}} \approx \int \frac{z d\psi_1^*}{g(\psi_1^*)} \quad (\text{A9b})$$

The function  $g(\psi_1^*)$  in Eqs. A9a-b is arbitrary, so as to illustrate the near- and far-field approximation. Applying this near- and far-field representation (Eqs. A9a-b) to Eq. A7 gives

$$\begin{aligned} \int_{-\infty}^0 \int_0^{2\pi} \frac{\bar{\mathbf{r}}_1 \times d\bar{\mathbf{s}}_1}{|\bar{\mathbf{r}}_1|^3} = & - \int_0^{2\pi} \frac{z[r \cos(\psi - \psi_1^*) - R]R d\psi_1^*}{[r^2 + R^2 - 2rR \cos(\psi - \psi_1^*)]\sqrt{r^2 + R^2 + z^2 - 2rR \cos(\psi - \psi_1^*)}} \bar{\mathbf{k}}_* \\ & + \int_0^{2\pi} \frac{[r \cos(\psi - \psi_1^*) - R]R d\psi_1^*}{[r^2 + R^2 - 2rR \cos(\psi - \psi_1^*)]} \bar{\mathbf{k}}_* \\ & - \int_0^{2\pi} \frac{R \cos \psi_1^* d\psi_1^*}{(1+|z|)\sqrt{r^2 + R^2 - 2rR \cos(\psi - \psi_1^*)}} \bar{\mathbf{j}}_* \\ & + \int_0^{2\pi} \frac{R \sin \psi_1^* d\psi_1^*}{(1+|z|)\sqrt{r^2 + R^2 - 2rR \cos(\psi - \psi_1^*)}} \bar{\mathbf{i}}_* \end{aligned} \quad (\text{A10})$$

The resultant integral solutions for Eq. A10 are in terms of complete elliptic integrals of the first and second kind,  $F(\pi/2, k)$  and  $E(\pi/2, k)$ , as shown below (see Ref. 9).



$$J_{R1} = \frac{(r+R)\cos\psi}{r(1+|z|)} \left\{ 2E\left(\frac{\pi}{2}, \frac{2\sqrt{rR}}{r+R}\right) - \left[ 1 + \left(\frac{r-R}{r+R}\right)^2 \right] F\left(\frac{\pi}{2}, \frac{2\sqrt{rR}}{r+R}\right) \right\} \quad (A11)$$

$$I_{R1} = \frac{(r+R)\sin\psi}{r(1+|z|)} \left\{ \left[ 1 + \left(\frac{r-R}{r+R}\right)^2 \right] F\left(\frac{\pi}{2}, \frac{2\sqrt{rR}}{r+R}\right) - 2E\left(\frac{\pi}{2}, \frac{2\sqrt{rR}}{r+R}\right) \right\} \quad (A12)$$

Numerical algorithms to estimate the complete elliptic integral expressions for  $I_{R1}$  and  $J_{R1}$  can be found in Ref. 10.

### **Second (Right-Hand-Side) Rotor**

Induced velocity solutions for the second (RHS) rotor can be readily found through analogy with the proceeding derived results for the left-hand rotor. The second rotor induced velocity terms are derivable from the double integral shown below (see also Eq. A2a).

$$I_{R2}\bar{\mathbf{i}}_* + J_{R2}\bar{\mathbf{j}}_* + K_{R2}\bar{\mathbf{k}}_* \equiv \int_{-\infty}^0 \int_0^{2\pi} \frac{\bar{\mathbf{r}}_2 \times d\bar{\mathbf{s}}_2}{|\bar{\mathbf{r}}_2|^3} \quad (A13)$$

The functional form of the above double integral for the second rotor is very similar to the integrals solved for the first rotor. Defining two new parameters:

$$r_0^2 = r^2 - 2br\sin\psi + b^2 \quad (A14a)$$

$$\psi_0 = \tan^{-1}\left(\frac{r\cos\psi}{r\sin\psi - b}\right) \quad (A14b)$$

Given these new parameters (Eq. A14a-b), the right-hand side rotor induced velocity terms can be noted.

$$K_{R2} = \pi \left\{ \frac{z}{\sqrt{R^2 + z^2}} - 1 \right\} \left[ 1 + \frac{R - \sqrt{r^2 - 2br \sin \psi + b^2}}{R - \sqrt{r^2 - 2br \sin \psi + b^2}} \right] \quad (A15)$$

$$J_{R2} = \frac{(r_0 + R) \cos \psi_0}{r_0(1 + |z|)} \left\{ 2E\left(\frac{\pi}{2}, \frac{2\sqrt{r_0 R}}{r_0 + R}\right) - \left[ 1 + \left(\frac{r_0 - R}{r_0 + R}\right)^2 \right] F\left(\frac{\pi}{2}, \frac{2\sqrt{r_0 R}}{r_0 + R}\right) \right\} \quad (A16)$$

$$I_{R2} = \frac{(r_0 + R) \sin \psi_0}{r_0(1 + |z|)} \left\{ \left[ 1 + \left(\frac{r_0 - R}{r_0 + R}\right)^2 \right] F\left(\frac{\pi}{2}, \frac{2\sqrt{r_0 R}}{r_0 + R}\right) - 2E\left(\frac{\pi}{2}, \frac{2\sqrt{r_0 R}}{r_0 + R}\right) \right\} \quad (A17)$$

### **Rotor Swirl Velocity Terms**

Finally, referring to Eq. A3a, the two remaining actuator disk induced velocity terms can now be solved for. The terms are defined by the relationship

$$I_{RR} \bar{\mathbf{i}}_* + J_{RR} \bar{\mathbf{j}}_* \equiv \int_{-\infty}^0 \frac{\bar{\mathbf{r}}_3 \times d\bar{\mathbf{s}}_3}{|\bar{\mathbf{r}}_3|^3} - \int_{-\infty}^0 \frac{\bar{\mathbf{r}}_4 \times d\bar{\mathbf{s}}_4}{|\bar{\mathbf{r}}_4|^3} \quad (A18)$$

Substituting Eqs. A2g-j into Eq. A18 -- and noting the relationship between the local and global coordinates is in this case one to one, i.e.,  $\bar{\mathbf{i}} = \bar{\mathbf{i}}_*$ ,  $\bar{\mathbf{j}} = \bar{\mathbf{j}}_*$ , and  $\bar{\mathbf{k}} = \bar{\mathbf{k}}_*$  -- gives

$$I_{RR} \bar{\mathbf{i}}_* + J_{RR} \bar{\mathbf{j}}_* = - \int_{-\infty}^0 \frac{r \cos(\psi) \bar{\mathbf{i}}_* + r \sin(\psi) \bar{\mathbf{j}}_*}{\sqrt{(r^2 + (z_1 - z)^2)^3}} dz_1 + \int_{-\infty}^0 \frac{r \cos(\psi) \bar{\mathbf{i}}_* + (r \sin(\psi) - b) \bar{\mathbf{j}}_*}{\sqrt{(r^2 - 2br \sin(\psi) + b^2 + (z_1 - z)^2)^3}} dz_1 \quad (A19)$$

The above integrals with respect to  $z_1$  can be found from standard handbooks. And, so, the Biot-Savart analytical solution for the pair of semi-infinite rotor blade root vortices is given by Eqs. A20 and A21.

$$I_{RR} = \frac{r \cos \psi}{r^2 - 2br \sin \psi + b^2} \left[ 1 - \frac{z}{\sqrt{r^2 - 2br \sin \psi + b^2 + z^2}} \right] - \frac{\cos \psi}{r} \left[ 1 - \frac{z}{\sqrt{r^2 + z^2}} \right] \quad (A20)$$

$$J_{RR} = \frac{1}{(r \sin \psi - b)} \left[ 1 - \frac{z}{\sqrt{r^2 - 2br \sin \psi + b^2 + z^2}} \right] - \frac{\sin \psi}{r} \left[ 1 - \frac{z}{\sqrt{r^2 + z^2}} \right] \quad (A21)$$

### Solution for Wing Interaction Induced Velocity Terms

The proceeding discussion outlined the derivation of the actuator disk contributions to the induced velocity distribution. To this point, for the most part, the analysis is essentially classic actuator vortex theory for rotors. In this section an analytical treatment is presented for the induced velocity terms for the rotor/wing interactions (Eq. A2b), i.e.  $\Delta \bar{V}$ . The analysis implicitly assumes that the wing is of moderate-to-high aspect ratio such that  $b > 2s$  and  $s \gg c$ .

Referring to Fig. A5, there are four vortex surfaces, for each rotor, that comprise the image vortex system that models the rotor/wing interaction. One of these image vortex surfaces is a convex surface that corresponds to the integrals (for the left- and right-hand side rotors respectively):

$$(I_{W11} + I_{W12}) \bar{i}_* + (J_{W11} + J_{W12}) \bar{j}_* + (K_{W11} + K_{W12}) \bar{k}_* \equiv \int_{-2h}^{-h} \int_{\psi_T}^{\psi_L} \frac{\bar{r}_1 \times d\bar{s}_1}{|\bar{r}_1|^3}$$

and

$$(I_{w21} + I_{w22})\bar{i}_* + (J_{w21} + J_{w22})\bar{j}_* + (K_{w21} + K_{w22})\bar{k}_* \equiv \int_{-2h}^{-h} \int_{2\pi-\psi_L}^{2\pi-\psi_T} \frac{\bar{r}_2 \times d\bar{s}_2}{|\bar{r}_2|^3} \quad (A22a-b)$$

Note the numbering of the first indice of above terms. The first indice denotes whether the term is for the 'first' (LHS) or 'second' (RHS) rotor's wake interaction with the wing surface. The three remaining image vortex surfaces are represented by flat, rectangular sheets. The Biot-Savart Law for a rectangular vortex sheet, with a single vorticity component, is given by the following integral expression (see Ref. 7, for example)

$$\frac{\gamma}{2\pi} \int_{-t_n}^{+t_n} \int_{-h/2}^{h/2} \frac{(\zeta - Z)\bar{j} - \eta_n \bar{k}}{\sqrt{[\eta_n^2 + (\tau - T_n)^2 + (\zeta - Z)^2]^3}} d\zeta d\tau \quad (A22c)$$

Equation A22c is arrived at by the substitution of Eqs. A2k-l into A2b.  $Z$  and  $T_n$  define the local origin of the each vortex sheet relative to the global coordinate system. The parameters  $\zeta$ ,  $\eta$ , and  $\tau$  are the vertical (along one sheet edge), normal, and tangential offset distances from each vortex sheet's origin to the point being evaluated (together they define the vortex sheet's position vector). The indice numbering system ( $n=1,2,3...6$ ) for each individual vortex sheet is outlined in Fig. A5. Later in the paper, when predicting the influence of rotor/wing interactions on rotor thrust and mean inflow, the convex vortex surfaces will be approximated/replaced by two additional flat rectangular vortex sheets; in that case (in total  $n=1,2,3...8$ ) sheets 7 and 8 will replace the convex surfaces.

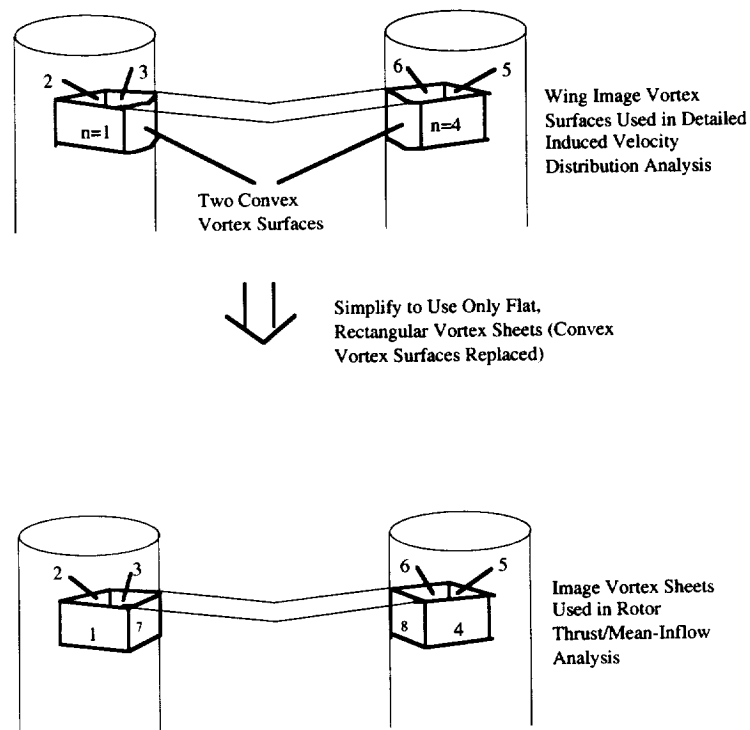


Fig. A5 - Types of Image Vortex Sheets Used to Model the Rotor/Wing Interaction and the Indice Numbering System Used to Identify the Vortex Sheets

### Convex Image Vortex Surfaces

Proceeding with the analytical solution for the convex vortex surfaces first (Eq. A22a-b), the integration with respect to the vertical axis,  $z_1$ , for arbitrary limits was presented earlier for a vortex cylinder (Eq. A5a-c). The convex surface element, representing a partial contribution of the wing interaction induced velocities, has the same general integration solution with respect to  $z_1$ . Therefore,

$$\begin{aligned}
\int_{-2h}^{-h} \int_{\psi_T}^{\psi_L} \frac{\bar{\mathbf{r}}_1 \times d\bar{\mathbf{s}}_1}{|\bar{\mathbf{r}}_1|^3} &= \int_{\psi_T}^{\psi_L} \frac{4R(z_1 - z)[r \cos(\psi - \psi_1^*) - R] d\psi_1^*}{q \sqrt{r^2 + R^2 + (z_1 - z)^2 - 2rR \cos(\psi - \psi_1^*)}} \bar{\mathbf{k}} \Big|_{-2h}^{-h} \\
&\quad - \int_{\psi_T}^{\psi_L} \frac{4R(a - 2z_1 z + z^2) d\psi_1^*}{q \sqrt{r^2 + R^2 + (z_1 - z)^2 - 2rR \cos(\psi - \psi_1^*)}} \bar{\mathbf{j}} \Big|_{-2h}^{-h}
\end{aligned} \tag{A23}$$

(In the above case, referring to Eq. A5a,  $U = -h$  and  $L = -2h$  for the upper and lower limits for integration with respect to  $z_1$ , and  $\phi_U = \psi_L$  and  $\phi_L = \psi_T$  for the integration with respect to  $\psi_1^*$ .) Applying the integration limits, transforming Eq. A23 to global coordinates ( $\bar{\mathbf{i}} = \cos \psi_1^* \hat{\mathbf{i}}_* + \sin \psi_1^* \hat{\mathbf{j}}_*$  ;  $\bar{\mathbf{j}} = -\sin \psi_1^* \hat{\mathbf{i}}_* + \cos \psi_1^* \hat{\mathbf{j}}_*$  ;  $\bar{\mathbf{k}} = \hat{\mathbf{k}}_*$ ), and simplifying gives

$$\begin{aligned}
\int_{-2h}^{-h} \int_{\psi_T}^{\psi_L} \frac{\bar{\mathbf{r}}_1 \times d\bar{\mathbf{s}}_1}{|\bar{\mathbf{r}}_1|^3} &= \int_{\psi_T}^{\psi_L} \frac{(2h + z)[r \cos(\psi - \psi_1^*) - R] R d\psi_1^*}{[r^2 + R^2 - 2rR \cos(\psi - \psi_1^*)] \sqrt{r^2 + R^2 + (2h + z)^2 - 2rR \cos(\psi - \psi_1^*)}} \bar{\mathbf{k}}_* \\
&\quad - \int_{\psi_T}^{\psi_L} \frac{(h + z)[r \cos(\psi - \psi_1^*) - R] R d\psi_1^*}{[r^2 + R^2 - 2rR \cos(\psi - \psi_1^*)] \sqrt{r^2 + R^2 + (h + z)^2 - 2rR \cos(\psi - \psi_1^*)}} \bar{\mathbf{k}}_* \\
&\quad + \int_{\psi_T}^{\psi_L} \frac{(a + 4hz + z^2) R \cos \psi_1^* d\psi_1^*}{[r^2 + R^2 - 2rR \cos(\psi - \psi_1^*)] \sqrt{r^2 + R^2 + (2h + z)^2 - 2rR \cos(\psi - \psi_1^*)}} \bar{\mathbf{j}}_* \\
&\quad - \int_{\psi_T}^{\psi_L} \frac{(a + 2hz + z^2) R \cos \psi_1^* d\psi_1^*}{[r^2 + R^2 - 2rR \cos(\psi - \psi_1^*)] \sqrt{r^2 + R^2 + (h + z)^2 - 2rR \cos(\psi - \psi_1^*)}} \bar{\mathbf{j}}_* \\
&\quad - \int_{\psi_T}^{\psi_L} \frac{(a + 4hz + z^2) R \sin \psi_1^* d\psi_1^*}{[r^2 + R^2 - 2rR \cos(\psi - \psi_1^*)] \sqrt{r^2 + R^2 + (2h + z)^2 - 2rR \cos(\psi - \psi_1^*)}} \bar{\mathbf{i}}_* \\
&\quad + \int_{\psi_T}^{\psi_L} \frac{(a + 2hz + z^2) R \sin \psi_1^* d\psi_1^*}{[r^2 + R^2 - 2rR \cos(\psi - \psi_1^*)] \sqrt{r^2 + R^2 + (h + z)^2 - 2rR \cos(\psi - \psi_1^*)}} \bar{\mathbf{i}}_*
\end{aligned} \tag{A24}$$

Because the arc length of the convex image vortex surfaces are very small compared to the circumference of the vortex cylinder, i.e.  $\psi_L - \psi_T \ll 2\pi$ , a simple approximation (based

on the mean value theorem) can be made for the integration of the convex surface with respect to  $\psi_1^*$ .

$$\int_L^U g(x) dx \approx (U - L)g(x)|_{x \rightarrow (U+L)/2} \quad \text{as} \quad U - L \rightarrow 0$$

Applied to Eq. A24, the approximation gives

$$\begin{aligned} \int_{-2h}^{-h} \int_{\psi_T}^{\psi_L} \frac{\bar{\mathbf{r}}_1 \times d\bar{\mathbf{s}}_1}{|\bar{\mathbf{r}}_1|^3} = & \frac{(2h+z)R(\psi_L - \psi_T)[r \cos(\psi - \psi_e) - R]}{[r^2 + R^2 - 2rR \cos(\psi - \psi_e)]\sqrt{r^2 + R^2 + (2h+z)^2 - 2rR \cos(\psi - \psi_e)}} \bar{\mathbf{k}}_* \\ & - \frac{(h+z)R(\psi_L - \psi_T)[r \cos(\psi - \psi_e) - R]}{[r^2 + R^2 - 2rR \cos(\psi - \psi_e)]\sqrt{r^2 + R^2 + (h+z)^2 - 2rR \cos(\psi - \psi_e)}} \bar{\mathbf{k}}_* \\ & + \frac{(e + 4hz + z^2)R \cos \psi_e (\psi_L - \psi_T)}{[r^2 + R^2 - 2rR \cos(\psi - \psi_e)]\sqrt{r^2 + R^2 + (2h+z)^2 - 2rR \cos(\psi - \psi_e)}} \bar{\mathbf{j}}_* \\ & - \frac{(e + 2hz + z^2)R \cos \psi_e (\psi_L - \psi_T)}{[r^2 + R^2 - 2rR \cos(\psi - \psi_e)]\sqrt{r^2 + R^2 + (h+z)^2 - 2rR \cos(\psi - \psi_e)}} \bar{\mathbf{j}}_* \\ & - \frac{(e + 4hz + z^2)R \sin \psi_e (\psi_L - \psi_T)}{[r^2 + R^2 - 2rR \cos(\psi - \psi_e)]\sqrt{r^2 + R^2 + (2h+z)^2 - 2rR \cos(\psi - \psi_e)}} \bar{\mathbf{i}}_* \\ & + \frac{(e + 2hz + z^2)R \sin \psi_e (\psi_L - \psi_T)}{[r^2 + R^2 - 2rR \cos(\psi - \psi_e)]\sqrt{r^2 + R^2 + (h+z)^2 - 2rR \cos(\psi - \psi_e)}} \bar{\mathbf{i}}_* \end{aligned} \quad (\text{A25a})$$

where

$$\psi_e = \frac{1}{2}(\psi_L + \psi_T) \quad (\text{A25b})$$

$$e = r^2 + R^2 + z^2 - 2rR \cos(\psi - \psi_e) \quad (\text{A25c})$$

Therefore, the induced velocities resulting from the convex vortex surface elements are given by the terms:

$$K_{w11} = \frac{(2h+z)(\psi_L - \psi_T)[r \cos(\psi - \psi_e) - R]R}{(r^2 + R^2 - 2rR \cos(\psi - \psi_e))\sqrt{r^2 + R^2 + (2h+z)^2 - 2rR \cos(\psi - \psi_e)}}$$

(A26a)

$$K_{w12} = \frac{-(h+z)(\psi_L - \psi_T)[r \cos(\psi - \psi_e) - R]R}{(r^2 + R^2 - 2rR \cos(\psi - \psi_e))\sqrt{r^2 + R^2 + (h+z)^2 - 2rR \cos(\psi - \psi_e)}}$$

(A26b)

$$J_{w11} = \frac{(e + 4hz + z^2)R \cos \psi_e (\psi_L - \psi_T)}{[r^2 + R^2 - 2rR \cos(\psi - \psi_e)]\sqrt{r^2 + R^2 + (2h+z)^2 - 2rR \cos(\psi - \psi_e)}}$$

(A26c)

$$J_{w12} = \frac{-(e + 2hz + z^2)R \cos \psi_e (\psi_L - \psi_T)}{[r^2 + R^2 - 2rR \cos(\psi - \psi_e)]\sqrt{r^2 + R^2 + (h+z)^2 - 2rR \cos(\psi - \psi_e)}}$$

(A26d)

$$I_{w11} = \frac{-(e + 4hz + z^2)R \sin \psi_e (\psi_L - \psi_T)}{[r^2 + R^2 - 2rR \cos(\psi - \psi_e)]\sqrt{r^2 + R^2 + (2h+z)^2 - 2rR \cos(\psi - \psi_e)}}$$

(A26e)



$$I_{w12} = \frac{(e + 2hz + z^2)R \sin \psi_e (\psi_L - \psi_T)}{\left[ r^2 + R^2 - 2rR \cos(\psi - \psi_e) \right] \sqrt{r^2 + R^2 + (h + z)^2 - 2rR \cos(\psi - \psi_e)}} \quad (A26f)$$

Analogously, the induced velocity term for the second convex image vortex surface can be solved by the same general method as outlined for the first convex surface. Therefore, the solutions for the rotor/wing interactions (due to the convex, image vortex sheet) from the left-hand side rotor and wing are

$$K_{w21} = \frac{-(2h + z)(\psi_L - \psi_T) \{ (R \cos \psi_e - r \cos \psi) \cos \psi_e + (R \sin \psi_e - b + r \sin \psi) \sin \psi_e \} R}{f \sqrt{f + (2h + z)^2}} \quad (A27a)$$

$$K_{w22} = \frac{(h + z)(\psi_L - \psi_T) \{ (R \cos \psi_e - r \cos \psi) \cos \psi_e + (R \sin \psi_e - b + r \sin \psi) \sin \psi_e \} R}{f \sqrt{f + (h + z)^2}} \quad (A27b)$$

$$J_{w21} = \frac{(f + 4hz + 2z^2)R \cos \psi_e (\psi_L - \psi_T)}{f \sqrt{f + (2h + z)^2}} \quad (A27c)$$

$$J_{w22} = \frac{-(f + 2hz + 2z^2)R \cos \psi_e (\psi_L - \psi_T)}{f \sqrt{f + (h + z)^2}} \quad (A27d)$$

$$I_{w21} = \frac{(f + 4hz + 2z^2)R \sin \psi_e (\psi_L - \psi_T)}{f \sqrt{f + (2h + z)^2}} \quad (A27e)$$

$$I_{w22} = \frac{-(f + 2hz + 2z^2)R \sin \psi_e (\psi_L - \psi_T)}{f \sqrt{f + (h + z)^2}} \quad (A27f)$$

where

$$f = r^2 + b^2 + R^2 - 2b[R \sin \psi_e + r \sin \psi] - 2rR \cos(\psi + \psi_e) \quad (A27g)$$

### **Rectangular Image Vortex Sheets**

To complete the solution for rotor/wing interactions it is now necessary to estimate the induced velocity contributions from the rectangular vortex sheet elements (Eqs. A2a and A3a). These are the terms  $I_{w13}$ ,  $I_{w23}$ ,  $J_{w13}$ ,  $J_{w23}$ ,  $K_{w13}$ , and  $K_{w23}$ . Biot-Savart integrals for flat rectangular vortex sheets -- with uniform distributed vorticity -- are in the literature and are given in terms of local coordinates, normal and parallel to the sheet surface, with the origin at the center of the sheet (Ref. 7). Transformation of the vortex sheet Biot-Savart solutions to global coordinates is necessary in order to define the induced velocity contribution for each individual vortex sheet to the overall rotor/wing interaction

$$Z = \left( z + \frac{3}{2}h \right) \quad (A28a)$$

$$\eta_n = \left[ r \sin\left(\frac{3}{2}\pi + \psi\right) - y_n \right] \cos \theta_n - \left[ r \cos\left(\frac{3}{2}\pi + \psi\right) - x_n \right] \sin \theta_n \quad (A28b)$$

$$T_n = \left[ r \sin\left(\frac{3}{2}\pi + \psi\right) - y_n \right] \sin \theta_n + \left[ r \cos\left(\frac{3}{2}\pi + \psi\right) - x_n \right] \cos \theta_n \quad (A28c)$$

The local coordinate vectors (for each individual vortex sheet) are transformed to the global Cartesian coordinates by

$$\bar{i} = \cos \theta_n \bar{i}_* - \sin \theta_n \bar{j}_* \quad (\text{A29a})$$

$$\bar{j} = \sin \theta_n \bar{i}_* + \cos \theta_n \bar{j}_* \quad (\text{A29b})$$

$$\bar{k}_* = \bar{k} \quad (\text{A29c})$$

To complete the local to global coordinate transformations as dictated by Eqs. A28a-c and A29a-c -- as applied to Eq. A22c -- it is necessary to define the rotation and translation vectors  $\theta$ ,  $x$ , and  $y$ ; it is also necessary to define the integration limit vector,  $t$ , used in Eq. A22c. Refer to Fig. A6.

$$\theta = \begin{bmatrix} 2\pi - \Lambda \\ \frac{3}{2}\pi \\ \pi - \Lambda \\ \Lambda \\ \frac{1}{2}\pi \\ \pi + \Lambda \\ \frac{\pi}{2} - \Lambda \\ \frac{3\pi}{2} + \Lambda \end{bmatrix} \quad t = \begin{bmatrix} \frac{1}{2}R \\ \frac{1}{2}c \\ \frac{1}{2}R \\ \frac{1}{2}R \\ \frac{1}{2}c \\ \frac{1}{2}R \\ \frac{c}{2}\cos\Lambda \\ \frac{c}{2}\cos\Lambda \end{bmatrix} \quad (\text{A30a-b})$$

$$x = \begin{bmatrix} \frac{1}{2}R\cos\Lambda \\ 0 \\ \frac{1}{2}R\cos\Lambda \\ b - \frac{1}{2}R\cos\Lambda \\ b \\ b - \frac{1}{2}R\cos\Lambda \\ R\cos\Lambda \\ b - R\cos\Lambda \end{bmatrix} \quad y = \begin{bmatrix} -\frac{1}{2}(c + R\sin\Lambda) \\ 0 \\ \frac{1}{2}(c - R\sin\Lambda) \\ -\frac{1}{2}(c + R\sin\Lambda) \\ 0 \\ \frac{1}{2}(c - R\sin\Lambda) \\ -R\sin\Lambda \\ -R\sin\Lambda \end{bmatrix} \quad (\text{A30c-d})$$

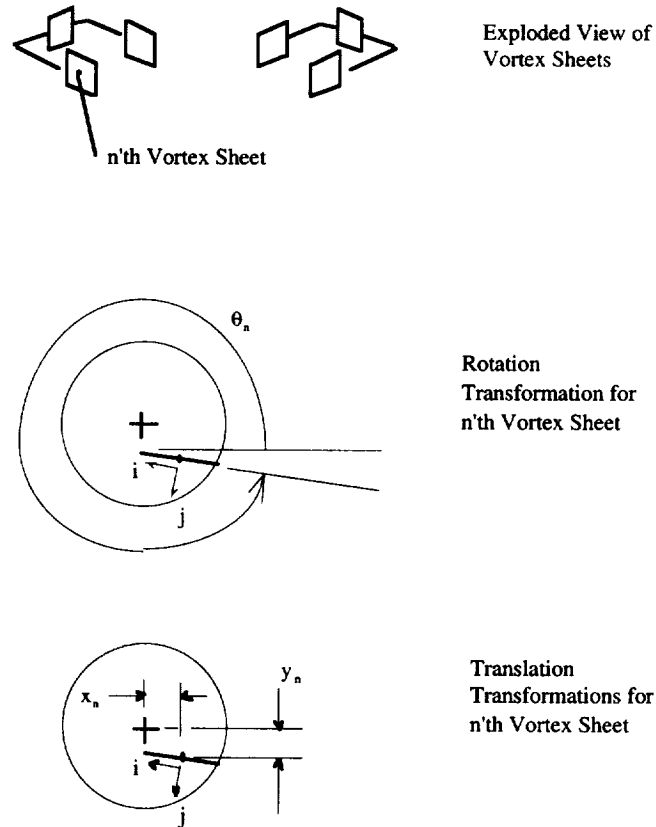


Fig. A6 - Transformations From n'th Vortex Sheet Local Coordinates to Global Coordinates

Note that  $1 \leq n \leq 6$  to complete the Biot-Savart solution for the remaining flat, rectangular vortex sheets. However, as clearly seen below, there are  $n=8$  elements in each of the Eq. A30a-d vectors. The reason for these additional vector elements,  $n = 7$  and  $8$ , is that later in this paper, in deriving the wing-on-rotor influence on rotor thrust and mean inflow, the convex image vortex surfaces will be replaced for simplicity sake by flat, rectangular sheets. The vectors  $\theta$ ,  $t$ ,  $x$ , and  $y$  have been defined with this in mind.

As noted earlier with Eq. A2b, repeated below for convenience, the induced velocities from the rotor/wing interactions are:

$$\Delta \bar{V} = \frac{-\gamma_{\text{Sheet}}}{4\pi} \left[ \int_{-h/2}^{h/2} \int_{\psi_T}^{\psi_L} \frac{\bar{\mathbf{r}}_1 \times d\bar{\mathbf{s}}_1}{|\bar{\mathbf{r}}_1|^3} + \int_{-h/2}^{h/2} \int_{2\pi-\psi_L}^{2\pi-\psi_T} \frac{\bar{\mathbf{r}}_2 \times d\bar{\mathbf{s}}_2}{|\bar{\mathbf{r}}_2|^3} \right] \quad (\text{A2b})$$

$$- \frac{\gamma_{\text{Sheet}}}{4\pi} \sum_{n=1}^6 \left[ \int_{-h/2}^{h/2} \int_{-t_n}^{+t_n} \frac{\bar{\mathbf{r}}_{n+4} \times d\bar{\mathbf{s}}_{n+4}}{|\bar{\mathbf{r}}_{n+4}|^3} \right]$$

The last integral term in Eq. A2b (see also Eq. A22c) is the contribution from the six rectangular image vortex sheets that model, in part, the wing-on-rotor interaction (The sum total of induced velocities from the eight image vortex sheets satisfies a mean no-flow boundary constraint at the wing surface.) Reference 4 described a similar flow modeling approach as a ‘vortex sheath.’

Substituting Eqs. A2k-l into A2b, and making the local to global coordinate transformations represented by Eqs. A29a-c, gives

$$\sum_{n=1}^6 \left[ \int_{-h/2}^{h/2} \int_{-t_n}^{+t_n} \frac{\bar{\mathbf{r}}_{n+4} \times d\bar{\mathbf{s}}_{n+4}}{|\bar{\mathbf{r}}_{n+4}|^3} \right] = \sum_{n=1}^6 \left[ \int_{-t_n}^{+t_n} \int_{-h/2}^{h/2} \frac{(\zeta - Z)\bar{\mathbf{j}} - \eta_n \bar{\mathbf{k}}}{\sqrt{(\eta_n^2 + (\tau - T_n)^2 + (\zeta - Z)^2)^3}} d\zeta d\tau \right]$$

$$= \sum_{n=1}^6 \left[ \int_{-h/2}^{h/2} \int_{-t_n}^{+t_n} \frac{(\zeta - Z)\sin\theta_n \bar{\mathbf{i}}_* + (\zeta - Z)\cos\theta_n \bar{\mathbf{j}}_* - \eta_n \bar{\mathbf{k}}_*}{\sqrt{(\eta_n^2 + (\tau - T_n)^2 + (\zeta - Z)^2)^3}} d\tau d\zeta \right] \quad (\text{A31})$$

Integration of Eq. A31, with respect to  $\tau$  (one of the two local, tangential coordinates along the vortex sheet surface), gives

$$\int_{-h/2}^{h/2} \int_{-t_n}^{+t_n} \frac{(\zeta - Z)\sin\theta_n \bar{\mathbf{i}}_* + (\zeta - Z)\cos\theta_n \bar{\mathbf{j}}_* - \eta_n \bar{\mathbf{k}}_*}{\sqrt{(\eta_n^2 + (\tau - T_n)^2 + (\zeta - Z)^2)^3}} d\tau d\zeta =$$

$$\int_{-h/2}^{h/2} \left[ \frac{(\tau - T_n)[(\zeta - Z)\sin\theta_n \bar{\mathbf{i}}_* + (\zeta - Z)\cos\theta_n \bar{\mathbf{j}}_* - \eta_n \bar{\mathbf{k}}_*]}{(\eta_n^2 + (\zeta - Z)^2)\sqrt{\tau^2 - 2T_n\tau + T_n^2 + (\zeta - Z)^2 + \eta_n^2}} d\zeta \right] \Bigg|_{-t_n}^{+t_n} \quad (\text{A32})$$

Integrating with respect to  $\zeta$  (the second local, tangential coordinate along the vortex sheet surface) results in

$$\begin{aligned}
& \int_{-h/2}^{h/2} \int_{-t_n}^{+t_n} \frac{(\zeta - Z) \sin \theta_n \bar{\mathbf{i}}_* + (\zeta - Z) \cos \theta_n \bar{\mathbf{j}}_* - \eta_n \bar{\mathbf{k}}_*}{\sqrt{(\eta_n^2 + (\tau - T_n)^2 + (\zeta - Z)^2)^3}} d\tau d\zeta = \\
& \frac{1}{2} \ln \left[ \frac{\sqrt{\eta_n^2 + (\tau - T_n)^2 + (\zeta - Z)^2} - (\tau - T_n)}{\sqrt{\eta_n^2 + (\tau - T_n)^2 + (\zeta - Z)^2} + (\tau - T_n)} \right] \sin \theta_n \bar{\mathbf{i}}_* \Bigg|_{-h/2}^{h/2} \Bigg|_{-t_n}^{+t_n} \\
& + \frac{1}{2} \ln \left[ \frac{\sqrt{\eta_n^2 + (\tau - T_n)^2 + (\zeta - Z)^2} - (\tau - T_n)}{\sqrt{\eta_n^2 + (\tau - T_n)^2 + (\zeta - Z)^2} + (\tau - T_n)} \right] \cos \theta_n \bar{\mathbf{j}}_* \Bigg|_{-h/2}^{h/2} \Bigg|_{-t_n}^{+t_n} \\
& - \tan^{-1} \left[ \frac{(\tau - T_n)(\zeta - Z)}{\eta_n \sqrt{\eta_n^2 + (\tau - T_n)^2 + (\zeta - Z)^2}} \right] \bar{\mathbf{k}}_* \Bigg|_{-h/2}^{h/2} \Bigg|_{-t_n}^{+t_n}
\end{aligned} \tag{A33}$$

The above terms in Eq. A33 are well-known analytical solutions for rectangular vortex sheets with uniform vorticity (Ref. 7).

Application of integration limits (upper limits of  $\alpha_2, \beta_2$  and lower limits of  $\alpha_1, \beta_1$ ), for an arbitrary function, can be concisely written in the form

$$f(\alpha, \beta) \Big|_{\alpha_1}^{\alpha_2} \Big|_{\beta_1}^{\beta_2} = 4 \sum_{k=1}^2 \sum_{j=1}^2 \left( k - \frac{3}{2} \right) \left( j - \frac{3}{2} \right) f(\alpha_j, \beta_k) \tag{A34}$$

Using this approach (Eq. A34) for handling the integration limits for Eq. A33, the solution now becomes

$$\begin{aligned}
& \int_{-h/2}^{h/2} \int_{-t_n}^{+t_n} \frac{(\zeta - Z) \sin \theta_n \bar{\mathbf{i}}_* + (\zeta - Z) \cos \theta_n \bar{\mathbf{j}}_* - \eta_n \bar{\mathbf{k}}_*}{\sqrt{(\eta_n^2 + (\tau - T_n)^2 + (\zeta - Z)^2)^3}} d\tau d\zeta = \\
& 2 \sum_{k=1}^2 \sum_{j=1}^2 \left(k - \frac{3}{2}\right) \left(j - \frac{3}{2}\right) \ln \left[ \frac{\sqrt{\eta_n^2 + (\tau_{n,k} - T_n)^2 + (\zeta_j - Z)^2} - (\tau_{n,k} - T_n)}{\sqrt{\eta_n^2 + (\tau_{n,k} - T_n)^2 + (\zeta_j - Z)^2} + (\tau_{n,k} - T_n)} \right] \sin \theta_n \bar{\mathbf{i}}_* \\
& + 2 \sum_{k=1}^2 \sum_{j=1}^2 \left(k - \frac{3}{2}\right) \left(j - \frac{3}{2}\right) \ln \left[ \frac{\sqrt{\eta_n^2 + (\tau_{n,k} - T_n)^2 + (\zeta_j - Z)^2} - (\tau_{n,k} - T_n)}{\sqrt{\eta_n^2 + (\tau_{n,k} - T_n)^2 + (\zeta_j - Z)^2} + (\tau_{n,k} - T_n)} \right] \cos \theta_n \bar{\mathbf{j}}_* \\
& - 4 \sum_{k=1}^2 \sum_{j=1}^2 \left(k - \frac{3}{2}\right) \left(j - \frac{3}{2}\right) \tan^{-1} \left[ \frac{(\tau_{n,k} - T_n)(\zeta_j - Z)}{\eta_n \sqrt{\eta_n^2 + (\tau_{n,k} - T_n)^2 + (\zeta_j - Z)^2}} \right] \bar{\mathbf{k}}_*
\end{aligned}
\tag{A35a}$$

where the integration limits  $(\tau_{n,k}, \zeta_j)$  are defined by the matrices

$$\begin{aligned}
\boldsymbol{\tau} &= \begin{bmatrix} -\frac{1}{2}R & \frac{1}{2}R \\ -\frac{1}{2}c & \frac{1}{2}c \\ -\frac{1}{2}R & \frac{1}{2}R \\ -\frac{1}{2}R & \frac{1}{2}R \\ -\frac{1}{2}c & \frac{1}{2}c \\ -\frac{1}{2}R & \frac{1}{2}R \\ -\frac{c}{2} \cos \Lambda & \frac{c}{2} \cos \Lambda \\ -\frac{c}{2} \cos \Lambda & \frac{c}{2} \cos \Lambda \end{bmatrix} & \boldsymbol{\zeta} &= \begin{bmatrix} -\frac{1}{2}h \\ \frac{1}{2}h \end{bmatrix}
\end{aligned}
\tag{A35b-c}$$

Note that  $\tau_{n,1} = -t_n$  and  $\tau_{n,2} = t_n$  (see Eq. A30b). Therefore

$$\begin{aligned}
I_{W13} &= 2 \sum_{n=1}^3 \sum_{k=1}^2 \sum_{j=1}^2 \left( k - \frac{3}{2} \right) \left( j - \frac{3}{2} \right) \ln \left[ \frac{\sqrt{\eta_n^2 + (\tau_{n,k} - T_n)^2 + (\zeta_j - Z)^2} - (\tau_{n,k} - T_n)}{\sqrt{\eta_n^2 + (\tau_{n,k} - T_n)^2 + (\zeta_j - Z)^2} + (\tau_{n,k} - T_n)} \right] \sin \theta_n \\
I_{W23} &= 2 \sum_{n=4}^6 \sum_{k=1}^2 \sum_{j=1}^2 \left( k - \frac{3}{2} \right) \left( j - \frac{3}{2} \right) \ln \left[ \frac{\sqrt{\eta_n^2 + (\tau_{n,k} - T_n)^2 + (\zeta_j - Z)^2} - (\tau_{n,k} - T_n)}{\sqrt{\eta_n^2 + (\tau_{n,k} - T_n)^2 + (\zeta_j - Z)^2} + (\tau_{n,k} - T_n)} \right] \sin \theta_n \\
J_{W13} &= 2 \sum_{n=1}^3 \sum_{k=1}^2 \sum_{j=1}^2 \left( k - \frac{3}{2} \right) \left( j - \frac{3}{2} \right) \ln \left[ \frac{\sqrt{\eta_n^2 + (\tau_{n,k} - T_n)^2 + (\zeta_j - Z)^2} - (\tau_{n,k} - T_n)}{\sqrt{\eta_n^2 + (\tau_{n,k} - T_n)^2 + (\zeta_j - Z)^2} + (\tau_{n,k} - T_n)} \right] \cos \theta_n \\
J_{W23} &= 2 \sum_{n=4}^6 \sum_{k=1}^2 \sum_{j=1}^2 \left( k - \frac{3}{2} \right) \left( j - \frac{3}{2} \right) \ln \left[ \frac{\sqrt{\eta_n^2 + (\tau_{n,k} - T_n)^2 + (\zeta_j - Z)^2} - (\tau_{n,k} - T_n)}{\sqrt{\eta_n^2 + (\tau_{n,k} - T_n)^2 + (\zeta_j - Z)^2} + (\tau_{n,k} - T_n)} \right] \cos \theta_n \\
K_{W13} &= -4 \sum_{n=1}^3 \sum_{k=1}^2 \sum_{j=1}^2 \left( k - \frac{3}{2} \right) \left( j - \frac{3}{2} \right) \tan^{-1} \left[ \frac{(\tau_{n,k} - T_n)(\zeta_j - Z)}{\eta_n \sqrt{\eta_n^2 + (\tau_{n,k} - T_n)^2 + (\zeta_j - Z)^2}} \right] \\
K_{W23} &= -4 \sum_{n=4}^6 \sum_{k=1}^2 \sum_{j=1}^2 \left( k - \frac{3}{2} \right) \left( j - \frac{3}{2} \right) \tan^{-1} \left[ \frac{(\tau_{n,k} - T_n)(\zeta_j - Z)}{\eta_n \sqrt{\eta_n^2 + (\tau_{n,k} - T_n)^2 + (\zeta_j - Z)^2}} \right]
\end{aligned}$$

(A36a-f)

This completes the derivation of the approximate, potential-flow solution for the induced velocities due to rotor/wing interactions. Overall, this also completes the description of the tiltrotor aircraft hover flowfield -- with the exception of the influence of the rotor-on-rotor and wing-on-rotor interactions on rotor thrust and mean inflow. The influence of the rotor-on-rotor and the wing-on-rotor interactions on rotor thrust and mean inflow will be discussed next.

### Effect of Interactions on Rotor Thrust/Inflow

To complete the analytical treatment of rotor/wing interactions in hover, it is first necessary to define an rotor thrust/mean-inflow interaction parameter,  $F$ , for tiltrotors in hover.



$$\bar{\lambda} \equiv \sqrt{C_T F} \quad (A37)$$

If there were no rotor/wing interactions then classic momentum theory (where  $\bar{\lambda} = \sqrt{C_T/2}$ ) would require that  $F=1/2$ . Given the above definition, it is now possible to derive an expression for the mean rotor inflow in terms of the induced velocity terms derived earlier in this paper. The mean rotor inflow, accounting for rotor/wing interactions, is given by

$$\bar{\lambda} = \frac{1}{\pi \Omega R^3} \int_0^{2\pi} \int_0^R (\bar{v} \cdot \bar{k}_*) r dr d\psi \quad (A38)$$

Noting that for isolated rotors in hover, momentum and vortex theory give the result  $\gamma = (\Omega R) \sqrt{2C_T}$  (Ref. 7); however, for rotors influenced by rotor/wing interactions  $\gamma = (\Omega R) \sqrt{C_T/F}$ . When these revised definitions of mean inflow and rotor slipstream circulation --and Eq. A3c -- are substituted into Eq. A38, the following expression can be derived

$$F = \frac{\bar{\lambda}^2}{C_T} = F_{RR} + \frac{-1}{4(\pi R)^2} \int_0^{2\pi} \int_0^R [K_{R1} - 2(K_{W11} + K_{W12} + K_{W13}) + K_{R2} - 2(K_{W21} + K_{W22} + K_{W23})] r dr d\psi \quad (A39)$$

Note that in Eq. A39 a parameter,  $F_{RR}$ , has been included in the expression for the interaction parameter,  $F$ .  $F_{RR}$  is an added term that embodies the rotor-on-rotor effects on rotor thrust and mean inflow. Derivation of  $F_{RR}$  will be discussed in detail later in the paper. The implications of Eqs. A38 and A39 are best understood by noting their impact on estimates of rotor thrust and induced-power. The expression for the rotor thrust (including rotor/wing interactions) ratio with respect to the isolated rotor thrust is

$$\frac{C_T}{C_{T_i}} \approx \sqrt{\frac{1}{2F}} \quad (A40)$$

If the convex rotor/wing image vortex surfaces are replaced with flat, rectangular vortex sheets, then a concise expression for the mean influence of the wing on the rotor can be presented (given Eqs. A39, A36e-f, A27a-b, A26a-b, A15 and A8) as

$$F = \frac{1}{2} + F_{RR} + F_{RW} \quad (\text{A41a})$$

Such that

$$F = \frac{1}{2} + F_{RR} - \frac{2}{(\pi R)^2} \sum_{n=1}^8 \sum_{k=1}^2 \sum_{j=1}^2 \left(k - \frac{3}{2}\right) \left(j - \frac{3}{2}\right) \int_0^{2\pi} \int_0^R r \tan^{-1} \left[ \frac{(\tau_{n,k} - T_n) \left(\zeta_j - \frac{3}{2}h\right)}{\eta_n \sqrt{\eta_n^2 + (\tau_{n,k} - T_n)^2 + \left(\zeta_j - \frac{3}{2}h\right)^2}} \right] dr d\psi \quad (\text{A41b})$$

Or

$$F_{RW} = - \frac{2}{(\pi R)^2} \sum_{n=1}^8 \sum_{k=1}^2 \sum_{j=1}^2 \left(k - \frac{3}{2}\right) \left(j - \frac{3}{2}\right) \int_0^{2\pi} \int_0^R r \tan^{-1} \left[ \frac{(\tau_{n,k} - T_n) \left(\zeta_j - \frac{3}{2}h\right)}{\eta_n \sqrt{\eta_n^2 + (\tau_{n,k} - T_n)^2 + \left(\zeta_j - \frac{3}{2}h\right)^2}} \right] dr d\psi \quad (\text{A41c})$$

Note the introduction of the parameter,  $F_{RW}$ , in Eq. A41a that embodies the wing-on-rotor interactional influence on rotor thrust and mean inflow.

## Rotor-on-Rotor Interaction

Previous authors (e.g. Refs. 12 and 13) have shown that there is an apparent net rotor thrust loss due to rotor/image-plane interactions for image-planes within  $1.24R$  radial distance from the rotor centerline. It is the hypothesis of this paper that the rotor-on-rotor, or rotor/image-plane, interaction,  $F_{RR}$ , is due to the mutual flow entrainment of each rotor's upstream far-wake by the other rotor. Classic actuator disk vortex theory can not explain the observed rotor-on-rotor or rotor/image-plane interactions. However, it will be shown that a combination of vortex and momentum theory can explain and predict the net rotor thrust loss resulting from the rotor-on-rotor (or image-plane-on-rotor) interaction.

As previously derived (Eqs. A3 and A7), the vertical induced velocity from the one of the rotors is given by the expression

$$w(z) = -\frac{\gamma}{4} \left[ \frac{z}{\sqrt{R^2 + z^2}} - 1 \right] \left[ 1 + \frac{R-r}{|R-r|} \right] = \frac{\gamma}{2} \left[ 1 - \frac{z}{\sqrt{R^2 + z^2}} \right] \quad (\text{for } r < R) \quad (\text{A42})$$

Note that in the above equation that  $w(z) \equiv \bar{v} \cdot \bar{k}_*$ . Equation A42, derived from classic actuator disk vortex theory, does not automatically satisfy mass flow continuity. By imposing the continuity constraint, an approximate rotor wake slipstream boundary, as a function of  $z$ , can be defined (Eq. A43).

$$R(z) \approx \frac{R}{\sqrt{\left(1 - \frac{z}{\sqrt{R^2 + z^2}}\right)}} \quad (\text{A43})$$

The implication of this approximate wake contraction expression is that the two rotor wakes overlap each other quite quickly above the rotor disk plane. The consequence of this wake overlap is mutual flow entrainment between the two rotors in the upstream far wake. Therefore, given superposition of the rotor induced velocity distributions, the result is a nonuniformity of the wake velocity distribution and a shifting of the centroid of the wakes laterally outward from each other. A wake skew angle,  $\chi$ , consequently exists for both rotor wakes, upstream of the rotor disk plane. Refer to Fig. A10.

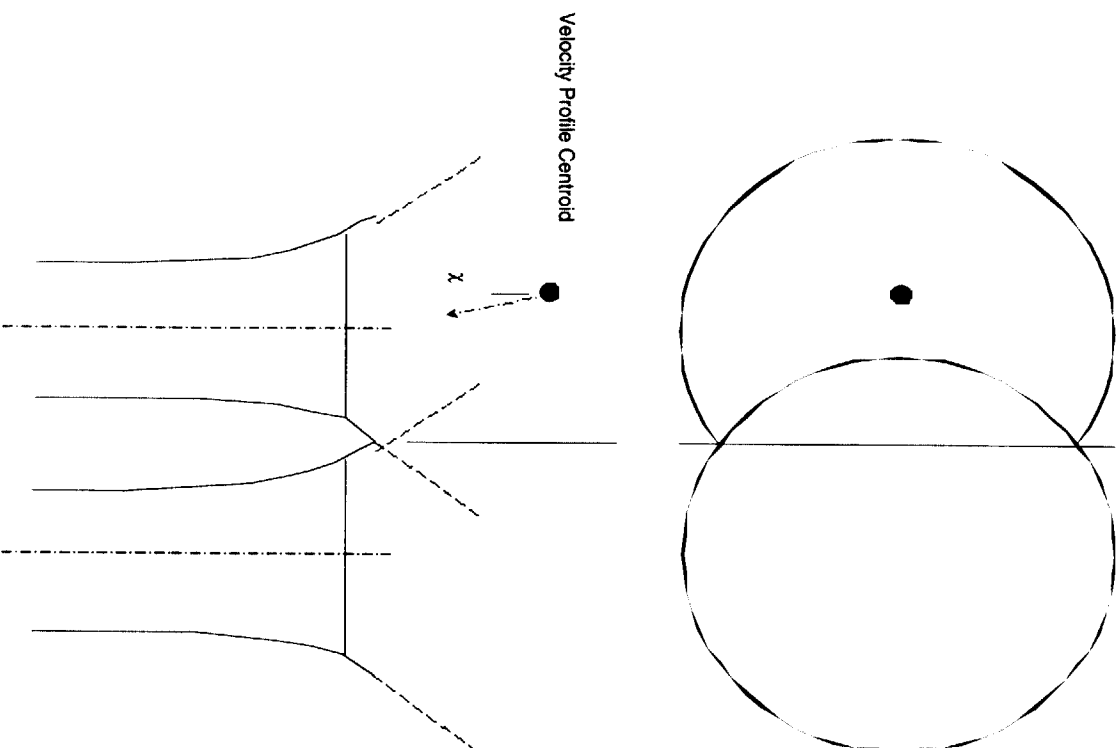


Fig. A10 - Rotor-on-Rotor Interaction (Upstream Far-Wake Flow Entrainment)

In the upstream far-wake, the centroid of the wake velocity distribution can be approximated by

$$\begin{aligned}
 X_{wake} &= \frac{2}{3\pi} \left[ b \left( \frac{\pi}{2} + \frac{2}{\pi} \right) - \frac{b^2}{2R(z)} - 2R(z) \right] \\
 &\approx \frac{2}{3\pi} \left[ b \left( \frac{\pi}{2} + \frac{2}{\pi} \right) - 2R(z) \right]
 \end{aligned}
 \tag{A44}$$

Equation A44 is derived from standard textbook formulas (see Refs. 14 and 15) for a composite cross-sectional area that consists of a circle with a missing segment. This assumes uniform flow in the far-wake, even though the slipstream is no longer wholly circular in cross-section.

An upstream far-wake skew angle has been observed in flow visualization studies cited in the literature for side-by-side and tandem rotors (Ref. 16). Unfortunately, this flow visualization work did not yield quantitative measures of the skew angle. The discussion in the literature is quite mixed with regard to quantifying rotor-on-rotor interactions for rotors in close side-by-side proximity (but not overlapped). This is principally due to an inability in these past studies to isolate rotor-on-rotor from test-stand-on-rotor effects.

A wake skew angle expression can be derived from the definition of the centroid of the far-wake for a single rotor. The skew angle of the far wake with respect to the rotor axes is

$$\chi = \tan^{-1} \left( -\frac{\partial x_{\text{wake}}}{\partial z} \right) \approx -\frac{\partial x_{\text{wake}}}{\partial z} \quad (\text{A45})$$

which yields

$$\chi = \frac{2}{3\pi} \left[ 2 - \frac{1}{2} \left( \frac{b}{R(z)} \right)^2 \right] \frac{\partial R(z)}{\partial z} \approx \frac{4}{3\pi} \frac{\partial R(z)}{\partial z} \quad (\text{A46})$$

Now, from Eq. A46, approximately

$$\frac{\partial R(z)}{\partial z} \rightarrow \sqrt{2} \text{ as } z \rightarrow +\infty \quad (\text{A47})$$

Application of momentum theory (see Ref. 7 and 17), when accounting for the upstream far-wake skew angle, gives the following expressions for rotor thrust with and without rotor-on-rotor interactional aerodynamic influences.

$$T_{RR} = \rho w(z) \cos \chi \Big|_{z \rightarrow -\infty} \quad (\text{A48a})$$

whereas

$$T_I = \mathbf{m} \mathbf{w}(z) \Big|_{z \rightarrow -\infty} \quad (\text{A48b})$$

Therefore, the ratio of rotor thrust, including rotor-on-rotor interactional effects, with respect to isolated rotor thrust approaches a minima value.

$$\frac{C_{T_{RR}}}{C_{T_I}} \rightarrow \cos\left(\frac{\sqrt{32}}{3\pi}\right) \quad (\text{A49})$$

and, therefore,

$$F_{RR} \rightarrow \frac{1}{2} \left[ \frac{1}{\cos^2\left(\frac{\sqrt{32}}{3\pi}\right)} - 1 \right] \quad (\text{A50})$$

Note that Eqs. A49 and A50, together, represent the maximum net rotor thrust loss possible for rotor-on-rotor (or rotor/image-plane) interactions.

The thrust minima result of Eq. A49 will now be used to arrive at an expression for the functional dependence of the rotor-on-rotor interaction on the lateral displacement of the two side-by-side rotors with respect to each other. It is assumed that the maximum rotor-on-rotor interaction (the thrust minima of Eq. A49) occurs when  $b = 2R$  and an asymptotic upper bound on the wake skew angle is approached, i.e., when

$$\chi \rightarrow \frac{\sqrt{32}}{3\pi} \quad \text{when} \quad b \rightarrow 2R$$

Imposing the above constraint on the Eqs. A44, A46, and A48a-b yields an expression that includes rotor proximity effects (Eq. A51).

$$\frac{C_{T_{RR}}}{C_{T_i}} \approx \cos \left[ \frac{\sqrt{32}}{3\pi} \left( 2 - \left( \frac{b}{2R} \right)^2 \right) \right] \quad (A51)$$

and, correspondingly,

$$F_{RR} \approx \frac{1}{2} \left[ \frac{1}{\cos^2 \left[ \frac{\sqrt{32}}{3\pi} \left( 2 - \left( \frac{b}{2R} \right)^2 \right) \right]} - 1 \right] \quad (A52)$$

Equations A51 and A52 are valid for the range  $1 \leq b/2R \leq \sqrt{2}$ . The classic work of Stepniewski (see Ref. 7) should be referred to for thrust loss estimates for overlapped rotors,  $b/2R < 1$ .

### **Wing-on-Rotor Interactions**

The rotor-on-rotor interaction term,  $F_{RR}$ , was derived in the previous section. This section will derive the solution for the wing-on-rotor interaction parameter,  $F_{RW}$ .

$$F_{RW} = -\frac{2}{(\pi R)^2} \sum_{n=1}^8 \sum_{k=1}^2 \sum_{j=1}^2 \left( k - \frac{3}{2} \right) \left( j - \frac{3}{2} \right) \int_0^{2\pi} \int_0^R r \tan^{-1} \left[ \frac{(\tau_{n,k} - T_n) \left( \zeta_j - \frac{3}{2} h \right)}{\eta_n \sqrt{\eta_n^2 + (\tau_{n,k} - T_n)^2 + \left( \zeta_j - \frac{3}{2} h \right)^2}} \right] dr d\psi \quad (A53)$$

$T_n$  and  $\eta_n$  are functions of  $r$  and  $\psi$  -- see Eqs. A28a-c. The solution for  $F_{RW}$  will be used - in conjunction with Eq. A52 for  $F_{RR}$  -- to solve Eqs. A38 and A40 for the mean inflow and the rotor thrust as influenced by both rotor-on-rotor and wing-on-rotor interactions.

Equation A53 can be considerably simplified by integrating with respect to the individual vortex sheet local coordinates, instead of the global coordinates, and integrating over a rectangular region that overlaps the circular region representing the rotor disk. (Refer to Fig. A12.)

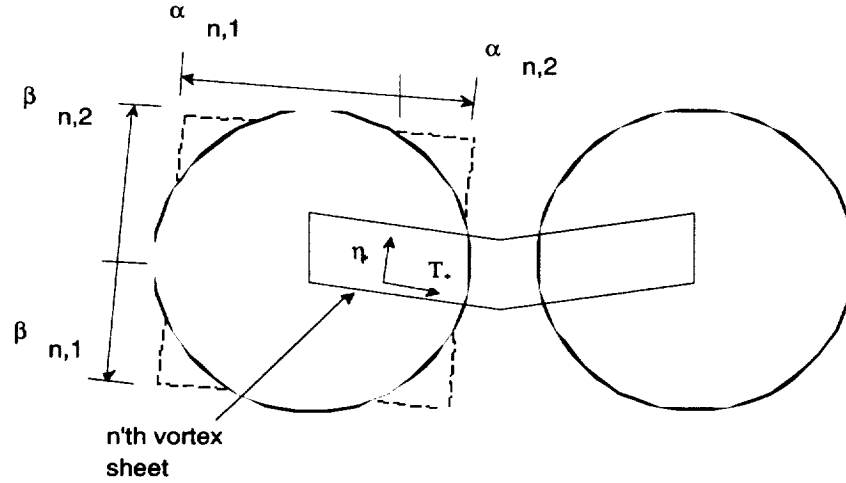


Fig. A12 - Approximate Integration Approach for Mean Inflow from the Rotor/Wing Vortex Sheets

From a first-order analysis perspective, this approximation yields reasonable results. (Improved  $F_{RW}$  estimates, though, could be obtained through numerical integration of Eq. A53.)

Integrating with respect to the individual vortex sheet local coordinates, instead of the global coordinates, gives Eq. A54a-f.

$$F_{RW} \approx -\frac{2}{(\pi R)^2} \sum_{n=1}^8 \sum_{k=1}^2 \sum_{j=1}^2 \left(k - \frac{3}{2}\right) \left(j - \frac{3}{2}\right) \int_{\beta_{n,1}}^{\beta_{n,2}} \int_{\alpha_{n,1}}^{\alpha_{n,2}} \tan^{-1} \left[ \frac{(\tau_{n,k} - T_*) \left(\zeta_j - \frac{3}{2}h\right)}{\eta_* \sqrt{\eta_*^2 + (\tau_{n,k} - T_*)^2 + \left(\zeta_j - \frac{3}{2}h\right)^2}} \right] dT_* d\eta_* \quad (A54a)$$



where the limits are

$$\begin{aligned}
\alpha_{n,2} &= \frac{\sqrt{\pi}}{2} R - (x_n \cos \theta_n + y_n \sin \theta_n) \\
\alpha_{n,1} &= -\frac{\sqrt{\pi}}{2} R - (x_n \cos \theta_n + y_n \sin \theta_n) \\
\beta_{n,2} &= \frac{\sqrt{\pi}}{2} R - (y_n \cos \theta_n - x_n \sin \theta_n) \\
\beta_{n,1} &= -\frac{\sqrt{\pi}}{2} R - (y_n \cos \theta_n - x_n \sin \theta_n)
\end{aligned} \tag{A54b-f}$$

The above limits (Eqs. A54b-f) are defined on the basis of an equivalent rectangular area that matches the rotor disk area. Refer to Eqs. A30a-d for the earlier established definitions of  $\theta_n$ ,  $x_n$ , and  $y_n$ . Two new integration independent variables have been introduced into Eq. A54a -- in place of the global independent variables,  $r$  and  $\psi$  (and their functions  $T_n$  and  $\eta_n$ ) of Eq. A53.

A final simplification to the problem is possible if an approximation to the arctangent function is employed, whereby

$$\tan^{-1} u \approx \frac{u}{\sqrt{1+u^2}}$$

This allows Eq. A54a to be expressed as

$$\begin{aligned}
F_{RW} \approx & \\
& \mp \frac{2}{(\pi R)^2} \sum_{n=1}^8 \sum_{k=1}^2 \sum_{j=1}^2 \left( k - \frac{3}{2} \right) \left( j - \frac{3}{2} \right) \int_{\beta_{n,1}}^{\beta_{n,2}} \int_{\alpha_{n,1}}^{\alpha_{n,2}} \frac{\left( \zeta_j - \frac{3}{2} h \right)}{\sqrt{\eta_*^2 + \left( \zeta_j - \frac{3}{2} h \right)^2}} \cdot \frac{(\tau_{n,k} - T_*)}{\sqrt{\eta_*^2 + (\tau_{n,k} - T_*)^2}} dT_* d\eta_*
\end{aligned} \tag{A55}$$

Integration with respect to  $T_*$  for Eq. A55 gives

$$F_{RW} \approx$$

$$+ \frac{2}{(\pi R)^2} \sum_{n=1}^8 \sum_{k=1}^2 \sum_{j=1}^2 \left(k - \frac{3}{2}\right) \left(j - \frac{3}{2}\right) \int_{\beta_{n,1}}^{\beta_{n,2}} \left(\zeta_j - \frac{3}{2}h\right) \text{sgn}(\eta_*) \sqrt{\frac{\eta_*^2 + (\tau_{n,k} - T_*)^2}{\eta_*^2 + \left(\zeta_j - \frac{3}{2}h\right)^2}} d\eta_* \Bigg|_{\alpha_{n,1}}^{\alpha_{n,2}}$$

(A56)

where  $\text{sgn}(\eta_*) \equiv \frac{\eta_*}{|\eta_*|}$ .

Reference 9 provides solutions for definite integrals of the above form. These solutions are in terms of elliptic integrals of the first and second kind,  $F(\phi, k)$  and  $E(\phi, k)$ . The general form of the solution is

$$\int_0^u \sqrt{\frac{x^2 + a^2}{x^2 + b^2}} dx = a \{F(\alpha, q) - E(\alpha, q)\} + u \sqrt{\frac{u^2 + a^2}{u^2 + b^2}} \quad (A57a)$$

for  $a > b$  and  $u > 0$ ,

$$\int_0^u \sqrt{\frac{x^2 + a^2}{x^2 + b^2}} dx = \frac{a^2}{b} F(\epsilon, Q) - b E(\epsilon, Q) + u \sqrt{\frac{u^2 + b^2}{u^2 + a^2}} \quad (A57b)$$

for  $b > a$  and  $u > 0$ ,

where

$$\alpha = \tan^{-1}\left(\frac{u}{b}\right) \quad q = \frac{\sqrt{a^2 - b^2}}{a}$$

$$\varepsilon = \tan^{-1}\left(\frac{u}{a}\right) \quad \text{and} \quad Q = \frac{\sqrt{b^2 - a^2}}{b} \quad (\text{A57c-f})$$

Therefore, the solution for Eq. A56 is

$$F_{RW} \approx + \frac{8}{(\pi R)^2} \sum_{n=1}^8 \sum_{m=1}^2 \sum_{l=1}^2 \sum_{k=1}^2 \sum_{j=1}^2 \left(m - \frac{3}{2}\right) \left(1 - \frac{3}{2}\right) \left(k - \frac{3}{2}\right) \left(j - \frac{3}{2}\right) F_{\text{Sheet}} \quad (\text{A58a})$$

where

$$F_{\text{Sheet}} = \left(\zeta_j - \frac{3}{2}h\right) \left\{ |\tau_{n,k} - \alpha_{n,l}| \cdot \left[ \chi_*^{(1-\gamma_*)/2} F(\varphi, \kappa) - \chi_*^{(\gamma_*-1)/2} E(\varphi, \kappa) \right] + |\beta_{n,m}| \cdot \left[ \frac{\beta_{n,m}^2 + (\tau_{n,k} - \alpha_{n,l})^2}{\beta_{n,m}^2 + \left(\zeta_j - \frac{3}{2}h\right)^2} \right]^{\gamma_*/2} \right\} \quad (\text{A58b})$$

and

$$\gamma_* = \frac{|\tau_{n,k} - \alpha_{n,l}| - \left|\zeta_j - \frac{3}{2}h\right|}{\left|\tau_{n,k} - \alpha_{n,l}\right| - \left|\zeta_j - \frac{3}{2}h\right|} \quad \chi_* = \frac{|\tau_{n,k} - \alpha_{n,l}|}{\left|\zeta_j - \frac{3}{2}h\right|}$$

$$\varphi = \tan^{-1} \left[ \frac{|\beta_{n,m}|}{\sqrt{(\tau_{n,k} - \alpha_{n,l})^{1-\gamma_*} \left( \zeta_j - \frac{3}{2}h \right)^{1+\gamma_*}}} \right]$$

$$\kappa = \sqrt{\frac{\left| (\tau_{n,k} - \alpha_{n,l})^2 - \left( \zeta_j - \frac{3}{2}h \right)^2 \right|}{(\tau_{n,k} - \alpha_{n,l})^{1+\gamma_*} \left( \zeta_j - \frac{3}{2}h \right)^{1-\gamma_*}}} \quad (\text{A58c-f})$$

Accurate values for the Legendre elliptic integrals in Eqs. A58a-f are required for accurate estimates of wing-on-rotor interactions. Bulirsch's generalized elliptical integral algorithm, Ref. 10, was used for the predictions of the effect of rotor/wing interaction on rotor thrust and mean inflow in this paper.

The predicted mean inflow contribution of the rotor-on-rotor and wing-on-rotor interactions provides considerable insight into the rotor performance of a tiltrotor aircraft. Tiltrotor hover ground and fountain effects, as observed in experimental investigations of rotor/wing interactions, are embodied by two different sets of analytical terms that contribute to the rotor mean inflow. The ground effect induced by the wing is due to the mean inflow contributions from the image vortex sheets for the primary rotor/wing interaction (the portion of  $F_{\text{Sheet}}$  due to vortex sheets 1-3 and 7 by this paper's numbering convention). The fountain effect on the other hand, is due to two factors: the upstream far wake effect,  $F_{\text{RR}}$ , and the influence of the secondary set of image vortices (the portion of  $F_{\text{Sheet}}$  due to vortex sheet elements 4-6 and 8).

## Appendix B - Strength of Wing Image Vortex Sheets

### **A Heuristic Argument**

The method of images analogy employed in this paper requires that the convex image vortex surfaces -- those used to model the wing interaction with the rotor wake -- have a net circulation of  $-\gamma$  (i.e., these image vortex surfaces are 'reflecting back' the actuator disk's trailed vorticity in the portion of the vortex cylinder directly above the partial ground plane/wing). This is depicted in Fig. B1.

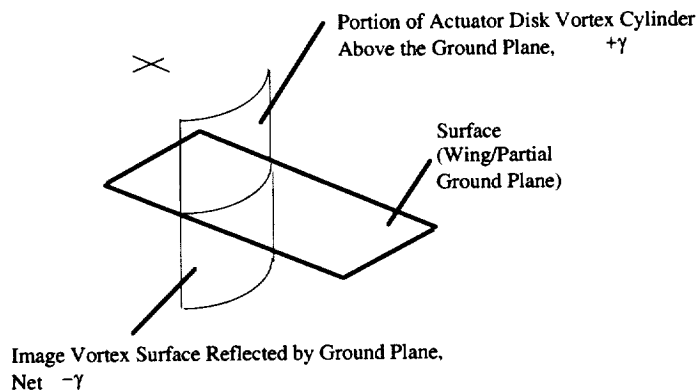


Fig. B1 - Consequence of 'Method of Images' Analogy As Applied to Rotor/Partial Ground Plane Interactions

To achieve this net circulation of  $-\gamma$ , a vortex sheet of strength  $-2\gamma$  needs to be superimposed over the portion of the circumference of the actuator disk vortex cylinder directly below the wing/partial ground plane. Refer to Fig. B2.

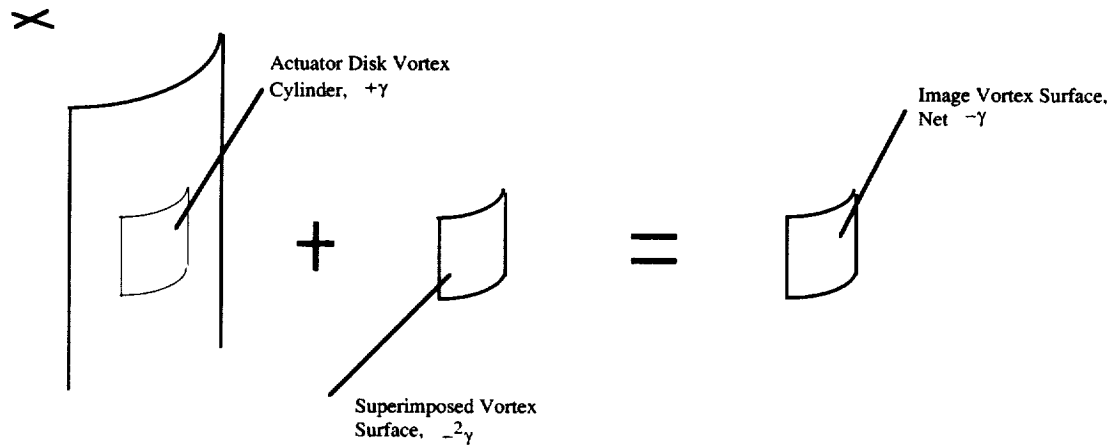


Fig. B2 - Required Potential Flow Superposition

Kelvin's Theorem for inviscid flow (Ref. 18) – “The circulation about any closed path moving with the fluid is a constant” -- requires that the superimposed vortex sheet have a set of companion vortex sheets to form a closed vortex sheath. There are two vortex sheaths for the tiltrotor rotor/wing interaction problem. Each vortex sheath is comprised of a set of four image vortex surfaces representing a partial ground plane, or wing span, embedded in each rotor wake. Refer to Fig. B3. Again, by Kelvin's Theorem, the circulation of each individual image vortex sheet in the vortex sheath has to have the uniform strength  $-2\gamma$ . No theorem or method *a priori* dictates that the spatial orientation of the three image vortex sheets in the interior of each rotor wake conform to the planform layout of the wing (or partial ground plane) surface; and, yet, this would appear to be a plausible assumption.

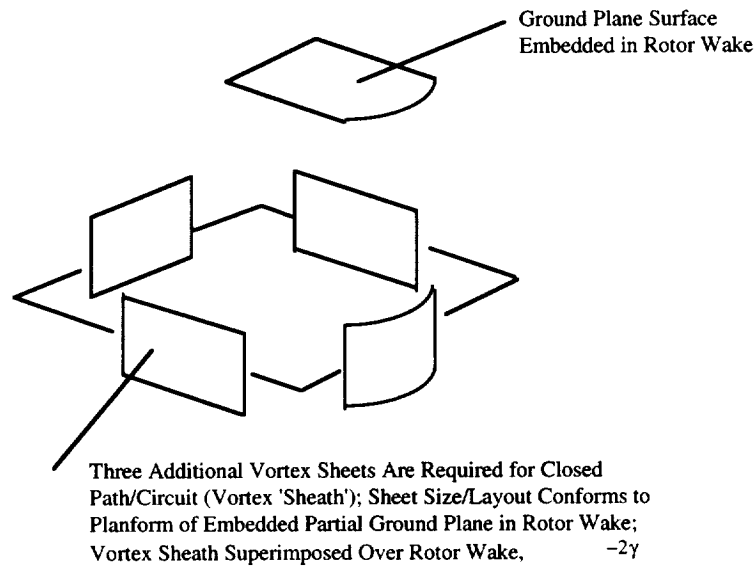


Fig. B3 - Consequence of Kelvin's Theorem: A Closed Path/Circuit of Vortex Surfaces (A Vortex Sheath)

This completes the outline of a heuristic argument for defining the circulation strength of the wing image vortex sheets such that the no-flow constraint of the wing/ground plane surface is adhered to.

### A Numerical Assessment

Previously,  $\gamma_{\text{sheet}}$  was heuristically argued to be equal in magnitude to  $-2\gamma$ . A more definitive treatment will now be offered. It should be noted, though, that this flow model and associated numerical assessment implicitly assumes that the wing is of moderate-to-high aspect ratio such that  $b > 2s$  and  $s \gg c$ .

Assume that the wing image vortex sheet circulation strength is unknown. And, yet, the wing surface no-flow boundary constraint must be met, which in turn dictates the circulation strength.

This problem can be stated analytically by Eq. B1 and more specifically Eqs. B2a-d. Refer to Fig. B4.

$$\bar{\lambda}_{\text{wing surface}} = 0 \quad (\text{B1})$$

Now

$$\begin{aligned} \bar{\lambda}_{\text{wing surface}} = & \frac{1}{\Omega R} \left\{ \frac{-\gamma}{4(\pi R)^2} \int_0^{2\pi} \int_0^R (K_{R1} + K_{R2}) r dr d\psi \right\} \bigg|_{z=-h} \\ & + \frac{-\gamma_{\text{sheet}}}{4\pi c \sqrt{R^2 - c^2/4}} \int_{\beta_{n,1}^*}^{\beta_{n,2}^*} \int_{\alpha_{n,1}^*}^{\alpha_{n,2}^*} [K_{W11} + K_{W12} + K_{W13} + K_{W21} + K_{W22} + K_{W23}] dT_* d\eta_* \bigg|_{z=-h} \end{aligned} \quad (\text{B2a})$$

$$\alpha^* = \begin{bmatrix} -s/2 & +s/2 \\ -c/2 & +c/2 \\ -s/2 & +s/2 \\ -s/2 & +s/2 \\ -c/2 & +c/2 \\ -s/2 & +s/2 \\ -c/2 & +c/2 \\ -c/2 & +c/2 \end{bmatrix} \quad \beta^* = \begin{bmatrix} -c \cos \Lambda & 0 \\ -s & 0 \\ -c \cos \Lambda & 0 \\ 0 & 0 \\ -b & s-b \\ 0 & 0 \\ -s & 0 \\ b-2s & b-s \end{bmatrix} \quad (\text{B2b-c})$$

where

$$s = \sqrt{R^2 - \frac{c^2}{4} \cos^2 \Lambda} \quad (\text{B2d})$$

Figure B4 schematically outlines the integration to be performed in Eq. B2a. It should be noted that the local coordinate system will be used for the integration of the induced velocity contribution for each image vortex sheet across the wing surface.



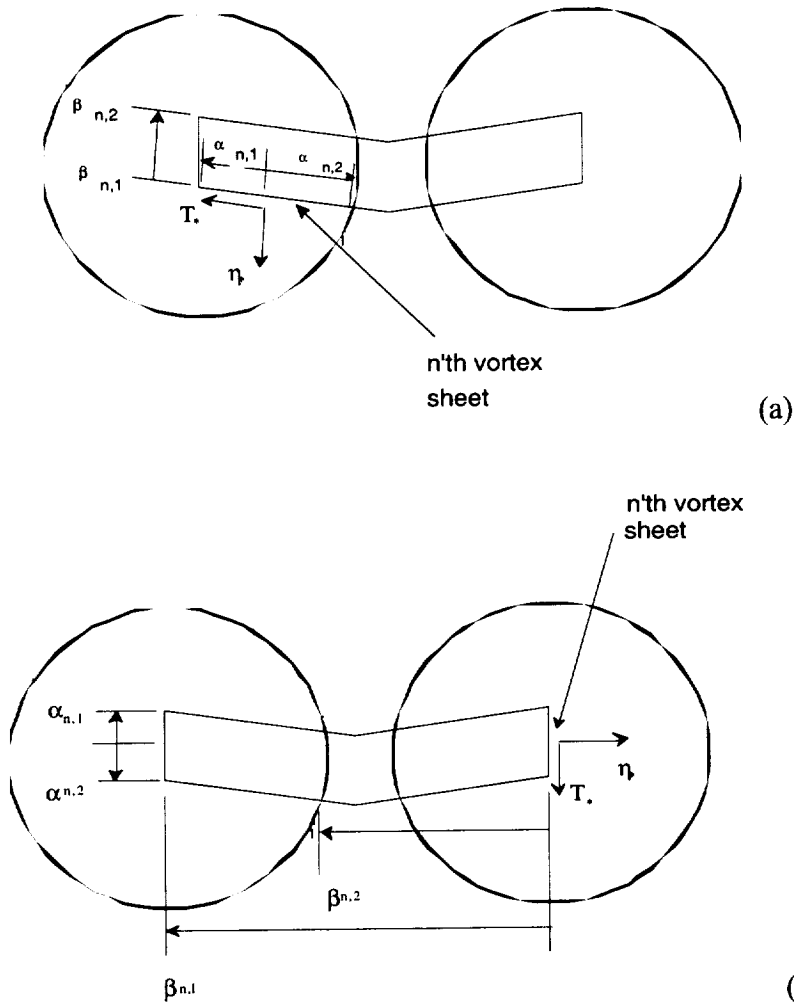


Fig. B4a-b - Integration Limits for the Wing Circulation Strength Analysis: (a) Definition of Limits for First (LHS) Rotor and (b) Limits for Second (RHS) Rotor

Equation B2 has several analogous attributes with respect to Eq. A38. In both cases a mean inflow estimate is made for a defined area of interest. In the case of the Eq. A38 the mean inflow for the port (left-hand-side) rotor disk at the disk plane was estimated; Eq. B2 attempts to define the mean inflow (which needs to be zero) at the left-hand-side wing surface (for that portion embedded in the rotor wake). The integration limits ( $\alpha_{n,2}^*$ ,  $\alpha_{n,1}^*$ ,  $\beta_{n,2}^*$ , and  $\beta_{n,1}^*$ ) for the second double integral term of Eq. B2a are given approximately in Eqs. B2b-d; approximately, in the sense that they are accurate only for small angles of wing sweep,  $\Lambda$ . The planform area of the portion of the wing embedded in an individual rotor wake is (for a tiltrotor aircraft where the rotor nacelles are mounted at the wing tips):  $\text{Area} = c \cos \Lambda \sqrt{R^2 - (c \cos \Lambda / 2)^2} \approx c \sqrt{R^2 - c^2 / 4}$ . This wing area estimate can be straightforwardly derived from elementary geometry and trigonometry considerations.

Substituting Eq. B2a into B1 gives

$$\frac{\gamma_{\text{sheet}}}{\gamma} = -\frac{c\sqrt{R^2 - c^2/4}}{\pi R^2} \cdot \frac{\int_0^{2\pi} \int_0^R (K_{R1} + K_{R2}) r dr d\psi}{\int_{\beta_{n,1}^*}^{\beta_{n,2}^*} \int_{\alpha_{n,1}^*}^{\alpha_{n,2}^*} [K_{W11} + K_{W12} + K_{W13} + K_{W21} + K_{W22} + K_{W23}] dT \cdot d\eta_*} \Big|_{z=-h} \quad (\text{B3})$$

It will be shown that

$$\frac{\gamma_{\text{sheet}}}{\gamma} \approx -2 \quad (\text{B4})$$

Given Eq. A8 (and the derived expressions for the terms  $K_{R1}$  and  $K_{R2}$ ), the numerator of Eq. B3 can be found to be

$$\begin{aligned} \int_0^{2\pi} \int_0^R (K_{R1} + K_{R2}) r dr d\psi \Big|_{z=-h} &= \int_0^{2\pi} \int_0^R \left\{ \frac{z}{\sqrt{R^2 + z^2}} - 1 \right\} \left[ 1 + \frac{R-r}{|R-r|} \right] r dr d\psi \Big|_{z=-h} \\ &= -2(\pi R)^2 \left\{ \frac{h}{\sqrt{R^2 + h^2}} + 1 \right\} \end{aligned} \quad (\text{B5})$$

Given Eqs. A36e-f and A54a (all wing image vortex surfaces represented solely by flat rectangular sheets instead of a combination of convex surfaces and flat rectangular sheets), the denominator of Eq. B3 is seen to be

$$\begin{aligned}
& \int_{\beta_{n,1}^*}^{\beta_{n,2}^*} \int_{\alpha_{n,1}^*}^{\alpha_{n,2}^*} [K_{W11} + K_{W12} + K_{W13} + K_{W21} + K_{W22} + K_{W23}] dT_* d\eta_* \Big|_{z=-h} \approx \\
& +4 \sum_{n=1}^8 \sum_{k=1}^2 \sum_{j=1}^2 \left(k - \frac{3}{2}\right) \left(j - \frac{3}{2}\right) \int_{\beta_{n,1}^*}^{\beta_{n,2}^*} \int_{\alpha_{n,1}^*}^{\alpha_{n,2}^*} \tan^{-1} \left[ \frac{(\tau_{n,k} - T_*)(\zeta_j - Z)}{\eta_* \sqrt{\eta_*^2 + (\tau_{n,k} - T_*)^2 + (\zeta_j - Z)^2}} \right] dT_* d\eta_* \Big|_{z=-h} = \\
& +4 \sum_{n=1}^8 \sum_{k=1}^2 \sum_{j=1}^2 \left(k - \frac{3}{2}\right) \left(j - \frac{3}{2}\right) \int_{\beta_{n,1}^*}^{\beta_{n,2}^*} \int_{\alpha_{n,1}^*}^{\alpha_{n,2}^*} \tan^{-1} \left[ \frac{(\tau_{n,k} - T_*)(\zeta_j - h/2)}{\eta_* \sqrt{\eta_*^2 + (\tau_{n,k} - T_*)^2 + (\zeta_j - h/2)^2}} \right] dT_* d\eta_*
\end{aligned}
\tag{B6}$$

where now  $Z = z + 3h/2$  (from Eq. A28a). Note the sign change of Eq. B6 with respect to Eq. A54a. This sign change accounts for the different local vortex sheet coordinate systems used between the two analyses.

Validation of the hypothesis of Eq. B4 can be accomplished via numerical integration of Eq. B6 and the incorporation of the results into Eq. B3, given Eq. B5. The resulting numerical validation of Eq. B4 can be seen in Figs. B5 and B6.

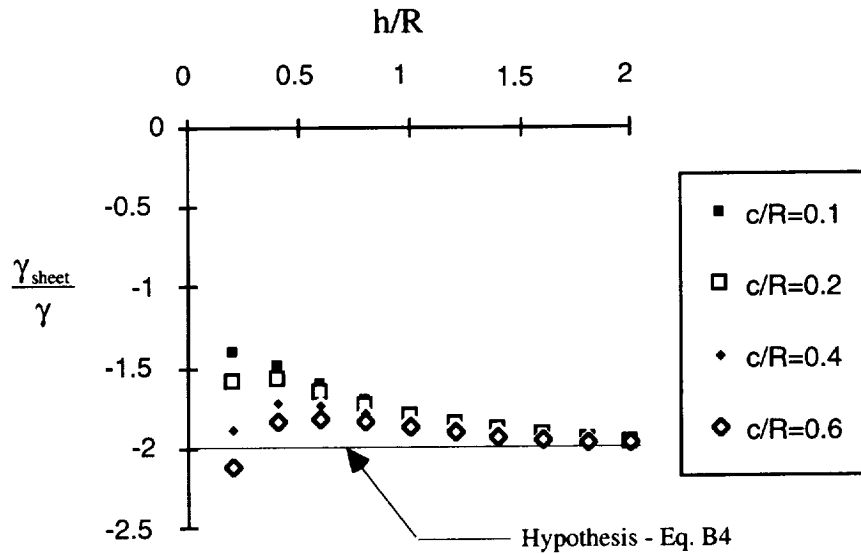


Fig. B5 - Numerical Validation of Equation B4 -- Primary Wing/Partial Ground Plane Interaction Only

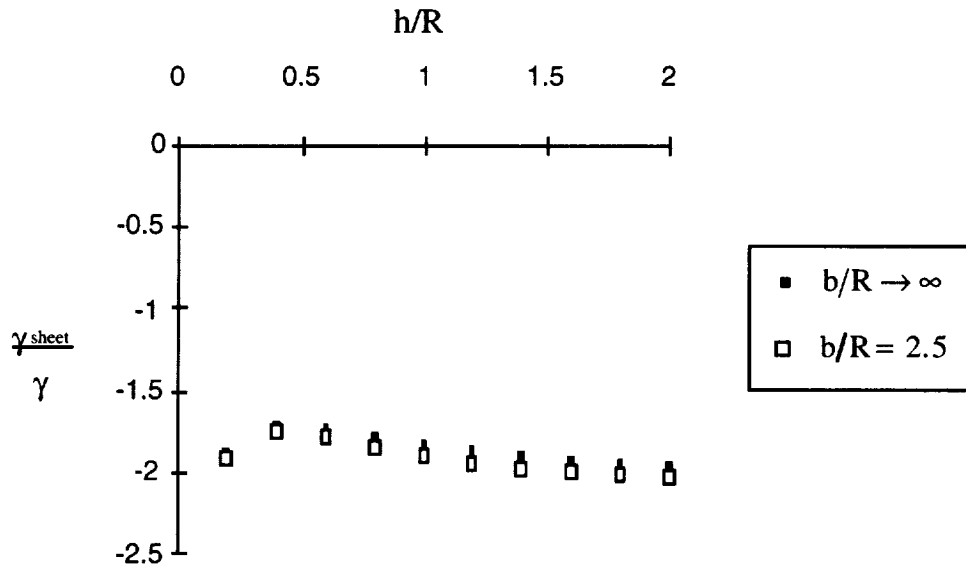


Fig. B6 - Numerical Validation of Equation B4 -- Includes the Effect of Both the Primary and Secondary Wing/Partial Ground Plane Interaction ( $c/R=0.4$ )

As can be seen in Figs. B5 and B6, the hypothesis ( $\gamma_{sheet}/\gamma = -2$ ) is reasonably sound except perhaps when the wing/partial ground plane is very close to the rotor tip-path-plane (i.e., very small  $h/R$  values). The secondary wing/partial ground plane interaction has a small, but discernable, effect on the wing image vortex surface circulation strength.

### An Approximate Analytic Treatment

An approximate analytical solution will now be outlined for Eq. B6, which will be used to further validate the hypothesis of Eq. B4. This approximate analytic treatment -- just as the above summarized numerical assessment -- remains based on a flow model that implicitly assumes that the wing is of moderate-to-high aspect ratio such that  $b > 2s$  and  $s \gg c$ .

Applying the arctangent approximation ( $\tan^{-1} u \approx u/\sqrt{1+u^2}$ ), Eq. B6 can be approximated by

$$\begin{aligned}
& \int_{\beta_{n,1}^*}^{\beta_{n,2}^*} \int_{\alpha_{n,1}^*}^{\alpha_{n,2}^*} [K_{W11} + K_{W12} + K_{W13} + K_{W21} + K_{W22} + K_{W23}] dT_* d\eta_* \approx \\
& \pm 4 \sum_{n=1}^8 \sum_{k=1}^2 \sum_{j=1}^2 \left(k - \frac{3}{2}\right) \left(j - \frac{3}{2}\right) \int_{\beta_{n,1}^*}^{\beta_{n,2}^*} \int_{\alpha_{n,1}^*}^{\alpha_{n,2}^*} \frac{(\zeta_j - h/2)}{\sqrt{\eta_*^2 + (\zeta_j - h/2)^2}} \cdot \frac{(\tau_{n,k} - T_*)}{\sqrt{\eta_*^2 + (\tau_{n,k} - T_*)^2}} dT_* d\eta_*
\end{aligned}
\tag{B7}$$

Again, analogously following the integration steps of Eqs. A55 through A58, Eq. B7 becomes

$$\begin{aligned}
& \int_{\beta_{n,1}^*}^{\beta_{n,2}^*} \int_{\alpha_{n,1}^*}^{\alpha_{n,2}^*} [K_{W11} + K_{W12} + K_{W13} + K_{W21} + K_{W22} + K_{W23}] dT_* d\eta_* \approx \\
& -16 \sum_{n=1}^8 \sum_{m=1}^2 \sum_{l=1}^2 \sum_{k=1}^2 \sum_{j=1}^2 \left(m - \frac{3}{2}\right) \left(1 - \frac{3}{2}\right) \left(k - \frac{3}{2}\right) \left(j - \frac{3}{2}\right) F_*,
\end{aligned}
\tag{B8a}$$

where

$$\begin{aligned}
F_* = (\zeta_j - h/2) & \left\{ |\tau_{n,k} - \alpha_{n,l}^*| \cdot \left[ \chi_{**}^{(1-\gamma_{**})/2} F(\varphi_*, \kappa_*) - \chi_{**}^{(\gamma_{**}-1)/2} E(\varphi_*, \kappa_*) \right] \right. \\
& \left. + |\beta_{n,m}^*| \cdot \left[ \frac{(\beta_{n,m}^*)^2 + (\tau_{n,k} - \alpha_{n,l}^*)^2}{(\beta_{n,m}^*)^2 + (\zeta_j - h/2)^2} \right]^{\gamma_{**}/2} \right\}
\end{aligned}
\tag{B8b}$$

and

$$\gamma_{**} = \frac{|\tau_{n,k} - \alpha_{n,l}^*| - |\zeta_j - h/2|}{\|\tau_{n,k} - \alpha_{n,l}^*| - |\zeta_j - h/2|\|} \quad \chi_{**} = \frac{|\tau_{n,k} - \alpha_{n,l}^*|}{|\zeta_j - h/2|}$$

$$\varphi_* = \tan^{-1} \left[ \frac{|\beta_{n,m}^*|}{\sqrt{(\tau_{n,k} - \alpha_{n,l}^*)^{1-\gamma_{**}} (\zeta_j - h/2)^{1+\gamma_{**}}}} \right]$$

$$\kappa_* = \sqrt{\frac{(\tau_{n,k} - \alpha_{n,l}^*)^2 - (\zeta_j - h/2)^2}{(\tau_{n,k} - \alpha_{n,l}^*)^{1+\gamma_{**}} (\zeta_j - h/2)^{1-\gamma_{**}}}} \quad (\text{B8c-f})$$

In order to validate the conjecture of Eq. B4, it is necessary to simplify Eq. B8a-f. First, noting the definition of the integration limit vector  $\zeta_j$  (Eq. A35c), Eq. B8a can be simplified to

$$\int_{\beta_{n,l}^*}^{\beta_{n,2}^*} \int_{\alpha_{n,l}^*}^{\alpha_{n,2}^*} [K_{w11} + K_{w12} + K_{w13} + K_{w21} + K_{w22} + K_{w23}] dT_* d\eta_* \approx$$

$$+ 8 \sum_{n=1}^8 \sum_{m=1}^2 \sum_{l=1}^2 \sum_{k=1}^2 \left( m - \frac{3}{2} \right) \left( 1 - \frac{3}{2} \right) \left( k - \frac{3}{2} \right) F_*$$

(B9a)

where

$$F_* = -h \left\{ |\tau_{n,k} - \alpha_{n,l}^*| \cdot \left[ \chi_{**}^{(1-\gamma_{**})/2} F(\varphi_*, \kappa_*) - \chi_{**}^{(\gamma_{**}-1)/2} E(\varphi_*, \kappa_*) \right] \right.$$

$$\left. + |\beta_{n,m}^*| \cdot \left[ \frac{(\beta_{n,m}^*)^2 + (\tau_{n,k} - \alpha_{n,l}^*)^2}{(\beta_{n,m}^*)^2 + h^2} \right]^{\gamma_{**}/2} \right\} \quad (\text{B9b})$$

and

$$\gamma_{**} = \frac{|\tau_{n,k} - \alpha_{n,l}^*| - h}{||\tau_{n,k} - \alpha_{n,l}^*| - h|} \quad \chi_{**} = |\tau_{n,k} - \alpha_{n,l}^*|/h$$

$$\varphi_* = \tan^{-1} \left[ \frac{|\beta_{n,m}^*|}{\sqrt{(-h)^{1+\gamma_{**}} (\tau_{n,k} - \alpha_{n,l}^*)^{1-\gamma_{**}}}} \right]$$

$$\kappa_* = \sqrt{\frac{|\left(\tau_{n,k} - \alpha_{n,l}^*\right)^2 - h^2|}{(-h)^{1-\gamma_{**}} (\tau_{n,k} - \alpha_{n,l}^*)^{1+\gamma_{**}}}} \quad (\text{B9c-f})$$

Note for small wing sweep angles, i.e.  $\Lambda \approx 0$ , the following relationship holds approximately true (see Eqs. A35b, A30b, B2b, and B2d).

$$|\tau_{n,k} - \alpha_{n,l}^*| \approx 2|k-l|t_n \quad (\text{B10})$$

Applying Eq. B10 to B9b-f gives

$$F_* = -h \left\{ 2|k-l|t_n \cdot \left[ \chi_{**}^{(1-\gamma_{**})/2} F(\varphi_*, \kappa_*) - \chi_{**}^{(\gamma_{**}-1)/2} E(\varphi_*, \kappa_*) \right] \right. \\ \left. + |\beta_{n,m}^*| \cdot \left[ \frac{(\beta_{n,m}^*)^2 + 4(k-l)^2 t_n^2}{(\beta_{n,m}^*)^2 + h^2} \right]^{\gamma_{**}/2} \right\} \quad (\text{B11a})$$

where

$$\gamma_{**} = \frac{2|k-l|t_n - h}{|2|k-l|t_n - h|} \quad \chi_{**} = 2|k-l|t_n/h$$

$$\varphi_* = \tan^{-1} \left[ \frac{|\beta_{n,m}^*|}{\sqrt{(-h)^{1+\gamma_{**}} (2|k-l|t_n)^{1-\gamma_{**}}}} \right]$$

$$\kappa_* = \sqrt{\frac{|4(k-l)^2 t_n^2 - h^2|}{(-h)^{1-\gamma_{**}} (2|k-l|t_n)^{1+\gamma_{**}}}} \quad (\text{B11b-e})$$

The parameters  $\gamma_*$ ,  $\varphi_*$ , and  $\kappa_*$  can be cast in terms of  $\chi_{**}$  such that

$$\gamma_{**} = \frac{\chi_{**} - 1}{|\chi_{**} - 1|} = \text{sgn}(\chi_{**} - 1) \quad (\text{B12a})$$

$$\varphi_* = \tan^{-1} \left[ \frac{|\beta_{n,m}^*|}{h} \chi_{**}^{(\gamma_{**}-1)/2} \right] \quad (\text{B12b})$$

$$\kappa_* = \sqrt{\frac{|\chi_{**}^2 - 1|}{\chi_{**}^{1+\gamma_{**}}}} \quad (\text{B12c})$$

Note that Eqs. B12a-c can be evaluated for two conditions

If  $\chi_{**} < 1$

$$\gamma_{**} = -1 \quad (\text{B13a})$$

$$\chi_{**}^{(1-\gamma_{**})/2} = \chi_{**} \quad (\text{B13b})$$

$$\chi_{**}^{(\gamma_{**}-1)/2} = \frac{1}{\chi_{**}} \quad (\text{B13c})$$



$$\chi_{**}^{1+\gamma_{**}} = 1 \quad (\text{B13d})$$

$$\kappa_* = \sqrt{1 - \chi_{**}^2} \quad (\text{B13e})$$

$$\varphi_* = \tan^{-1} \left[ \frac{|\beta_{n,m}^*|}{h} \cdot \left( \frac{1}{\chi_{**}} \right) \right] \quad (\text{B13f})$$

Or, if  $\chi_{**} \geq 1$

$$\gamma_{**} = +1 \quad (\text{B13g})$$

$$\chi_{**}^{(1-\gamma_{**})/2} = 1 \quad (\text{B13h})$$

$$\chi_{**}^{(\gamma_{**}-1)/2} = 1 \quad (\text{B13i})$$

$$\chi_{**}^{1+\gamma_{**}} = \chi_{**}^2 \quad (\text{B13j})$$

$$\kappa_* = \sqrt{1 - \frac{1}{\chi_{**}^2}} \quad (\text{B13k})$$

$$\varphi_* = \tan^{-1} \left[ \frac{|\beta_{n,m}^*|}{h} \right] \quad (\text{B13l})$$

Application of Eqs. B13a-l into Eq. B11a gives

$$\begin{aligned}
F_* = & -h^2 u(1 - \chi_{**}) \left\{ \chi_{**}^2 F \left( \tan^{-1} \left[ \frac{|\beta_{n,m}^*|}{h} \cdot \left( \frac{1}{\chi_{**}} \right) \right], \sqrt{1 - \chi_{**}^2} \right) - E \left( \tan^{-1} \left[ \frac{|\beta_{n,m}^*|}{h} \cdot \left( \frac{1}{\chi_{**}} \right) \right], \sqrt{1 - \chi_{**}^2} \right) \right. \\
& \left. + \frac{|\beta_{n,m}^*|}{h} \cdot \left[ \frac{(\beta_{n,m}^*/h)^2 + 1}{(\beta_{n,m}^*/h)^2 + \chi_{**}^2} \right]^{1/2} \right\} \\
& -h^2 u(\chi_{**} - 1) \left\{ \chi_{**} \cdot \left[ F \left( \tan^{-1} \left[ \frac{|\beta_{n,m}^*|}{h} \right], \sqrt{1 - \frac{1}{\chi_{**}^2}} \right) - E \left( \tan^{-1} \left[ \frac{|\beta_{n,m}^*|}{h} \right], \sqrt{1 - \frac{1}{\chi_{**}^2}} \right) \right] \right. \\
& \left. + \frac{|\beta_{n,m}^*|}{h} \cdot \left[ \frac{(\beta_{n,m}^*/h)^2 + \chi_{**}^2}{(\beta_{n,m}^*/h)^2 + 1} \right]^{1/2} \right\}
\end{aligned} \tag{B14}$$

where  $u(x-x_0)$  is the unit step function.

An approximate relationship between  $\beta_{n,m}^*$  and  $\chi_{**}$  can be defined by means of Eq. B15a-c (again, if  $\Lambda \approx 0$ ). This can be readily validated by comprehensively comparing the results of Eq. B15a-c to Eq. B2c, given Eq. B11c.

$$\beta_{n,m}^* \approx \frac{A}{\chi_{**}} + B$$

where

$$\begin{aligned}
A = & (1 - \delta_{n4} - \delta_{n6}) \text{sgn}(7 - n) \{ (m - 2)u(4 - n) + (\text{sgn}(7 - n)m + 4u(n - 7) - 1)u(n - 4) \} \left[ |k - l| \frac{cs}{h} \right] \\
B = & (1 - \delta_{n4} - \delta_{n6} - \delta_{n7}) \text{sgn}(n - 7)u(n - 4)b
\end{aligned} \tag{B15a-c}$$

The function  $\delta_{ij}$  is the 'Kronecker delta' function:  $\delta_{ij}=0$  when  $i \neq j$  and  $\delta_{ij}=1$  when  $i=j$ . (For example,  $\delta_{n4}=1$  if, and only when,  $n=4$ , else wise  $\delta_{n4}=0$ .) The function  $\text{sgn}(x-x_0)$  is the 'sign' function:  $\text{sgn}(x-x_0)=-1$  if  $x < x_0$  and  $\text{sgn}(x-x_0)=+1$  if  $x \geq x_0$ . (The sign function can

alternatively be expressed in terms of unit step functions, if preferred.) Equation B15a-c can be reduced to a considerably simpler form ( $\beta_{n,m}^* = A'/\chi_{**}$ , where  $A' = |k-l|(m-2)cs/h$ ) if only a single rotor and one partial ground plane were accounted for in Eq. B14. Further, the distribution/ordering of elements within the  $\beta_{n,m}^*$  matrix could also be re-ordered and optimized to reduce the complexity of the expressions for B15a-c. That stated, proceeding with the application of Eqs. B15a-c to B14 gives

$$\begin{aligned}
 F_* = & -h^2 u(1 - \chi_{**}) \left\{ \chi_{**}^2 F \left( \tan^{-1} \left[ \left| \frac{A}{\chi_{**}} + B \right| \cdot \left( \frac{1}{h\chi_{**}} \right) \right], \sqrt{1 - \chi_{**}^2} \right) - E \left( \tan^{-1} \left[ \left| \frac{A}{\chi_{**}} + B \right| \cdot \left( \frac{1}{h\chi_{**}} \right) \right], \sqrt{1 - \chi_{**}^2} \right) \right. \\
 & \left. + \frac{1}{h} \left| \frac{A}{\chi_{**}} + B \right| \cdot \left[ \frac{(A + B\chi_{**})^2 + h^2 \chi_{**}^2}{(A + B\chi_{**})^2 + h^2 \chi_{**}^4} \right]^{1/2} \right\} \\
 & -h^2 u(\chi_{**} - 1) \left\{ \chi_{**} \cdot \left[ F \left( \tan^{-1} \left[ \frac{1}{h} \cdot \left| \frac{A}{\chi_{**}} + B \right| \right], \sqrt{1 - \frac{1}{\chi_{**}^2}} \right) - E \left( \tan^{-1} \left[ \frac{1}{h} \cdot \left| \frac{A}{\chi_{**}} + B \right| \right], \sqrt{1 - \frac{1}{\chi_{**}^2}} \right) \right] \right. \\
 & \left. + \frac{1}{h} \left| \frac{A}{\chi_{**}} + B \right| \cdot \left[ \frac{(A + B\chi_{**})^2 + h^2 \chi_{**}^4}{(A + B\chi_{**})^2 + h^2 \chi_{**}^2} \right]^{1/2} \right\}
 \end{aligned}
 \tag{B16}$$

Introducing an intermediate parameter,  $G_*$  (referring to Eq. B9).

$$G_* = \sum_{l=1}^2 \sum_{k=1}^2 \left( 1 - \frac{3}{2} \right) \left( k - \frac{3}{2} \right) F_* \tag{B17}$$

Substituting Eq. B16 into B17 and performing the required summation operations, while noting that when  $|k-l|=0$  then  $\chi_{**} = A = 0$  (but the ratio  $A/\chi_{**}$  is not necessarily equal to zero), gives

$$\begin{aligned}
G_* = & +\frac{1}{2}h^2 - \frac{1}{2}h \left| \frac{A_*}{\chi_{**}} + B \right| \cdot \left[ 1 + \left( \frac{h}{A_*/\chi_{**} + B} \right)^2 \right]^{1/2} \\
& + \frac{1}{2}h \left| \frac{A_*}{\chi_{**}} + B \right| \cdot \left\{ u(1 - \chi_{**}) \left[ \frac{(A_* + B\chi_{**})^2 + h^2\chi_{**}^2}{(A_* + B\chi_{**})^2 + h^2\chi_{**}^4} \right]^{1/2} + u(\chi_{**} - 1) \left[ \frac{(A_* + B\chi_{**})^2 + h^2\chi_{**}^4}{(A_* + B\chi_{**})^2 + h^2\chi_{**}^2} \right]^{1/2} \right\} \\
& + \frac{1}{2}h^2 u(1 - \chi_{**}) \left\{ \chi_{**}^2 F \left( \tan^{-1} \left[ \left| \frac{A_*}{\chi_{**}} + B \right| \cdot \left( \frac{1}{h\chi_{**}} \right) \right], \sqrt{1 - \chi_{**}^2} \right) - E \left( \tan^{-1} \left[ \left| \frac{A_*}{\chi_{**}} + B \right| \cdot \left( \frac{1}{h\chi_{**}} \right) \right], \sqrt{1 - \chi_{**}^2} \right) \right\} \\
& + \frac{1}{2}h^2 u(\chi_{**} - 1) \chi_{**} \cdot \left\{ F \left( \tan^{-1} \left[ \frac{1}{h} \cdot \left| \frac{A_*}{\chi_{**}} + B \right| \right], \sqrt{1 - \frac{1}{\chi_{**}^2}} \right) - E \left( \tan^{-1} \left[ \frac{1}{h} \cdot \left| \frac{A_*}{\chi_{**}} + B \right| \right], \sqrt{1 - \frac{1}{\chi_{**}^2}} \right) \right\}
\end{aligned}$$

$$\text{when } |A/\chi_{**} + B| \neq 0$$

$$G_* = 0$$

$$\text{when } |A/\chi_{**} + B| = 0$$

(B18a)

where (given Eqs. B11c and B15b and noting that  $|k - l| = 1$ )

$$A_* = (1 - \delta_{n4} - \delta_{n6}) \text{sgn}(7 - n) \{ (m - 2)u(4 - n) + (\text{sgn}(7 - n)m + 4u(n - 7) - 1)u(n - 4) \} \left[ \frac{cs}{h} \right]$$

$$\chi_{**} = 2t_n/h$$

(B18b-c)

Now, given Eq. B18a-c, Eq. B9a can be recast as

$$\int_{\beta_{n,1}^*}^{\beta_{n,2}^*} \int_{\alpha_{n,1}^*}^{\alpha_{n,2}^*} [K_{w11} + K_{w12} + K_{w13} + K_{w21} + K_{w22} + K_{w23}] dT_* d\eta_* \approx +8 \sum_{n=1}^8 \sum_{m=1}^2 \left( m - \frac{3}{2} \right) G_*$$

(B19)

An exhaustive examination of the matrix of  $\chi_{**}$ ,  $A_*$ , and  $B$  values resulting from all the possible permutations of the  $m$  and  $n$  indices, reveals that there are five distinct, nonzero terms implicit in Eq. B19.

$$\int_{\beta_{n,1}^*}^{\beta_{n,2}^*} \int_{\alpha_{n,1}^*}^{\alpha_{n,2}^*} [K_{w11} + K_{w12} + K_{w13} + K_{w21} + K_{w22} + K_{w23}] dT_* d\eta_* \approx$$

$$+8\{H_{*1} + H_{*2} + H_{*3} + H_{*4} + H_{*5}\}$$

(B20)

These terms are

$$H_{*1} \approx -h^2 + \frac{1}{2}h[c^2 + h^2]^{1/2} - \frac{1}{2}ch \cdot \left[ \frac{c^2 + s^2}{c^2 + h^2} \right]^{\text{sgn}\left(\frac{s}{h}-1\right)/2}$$

$$- \frac{1}{2}h^2u\left(1 - \frac{s}{h}\right) \left\{ \left(\frac{s}{h}\right)^2 F\left(\tan^{-1}\left(\frac{c}{s}\right), \sqrt{1 - \left(\frac{s}{h}\right)^2}\right) - E\left(\tan^{-1}\left(\frac{c}{s}\right), \sqrt{1 - \left(\frac{s}{h}\right)^2}\right) \right\}$$

$$- \frac{1}{2}u\left(\frac{s}{h} - 1\right)hs \left\{ F\left(\tan^{-1}\left(\frac{c}{h}\right), \sqrt{1 - \left(\frac{h}{s}\right)^2}\right) - E\left(\tan^{-1}\left(\frac{c}{h}\right), \sqrt{1 - \left(\frac{h}{s}\right)^2}\right) \right\}$$

$$H_{*2} \approx +\frac{1}{2}h[s^2 + h^2]^{1/2} - \frac{1}{2}hs \cdot \left[ \frac{s^2 + c^2}{s^2 + h^2} \right]^{\text{sgn}\left(\frac{c}{h}-1\right)/2}$$

$$- \frac{1}{2}h^2u\left(1 - \frac{c}{h}\right) \left\{ \left(\frac{c}{h}\right)^2 F\left(\tan^{-1}\left(\frac{s}{c}\right), \sqrt{1 - \left(\frac{c}{h}\right)^2}\right) - E\left(\tan^{-1}\left(\frac{s}{c}\right), \sqrt{1 - \left(\frac{c}{h}\right)^2}\right) \right\}$$

$$- \frac{1}{2}u\left(\frac{c}{h} - 1\right)hc \left\{ F\left(\tan^{-1}\left(\frac{s}{h}\right), \sqrt{1 - \left(\frac{h}{c}\right)^2}\right) - E\left(\tan^{-1}\left(\frac{s}{h}\right), \sqrt{1 - \left(\frac{h}{c}\right)^2}\right) \right\}$$

$$\begin{aligned}
H_{*3} \approx & +\frac{1}{4}h[b^2+h^2]^{1/2} - \frac{1}{4}hb\left[\frac{b^2+c^2}{b^2+h^2}\right]^{\text{sgn}\left(\frac{c}{h}-1\right)/2} \\
& -\frac{1}{4}h^2u\left(1-\frac{c}{h}\right)\left\{\left(\frac{c}{h}\right)^2F\left(\tan^{-1}\left(\frac{b}{c}\right),\sqrt{1-\left(\frac{c}{h}\right)^2}\right)-E\left(\tan^{-1}\left(\frac{b}{c}\right),\sqrt{1-\left(\frac{c}{h}\right)^2}\right)\right\} \\
& -\frac{1}{4}u\left(\frac{c}{h}-1\right)hc\left\{F\left(\tan^{-1}\left(\frac{b}{h}\right),\sqrt{1-\left(\frac{h}{c}\right)^2}\right)-E\left(\tan^{-1}\left(\frac{b}{h}\right),\sqrt{1-\left(\frac{h}{c}\right)^2}\right)\right\} \\
\\
H_{*4} \approx & +\frac{1}{4}h[(b-2s)^2+h^2]^{1/2} - \frac{1}{4}h|b-2s|\cdot\left[\frac{(b-2s)^2+c^2}{(b-2s)^2+h^2}\right]^{\text{sgn}\left(\frac{c}{h}-1\right)/2} \\
& -\frac{1}{4}h^2u\left(1-\frac{c}{h}\right)\left\{\left(\frac{c}{h}\right)^2F\left(\tan^{-1}\left(\frac{|b-2s|}{c}\right),\sqrt{1-\left(\frac{c}{h}\right)^2}\right)-E\left(\tan^{-1}\left(\frac{|b-2s|}{c}\right),\sqrt{1-\left(\frac{c}{h}\right)^2}\right)\right\} \\
& -\frac{1}{4}u\left(\frac{c}{h}-1\right)hc\left\{F\left(\tan^{-1}\left(\frac{|b-2s|}{h}\right),\sqrt{1-\left(\frac{h}{c}\right)^2}\right)-E\left(\tan^{-1}\left(\frac{|b-2s|}{h}\right),\sqrt{1-\left(\frac{h}{c}\right)^2}\right)\right\} \\
\\
H_{*5} \approx & -\frac{1}{2}h[(b-s)^2+h^2]^{1/2} + \frac{1}{2}h|b-s|\cdot\left[\frac{(b-s)^2+c^2}{(b-s)^2+h^2}\right]^{\text{sgn}\left(\frac{c}{h}-1\right)/2} \\
& +\frac{1}{2}h^2u\left(1-\frac{c}{h}\right)\left\{\left(\frac{c}{h}\right)^2F\left(\tan^{-1}\left(\frac{|b-s|}{c}\right),\sqrt{1-\left(\frac{c}{h}\right)^2}\right)-E\left(\tan^{-1}\left(\frac{|b-s|}{c}\right),\sqrt{1-\left(\frac{c}{h}\right)^2}\right)\right\} \\
& +\frac{1}{2}u\left(\frac{c}{h}-1\right)hc\left\{F\left(\tan^{-1}\left(\frac{|b-s|}{h}\right),\sqrt{1-\left(\frac{h}{c}\right)^2}\right)-E\left(\tan^{-1}\left(\frac{|b-s|}{h}\right),\sqrt{1-\left(\frac{h}{c}\right)^2}\right)\right\}
\end{aligned}$$

(B21a-e)

Terms  $H_{*1}$  and  $H_{*2}$  account for the primary wing/rotor interaction as it influences the no-flow wing surface constraint;  $H_{*3}$  and  $H_{*4}$ , and  $H_{*5}$  account for the secondary wing/rotor interaction.

Note that a general function  $f(x)$  that has the attributes of  $f(0)=f_0$ ,  $f(c)=f_c$ , and  $f(x)|_{x \rightarrow \infty} \rightarrow f_\infty$  can be approximated by a rational function of the form

$$f(x) \approx g(x) = c_0 + \frac{c_1 x}{\sqrt{c_2^2 + x^2}} \quad (\text{B22a})$$

where  $c_0$ ,  $c_1$ , and  $c_2$  are constants that have the values

$$c_0 = f_0$$

$$c_1 = f_\infty - f_0$$

$$c_2 = \left(\frac{c}{R}\right) \sqrt{\left(\frac{f_\infty - f_0}{f_c - f_0}\right)^2 - 1}$$

(B22b-d)

Other rational functions could be chosen for an approximation function, but this one best illustrates the point that  $\gamma_{\text{sheet}}/\gamma \approx -2$  for representative values of  $c/R$ ,  $b/R$ , and  $h/R$ . Reference 19 discusses in more detail the approximation of functions by rational functions.

Returning to Eqs. B20 and B21a-e, if  $b$  and  $c$  are assumed to be finite-valued constants, and  $h/R$  can be treated as an independent variable

$$f(x) = 8\{H_{*1} + H_{*2} + H_{*3} + H_{*4} + H_{*5}\} \approx c_0 + \frac{c_1 x}{\sqrt{c_2^2 + x^2}}$$

where

$$x \equiv h/R$$

$$f_0 = 8\{H_{*1} + H_{*2} + H_{*3} + H_{*4} + H_{*5}\} \Big|_{h/R \rightarrow 0}$$

$$f_c = 8\{H_{*1} + H_{*2} + H_{*3} + H_{*4} + H_{*5}\} \Big|_{h/R \rightarrow c/R}$$

$$f_{\infty} = 8\{H_{*1} + H_{*2} + H_{*3} + H_{*4} + H_{*5}\}\Big|_{h/R \rightarrow \infty}$$

(B23a-e)

And the coefficients  $c_0$ ,  $c_1$ , and  $c_2$  are determined from Eqs. B22b-c.

Note that the elliptical integrals of the first and second kind can be approximated by the following expressions, Eqs. B24a-b. These elliptic integral approximations result from truncation of series expressions found in standard calculus handbooks -- see Ref. 9.

$$E(\phi, k) \approx \frac{2}{\pi} E\left(\frac{\pi}{2}, k\right) \phi$$

$$F(\phi, k) \approx \frac{2}{\pi} F\left(\frac{\pi}{2}, k\right) \phi \approx \left[1 + \frac{2}{\pi} \left(\frac{k^2}{2 - k^2}\right)\right] \phi$$

(B24a-b)

Applying the appropriate  $h/R$  limits to Eqs. B21a-e given the elliptical integral expression approximations, Eqs. B24a-b, yields

$$H_{*1}\Big|_{h/R \rightarrow 0} \rightarrow 0$$

$$H_{*2}\Big|_{h/R \rightarrow 0} \rightarrow 0$$

$$H_{*3}\Big|_{h/R \rightarrow 0} \rightarrow 0$$

$$H_{*4}\Big|_{h/R \rightarrow 0} \rightarrow 0$$

$$H_{*5}\Big|_{h/R \rightarrow 0} \rightarrow 0$$

$$\begin{aligned} H_{*1}\Big|_{h/R \rightarrow c/R} &\rightarrow \left(\frac{1}{\sqrt{2}} - 1\right)c^2 - \left(\frac{\pi}{8} + \frac{1}{2\sqrt{2}}\right)cs \\ &\approx -\frac{3}{4}cs \end{aligned}$$



$$H_{*2}|_{h/R \rightarrow c/R} \rightarrow 0$$

$$H_{*3}|_{h/R \rightarrow c/R} \rightarrow 0$$

$$H_{*4}|_{h/R \rightarrow c/R} \rightarrow 0$$

$$H_{*5}|_{h/R \rightarrow c/R} \rightarrow 0$$

$$\begin{aligned} H_{*1}|_{h/R \rightarrow \infty} &\rightarrow \frac{1}{2}h^2 \left\{ -1 - \frac{c}{\sqrt{c^2 + s^2}} + \frac{2}{\pi} \text{Tan}^{-1}\left(\frac{c}{s}\right) \right\} \Big|_{h/R \rightarrow \infty} - \frac{1}{2} \left(1 + \frac{2}{\pi}\right) s^2 \text{Tan}^{-1}\left(\frac{c}{s}\right) \\ &\approx -\frac{1}{2}h^2 \Big|_{h/R \rightarrow \infty} - \frac{1}{2} \left(1 + \frac{2}{\pi}\right) s^2 \text{Tan}^{-1}\left(\frac{c}{s}\right) \end{aligned}$$

$$\begin{aligned} H_{*2}|_{h/R \rightarrow \infty} &\rightarrow \frac{1}{2}h^2 \left\{ 1 - \frac{s}{\sqrt{c^2 + s^2}} + \frac{2}{\pi} \text{Tan}^{-1}\left(\frac{s}{c}\right) \right\} \Big|_{h/R \rightarrow \infty} - \frac{1}{2} \left(1 + \frac{2}{\pi}\right) c^2 \text{Tan}^{-1}\left(\frac{s}{c}\right) \\ &\approx +\frac{1}{2}h^2 \Big|_{h/R \rightarrow \infty} - \frac{1}{2} \left(1 + \frac{2}{\pi}\right) c^2 \text{Tan}^{-1}\left(\frac{s}{c}\right) \end{aligned}$$

$$\begin{aligned} H_{*3}|_{h/R \rightarrow \infty} &\rightarrow \frac{1}{4}h^2 \left\{ 1 - \frac{b}{\sqrt{c^2 + b^2}} + \frac{2}{\pi} \text{Tan}^{-1}\left(\frac{b}{c}\right) \right\} \Big|_{h/R \rightarrow \infty} - \frac{1}{4} \left(1 + \frac{2}{\pi}\right) c^2 \text{Tan}^{-1}\left(\frac{b}{c}\right) \\ &\approx +\frac{1}{4}h^2 \Big|_{h/R \rightarrow \infty} - \frac{1}{4} \left(1 + \frac{2}{\pi}\right) c^2 \text{Tan}^{-1}\left(\frac{b}{c}\right) \end{aligned}$$

$$\begin{aligned} H_{*4}|_{h/R \rightarrow \infty} &\rightarrow \frac{1}{4}h^2 \left\{ 1 - \frac{|b - 2s|}{\sqrt{c^2 + (b - 2s)^2}} + \frac{2}{\pi} \text{Tan}^{-1}\left(\frac{|b - 2s|}{c}\right) \right\} \Big|_{h/R \rightarrow \infty} - \frac{1}{4} \left(1 + \frac{2}{\pi}\right) c^2 \text{Tan}^{-1}\left(\frac{|b - 2s|}{c}\right) \\ &\approx +\frac{1}{4}h^2 \Big|_{h/R \rightarrow \infty} - \frac{1}{4} \left(1 + \frac{2}{\pi}\right) c^2 \text{Tan}^{-1}\left(\frac{|b - 2s|}{c}\right) \end{aligned}$$

$$\begin{aligned}
H_{*5}|_{h/R \rightarrow \infty} &\rightarrow \frac{1}{2}h^2 \left\{ -1 + \frac{|b-s|}{\sqrt{c^2 + (b-s)^2}} - \frac{2}{\pi} \text{Tan}^{-1}\left(\frac{|b-s|}{c}\right) \right\} \Bigg|_{h/R \rightarrow \infty} + \frac{1}{2}\left(1 + \frac{2}{\pi}\right)c^2 \text{Tan}^{-1}\left(\frac{|b-s|}{c}\right) \\
&\approx -\frac{1}{2}h^2 \Bigg|_{h/R \rightarrow \infty} + \frac{1}{2}\left(1 + \frac{2}{\pi}\right)c^2 \text{Tan}^{-1}\left(\frac{|b-s|}{c}\right)
\end{aligned}$$

(B25a-j)

Which -- noting that  $b > 2s$ , and an implicit assumption that  $b \gg c$ , and applying the arctangent approximation ( $\tan^{-1} u \approx u/\sqrt{1+u^2}$ ) -- gives

$$f_0 = 0$$

$$f_c = -6cs$$

$$f_\infty =$$

$$\begin{aligned}
&-4\left(1 + \frac{2}{\pi}\right) \left\{ s^2 \text{Tan}^{-1}\left(\frac{c}{s}\right) + c^2 \text{Tan}^{-1}\left(\frac{s}{c}\right) + c^2 \left[ \frac{1}{2} \text{Tan}^{-1}\left(\frac{b}{c}\right) + \frac{1}{2} \text{Tan}^{-1}\left(\frac{|b-2s|}{c}\right) - \text{Tan}^{-1}\left(\frac{|b-s|}{c}\right) \right] \right\} \\
&\approx -4\left(1 + \frac{2}{\pi}\right) \left\{ cs + \frac{1}{2}c^2 \left[ \frac{|b-2s|}{\sqrt{(b-2s)^2 + c^2}} - 1 \right] \right\}
\end{aligned}$$

(B26a-c)

Substituting Eq. B26a-c into B22b-d gives

$$c_0 = 0$$

$$c_1 = -4\left(1 + \frac{2}{\pi}\right)(cs + c_3c^2)$$

$$c_2 = \left(\frac{c}{R}\right) \sqrt{\frac{4}{9}\left(1 + \frac{2}{\pi}\right)^2 \left(1 + c_3\frac{c}{s}\right)^2 - 1}$$

$$c_3 \equiv \frac{1}{2} \left[ \frac{|b - 2s|}{\sqrt{(b - 2s)^2 + c^2}} - 1 \right]$$

(B27a-d)

Therefore, after laborious efforts, given Eqs. B3, B5, B20, B23a-d, and B27a-b, the following expression for the image vortex system circulation strength (representing the rotor/wing interaction) can be derived

$$\frac{\gamma_{\text{sheet}}}{\gamma} = \frac{2\pi cs}{c_1} \left[ \sqrt{\frac{c_2^2 + x^2}{1 + x^2}} + \sqrt{1 + \left(\frac{c_2}{x}\right)^2} \right]$$

(B28)

Given the approximate (albeit analytical) nature of Eq. B28, it is appropriate to evaluate the accuracy of its results as compared to the numerical assessment of Eq. B3.

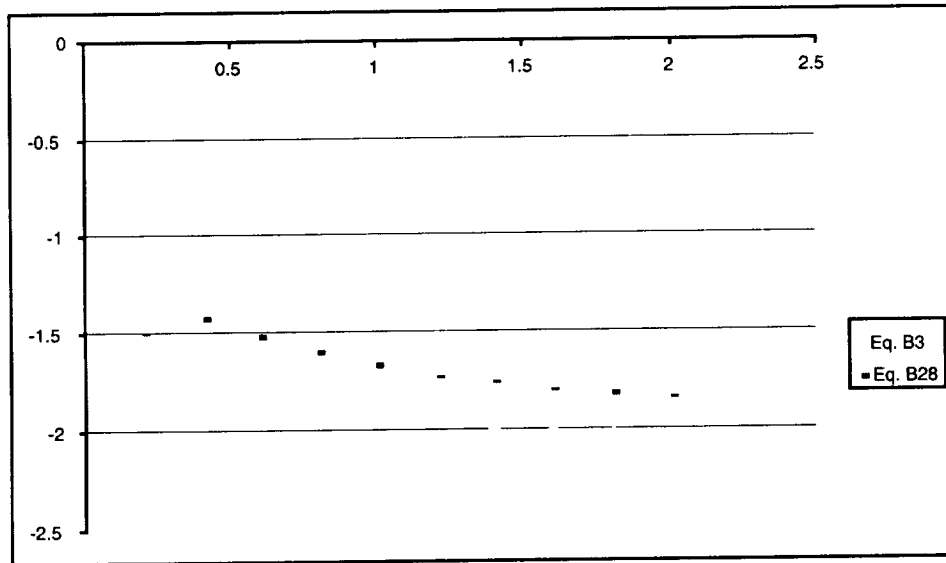


Fig. B7 -- Comparison of Numerical Assessment versus Approximate Analytical Expression for  $\gamma_{\text{sheet}}/\gamma$  versus  $h/R$  (Representative Case:  $c/R=0.4$  and  $b/R=2.5$ )

From Fig. B7 it can be seen that the hypothesis of  $\gamma_{\text{sheet}}/\gamma = -2$  (Eq. B4) is approximately valid.

This concludes the discussion validating the hypothesis of the circulation strength of the wing image vortex surfaces. This hypothesis,  $\gamma_{\text{sheet}}/\gamma = -2$ , has been validated by three different approaches: heuristic reasoning, a numerical assessment, and an approximate analytical treatment of the problem.

**REPORT DOCUMENTATION PAGE**Form Approved  
OMB No. 0704-0188

Public reporting burden for this collection of information is estimated to average 1 hour per response, including the time for reviewing instructions, searching existing data sources, gathering and maintaining the data needed, and completing and reviewing the collection of information. Send comments regarding this burden estimate or any other aspect of this collection of information, including suggestions for reducing this burden, to Washington Headquarters Services, Directorate for Information Operations and Reports, 1215 Jefferson Davis Highway, Suite 1204, Arlington, VA 22202-4302, and to the Office of Management and Budget, Paperwork Reduction Project (0704-0188), Washington, DC 20503.

<b>1. AGENCY USE ONLY (Leave blank)</b>		<b>2. REPORT DATE</b> April 2002	<b>3. REPORT TYPE AND DATES COVERED</b> Technical Memorandum	
<b>4. TITLE AND SUBTITLE</b> Rotor/Wing Interactions in Hover			<b>5. FUNDING NUMBERS</b>  712-92-43	
<b>6. AUTHOR(S)</b> Larry A. Young and Michael R. Derby				
<b>7. PERFORMING ORGANIZATION NAME(S) AND ADDRESS(ES)</b> Ames Research Center Moffett Field, CA 94035-1000			<b>8. PERFORMING ORGANIZATION REPORT NUMBER</b>  A-0207202	
<b>9. SPONSORING/MONITORING AGENCY NAME(S) AND ADDRESS(ES)</b> National Aeronautics and Space Administration Washington, DC 20546-0001			<b>10. SPONSORING/MONITORING AGENCY REPORT NUMBER</b>  NASA/TM-2002-211392	
<b>11. SUPPLEMENTARY NOTES</b> Point of Contact: Larry A. Young, Ames Research Center, MS T12B, Moffett Field, CA 94035-1000 (650) 604-4022				
<b>12a. DISTRIBUTION/AVAILABILITY STATEMENT</b> Unclassified — Unlimited Subject Category 02                      Distribution: Standard Availability: NASA CASI (301) 621-0390			<b>12b. DISTRIBUTION CODE</b>	
<b>13. ABSTRACT (Maximum 200 words)</b> <p>Hover predictions of tiltrotor aircraft are hampered by the lack of accurate and computationally efficient models for rotor/wing interactional aerodynamics. This paper summarizes the development of an approximate, potential flow solution for the rotor-on-rotor and wing-on-rotor interactions. This analysis is based on actuator disk and vortex theory and the method of images. The analysis is applicable for out-of-ground-effect predictions. The analysis is particularly suited for aircraft preliminary design studies. Flow field predictions from this simple analytical model are validated against experimental data from previous studies. The paper concludes with an analytical assessment of the influence of rotor-on-rotor and wing-on-rotor interactions. This assessment examines the effect of rotor-to-wing offset distance, wing sweep, wing span, and flaperon incidence angle on tiltrotor inflow and performance.</p>				
<b>14. SUBJECT TERMS</b> Tiltrotor aircraft, Interactional aerodynamics, Design and analysis			<b>15. NUMBER OF PAGES</b> 89	
			<b>16. PRICE CODE</b>	
<b>17. SECURITY CLASSIFICATION OF REPORT</b> Unclassified	<b>18. SECURITY CLASSIFICATION OF THIS PAGE</b> Unclassified	<b>19. SECURITY CLASSIFICATION OF ABSTRACT</b> Unclassified	<b>20. LIMITATION OF ABSTRACT</b>	

